Infrared Microspectroscopy of Focally Elevated Creatine in Brain Tissue from Amyloid Precursor Protein (APP) Transgenic Mice

Meghan Gallant

A Thesis submitted to the Faculty of Graduate Studies of the University of Manitoba in partial fulfilment of the requirements of the degree of

Master of Science

Department of Chemistry
University of Manitoba
Winnipeg, Manitoba

Abstract

Infrared microspectroscopy has been used to survey Alzheimer's diseased brain tissue from a transgenic mouse model of the disease. Alzheimer's disease is the leading cause of dementia among the elderly and is characterized by β-amyloid plaque deposition, neurofibrillary tangles, inflammation, and disturbed energy metabolism in the brain. Both the TgCRND8 and Tg19959 mouse models of the disease develop Alzheimer's disease pathology beginning at approximately 3 months of age. Infrared microspectroscopy allows analysis of untreated, flash frozen tissue samples, at micron level spatial resolution, and was used in this study to examine creatine deposits in the Alzheimer's diseased brain. Creatine is central to cellular energetics and plays an important role in proper brain function.

The hippocampi of 7 pairs of transgenic mice and their littermate controls were mapped using infrared microspectroscopy and the results were analyzed for creatine levels and levels of β-sheet, indicative of the presence of β-amyloid plaques. Creatine was found to be focally elevated in the transgenic mice, as compared to their littermate controls but was not co-localized with β-amyloid plaques. Further surveys of serial sections from one transgenic mouse showed the 3-dimensional distribution of creatine within the sample. Focally elevated creatine may be a marker of the disease process, indicative of disturbed energy metabolism or inflammatory response to the disease progression.

List of Published Papers

1. Gallant, M., Rak, M., Szeghalmi, A., Del Bigio, M. R., Westaway, D., Yang, J., Julian, R., & Gough, K. M. (2006) Focally elevated creatine detected in amyloid precursor protein (APP) transgenic mice and Alzheimer disease brain tissue. J Biol Chem, 281, 5-8.

List of Conference Presentations

1. Gallant, M., Rak, M., Kastyak, M., Del Bigio, M. R., Westaway, D., Gough, K. Imaging Focally Elevated Creatine in APP Transgenic Mice. Poster, Chemical Biophysics Symposium, University of Toronto, April 2007.

2. Gallant, M., Rak, M., Szeghalmi, A., Gough K., Del Bigio, M., Westaway, D., Julian, R. Imaging Molecular Changes in APP Transgenic Mice. Poster, CSC 2006, Canadian Chemistry Conference and Exhibition, May 2006

3. Gallant, M., Rak, M., Szeghalmi, A., Del Bigio, M., Westaway, D., Yang, J., Julian, R., Gough, K. Elevated Levels of Creatine Detected in APP Transgenic Mice and Alzheimer Disease Brain Tissue. Poster, Canadian Light Source Users Meeting, University of Saskatchewan, November 2005.

4. Rak, M., Gough, K., Gallant, M., Del Bigio, M., Mai S., Westaway, D. Synchrotron IR Spectromicroscopy of Plaques in a Transgenic Mouse Model of Alzheimer's Disease. Poster, Canadian Light Source Users Meeting, University of Saskatchewan, November 2004.

List of Abbreviations

AD ..... Alzheimer's disease
ADP ..... adenosine diphosphate
AGAT ..... L-arginine:glycine amidinotransferase
AGE ..... advanced glycation endproducts
ApoE ..... apolipoprotein E
APP ..... amyloid precursor protein
ATP ..... adenosine triphosphate
Aβ ..... amyloid β
CA ..... Cornu Ammonis
CK ..... creatine kinase
Cr ..... creatine
FPA ..... focal plane-array
FT ..... Fourier transform
GAA ..... guanidine acetic acid
GAMT ..... S-adenosyl-L-methionine:N-guanidinoacetate methyltransferase
IR ..... infrared
MAP ..... microtubule-associated proteins
MCT ..... mercury/cadmium telluride
MRS ..... magnetic resonance spectroscopy
NFT ..... neurofibrillary tangle
NO ..... nitric oxide
OCT ..... Optimal Cutting Temperature
P1 ..... presenilin 1
P2 ..... presenilin 2
PCr ..... phosphocreatine
PHF ..... paired helical filaments
ROS ..... reactive oxidizing species

Acknowledgements

I would like to thank several people whose assistance was invaluable to this thesis:

First, my supervisor, Dr Kathleen Gough for her support, guidance, and understanding throughout the research and writing of this thesis.

Members of the research group: Marzena Kastyak, Margaret Rak, Dr. Adrianna Szegalmi, Lsan Tsadzu, Tammy Welshman, Richard Wiens, Avid Khamenefer, Veena Agrawal, and Dr. Gajjeraman Sivakumar. I would especially like to thank Margaret Rak for her assistance with data collection and interpretation.

Dr. Bob Julian at the SRC for technical help and assistance with data collection.

Dr. David Westaway for donating transgenic mice and Dr. Marc Del Bigio for use of his research facilities.

Members of the defense committee: Dr. Melanie Martin and Dr. Jennifer van Wijngaarden.

Everyone in the Chemistry department.

The Manitoba Health Research Council for financial support

Finally, my family, and especially my parents, for their support and encouragement over these years.

Table of Contents

List of Tables

List of Figures

1. Introduction

1.1 Overview and Scope

Previous work in this research group had focused on analysis by infrared microspectroscopy of the brains of transgenic mice with Alzheimer's disease. In using this technique to analyze plaques characteristic of the disease, a spectral anomaly was noted in many infrared maps. This was determined later to be due to microcrystalline creatine deposits.

Although the deposits seemed to occur more frequently in the Alzheimer's diseased mice than in their littermate controls, this could not be confirmed without systematic analysis of both diseased and control brains. In this study, the hippocampus region of the brains of 7 pairs of transgenic mice from two different lines (TgCRND8 and Tg19959) was systematically surveyed for creatine content, by acquisition and analysis of large area infrared maps across each hippocampus. The goal was to determine whether creatine was focally elevated in the transgenic mice.

In order to understand better the nature of creatine in the diseased brain, further information about its distribution was needed. As distribution of creatine could be detected across tissue sections, analysis of serial sections could reveal the distribution of creatine in a third dimension. Infrared maps on serial sections from the brain of one transgenic mouse were acquired in an attempt to determine the three dimensional distribution of creatine through the brain.

We hypothesize that a better knowledge of the 3D distribution will provide clues regarding the origin of the creatine.

1.2 Alzheimer's Disease

Alzheimer's disease (AD) is characterized by progressive memory loss, deteriorating cognitive function, altered behavior and a progressive decline in language function. Although dementia – the deterioration of cognitive function to the point of interference with daily activities and quality of life (Villareal and Morris, 1998) – is a symptom of AD, other causes of dementia exist and their likelihood increases with age.

The distinguishing symptoms of AD were first described at meeting in Munich in 1906 by Alois Alzheimer, a German neurologist. In his report, he presented the case of a woman in her fifties who displayed the symptoms of the disease that would later bear his name (Selkoe, 2001). By the end of the 1960s, researchers had established that AD was the primary cause of dementia in the elderly (Roth et al, 1966; Blessed et al, 1968; Tomlinson et al, 1968; Tomlinson et al, 1970). Although much has been learned since that time, the need to further our understanding of the disease is evident. With rising life expectancy and thus an aging population, the societal and economic impact of the disease increases. In 1994, there were approximately 252,600 cases of dementia among Canadians over 65 (representing 8.0% of this age group), and 64% of these – or 161,000 cases – were attributed to AD (representing 5.1% of this age group) (Canadian Study of Health and Aging Working Group, 1994). A later study by the same research group estimated that there are a minimum of 60,150 new cases of dementia each year in Canada (Canadian Study of Health and Aging Working Group, 2000). Further, of 21 chronic conditions, AD has the most dramatic effect on a patient's health-related quality of life (Shultz and Kopec, 2003), and thus the impact of the disease extends far beyond the individual to their family and friends, community and society at large.

Alzheimer's disease is characterized by two lesions: extracellular plaques comprised of amyloid β-protein (Aβ) and neurofibrillary tangles (NFT) comprised of hyperphosphorylated tau proteins (Selkoe, 2001; Cummings and Cole, 2002). As these lesions can only be observed post-mortem, effective treatment of the symptoms of AD has necessitated the creation of means to assess whether a patient has AD, rather than other forms of dementia. Patients are assigned a probability of their having AD based on the presence and course of development of specific symptoms, while confirmation of definite AD is only assigned after the frequency of plaques and tangles has been assessed after autopsy or biopsy (McKhann et al, 1984; Khachaturian, 1985; Villareal and Morris, 1998; Newell et al, 1999; Hyman and Trojanowski, 1997; Mirra et al, 1991; National Institute on Aging and Reagan Institute Working Group on Diagnostic Criteria for the Neuropathological Assessment of Alzheimer's Disease, 1997).

1.2.1 Neurofibrillary Tangles

Tau proteins are members of the microtubule-associated proteins (MAP) family which are found primarily in neurons, and are thought to play regulatory role in neurite outgrowth and the maintenance of mature neuronal morphology (Tucker, 1990). While some phosphorylation of tau, at specific sites, is normal, tau proteins in the AD brain become hyperphosphorylated, either by increased kinase activity or decreased phosphatase activity, aggregating into insoluble polymers (Grundke-Iqbal et al, 1986; Illenberger et al, 1998; Lovestone and Reynolds, 1997). Tau proteins aggregate into paired helical filaments (PHF) – after which they are termed PHF-tau proteins – and combine with some straight filaments to form intraneuronal, non-membrane bound NFT,

which are characteristic of AD (Kidd, 1963; Terry, 1963; Terry et al, 1964; Kidd, 1964; Grundke-Iqbal et al, 1986; Kosik et al, 1986; Wood et al, 1986; Nukina and Ihara, 1986; Ihara et al, 1986; Selkoe, 2001; Buée et al, 2000).

In the early stages of AD, NFT are found throughout the hippocampal formation, followed by the anterior, inferior, and mid temporal cortex. The NFT then progress through the association areas of the temporal (superior), parietal and frontal cortex, and, finally, to the primary motor or sensory areas of the brain, including the primary motor cortex and primary visual cortex (Delacourte et al, 1999; Delacourte et al, 1998). While the presence of NFT is a criterion in the diagnosis of AD, some cases, though infrequent, see few NFT. This is most often the case in the Lewy Body Variant of AD (Terry et al, 1987; Hansen et al, 1993). NFT have been observed in several other diseases, including Pick's disease (Buée-Scherrer et al, 1996), postencephalitic parkinsonism (Geddes et al, 1993; Hof et al, 1992; Buée-Scherrer et al, 1997), amyotrophic lateral sclerosis/parkinsonism dementia complex of Guam (Buee-Scherrer et al, 1995; Hirano et al, 1966), and Down's syndrome (Hof et al, 1995), in some cases alongside plaques similar to those in AD and in other cases, without.

1.2.2 Plaques

The extracellular plaques characteristic of AD are comprised of Aβ peptides and are associated with dystrophic neurites, activated microglia and reactive astrocytes (Terry et al, 1964; Kidd, 1964; Dickson, 1997; Selkoe, 2001; Cummings and Cole, 2002). Aβ is derived from the amyloid precursor protein (APP), a transmembrane protein having 3 major isoforms (with 695, 751 or 770 residues). APP is cleaved by α-secretase and β-

secretase, and subsequently by γ-secretase to produce either p3 peptides, in the case of cleavage by α-secretase then γ-secretase, or Aβ peptides in the case of cleavage by β-secretase than γ-secretase (Esch et al, 1990; Koo and Squazzo, 1994; Sisodia, 1992; Vassar et al, 1999; Yan et al, 1999; Haas et al, 1993; Sinha et al, 1999; Selkoe, 2001) (Figure 1.1).

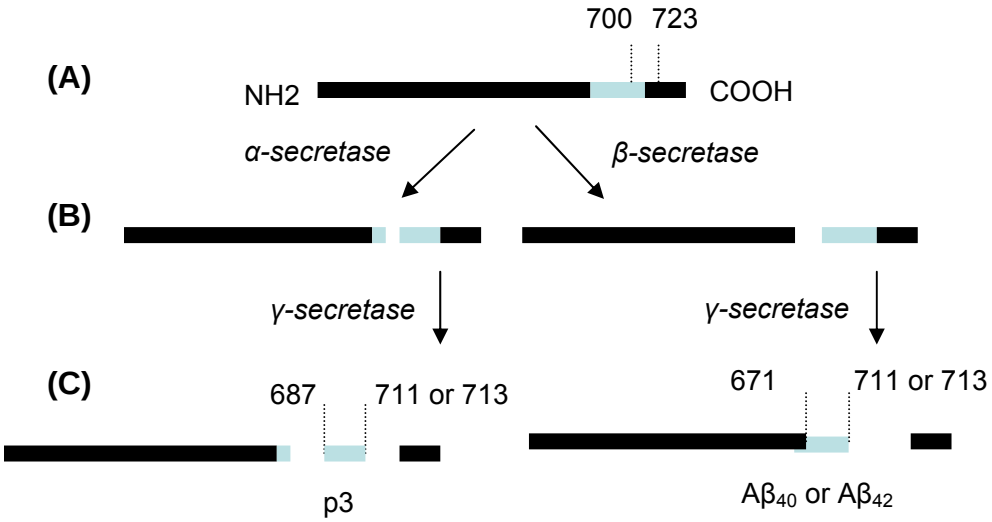

Figure 1.1: Cleavage of APP. APP (A) crosses the cellular membrane between residues 700 and 723. APP is cleaved by either α-secretase or β-secretase and the resulting proteins (B) are cleaved by γ-secretase. In the case of cleavage by α-secretase and then γ-secretase, p3 results, consisting of residues 687-711 or 687-713 of the original APP. In the case of cleavage by β-secretase and then γ-secretase, the result is Aβ40 (residues 671-711 of APP) or Aβ42 (residues 671-713 of APP) (C).

While neurons express the majority of APP, and secrete substantial amounts of Aβ peptides, APP can also be expressed by astrocytes (Busciglio et al, 1993), microglia (Haass et al, 1991), endothelial and smooth muscle cells (Haass et al, 1992) and other nonneuronal cells (Selkoe et al, 1988; Shoji et al, 1992). These cells may also release Aβ (Selkoe, 2001).

The gene that codes for APP production is located on chromosome 21, and as a result, individuals with Down's syndrome – having three copies of chromosome 21 rather than two – often develop amyloid plaques as early as their thirties or forties (Kang et al, 1987) The most common form of Aβ in the brain is the species ending at amino acid 40 ($A\beta_{40}$), although the species ending at amino acid 42 ($A\beta_{42}$) is also present. The longer, more hydrophobic $A\beta_{42}$ aggregates more readily into plaques, although co-aggregation of $A\beta_{40}$ is seen in developed plaques (Glenner and Wong, 1984; Masters et al, 1985; Iwatsubo et al, 1994; Harigaya et al, 1995). These plaques may reach more than 120 μm in cross-sectional diameter and are found throughout the limbic and association cortices in the diseased brain (Selkoe, 2001; Dickson, 1997).

The compact, fibrillar plaques – termed neuritic plaques – that were initially associated with the disease are different from diffuse plaques found in regions of the brain containing neuritic plaques, as well as those unaffected by the disease (Joachim et al, 1989). Diffuse plaques are amorphous, lacking the clear core and dystrophic neurites seen with neuritic plaques (Tagliavini et al, 1988; Yamaguchi et al, 1988). Diffuse plaques contain predominantly $A\beta_{42}$, with little to no $A\beta_{40}$ (Gowing et al, 1994; Iwatsubo et al, 1994; Selkoe, 2001).

1.2.3 Inflammation and Neurotoxicity in AD

1.2.3.1 Toxicity of Aβ and disturbed energy metabolism

In addition to plaque formation, $A\beta_{42}$ has been found to induce neuronal apoptosis (Kienlen-Campard et al, 2002), inhibit mitochondrial function as well as key enzymes (Casley et al, 2002), induce cellular degeneration (Bhatia et al, 2000), impair glucose

uptake and depress ATP levels (Mark et al, 1997), and is associated with abnormal synaptic morphology prior to the development of β-amyloid pathology (Takahashi et al, 2002). Aβ has been proven to induce nitric oxide (NO) synthesis, leading to oxidative damage of synaptic terminals, and to altered calcium homeostasis, possibly leading to neuronal death (Mattson et al, 1992). Despite this, some structural changes in synapses and electrophysiological alterations are detected before formation of diffuse plaques can be detected (Hsia et al, 1999).

Glucose metabolism and cellular energy production have been found to be severely reduced in the Alzheimer's diseased brain, limiting synthesis of several amino acids and ATP production as well as contributing to free radical formation and induced damage (Münch et al, 1998). Overall brain metabolism is increasingly reduced as severity of dementia increases (Gibson, 2002).

1.2.3.1 Inflammatory response in AD

Inflammatory response in the AD brain has been the subject of numerous studies and reviews (Neuroinflammation Working Group, 2000; Tuppo and Arias, 2005; Heneka, 2006; Versijpt et al, 2002; Butterfield et al, 2002). It is unsurprising that pathological hallmarks of AD – plaques and neurofibrillary tangles – would elicit an inflammatory response in the same way foreign material would elicit an inflammatory response in other regions of the body. The inflammatory pathways underway in the AD brain are complex and beyond the scope of this thesis, although a brief summary of the cellular mediators involved is useful.

The activated microglia found clustered around amyloid plaques are indicative of inflammation in the brain. Activation of microglia results in altered morphology of these

cells, and increased secretion of pro-inflammatory cytokines, chemokins, complement factors, reactive oxygen intermediates and nitric oxide, all of which contribute to neuronal dysfunction and cell death (Neuroinflammation Working Group, 2000; Tuppo and Arias, 2005; Heneka, 2006). Activated microglia are also linked to neuritic beading, which is linked to a rapid drop in intracellular ATP and neuronal death (Takeuchi et al, 2005).

Reactive astrocytes associated with amyloid plaques are also known to express numerous inflammatory mediators, including complement factors, cytokines, chemokines, proteases and protease inhibitors. Further, neurons have been shown to express complement proteins, and cytokines in the AD brain, which would exacerbate inflammatory damage (Neuroinflammation Working Group, 2000; Tuppo and Arias, 2005; Heneka, 2006). Altered calcium homeostasis, increased production of reactive oxidizing species (ROS), increased oxidative stress, reduced enzyme activity, and accumulations of advanced glycation endproducts (AGEs) are all common to the AD brain, and represent a complex process of imflammation, oxidative stress and ionic disruption that leads to neuritic dystrophy, synaptic and neuronal loss, and the clinical dementia characteristic of the disease (Gibson, 2002; Butterfield et al, 2002; Selkoe, 2001).

1.2.4 Genetic forms of AD

The most common form of AD is sporadic AD – the later onset version of the disease which is familiar to many – and is distinct from familial AD. Familial AD occurs earlier in life and is inherited through genetic mutations, many of which are understood well. Sporadic AD occurs later in life and, although genetics may predispose an individual to

the disease, these genetic factors are not well understood. While familial AD may, in specific lineages, include symptoms not typical of AD (such as seizures or myoclonus), the end results of sporadic and familial AD are virtually indistinguishable, both clinically and pathologically. This offers the potential to use these mutations to study the disease through transgenic models.

Three key genetic factors have been linked to AD: missense mutations in APP, missense mutations in presenilins and the inheritance of the apolipoprotein ε4 allele. However, other genetic indicators are currently being investigated and it is likely that the coming years will see a significant increase in our knowledge of genetic factors that predispose towards AD.

Missense mutations in APP are perhaps the least common of the known genetic causes of familial AD, but are well-characterized and are frequently employed in transgenic models of the disease. APP is encoded by a gene on chromosome 21 (Kang et al, 1987) and mutations on this gene result in amino acid substitutions in the immediate vicinity of locations of β-secretase cleavage, α-secretase cleavage, or γ-secretase cleavage. These substitutions alter typical cleavage and processing, leading to AD pathology (Johnson et al, 1994; Roher et al, 2004; Chartier-Harlin et al, 1991; Goate et al, 1991; Selkoe, 2001). Individuals experiencing AD as a product of these mutations often display AD symptoms at an early age, with onset ranging from the late thirties to late fifties (Selkoe, 2001; Roher et al, 2004).

The presenilin holoproteins are critical to γ-secretase cleavage of APP, producing $A\beta_{40}$ and $A\beta_{42}$. Two genes code for these proteins: presenilin1 (P1) is located on chromosome 14q and presenilin2 (P2) is located on chromosome 1 (Sherrington et al, 1995; Levy-

Lahad et al, 1995; Rogaev et al, 1995). Mutations on both P1 and P2 cause an increase in $A\beta_{42}$ by selectively increasing γ-secretase cleavage of APP, and onset of AD due to these mutations occurs as early as an individual's thirties (Selkoe, 2001; Scheuner et al, 1996). The apolipoprotein E (ApoE) has three alleles: ε2, ε3 and ε4. The risk of AD increases with the number of ε4 alleles, while the age of onset of AD decreases with the same (Corder et al, 1993; Strittmatter et al, 1993; Schmechel et al, 1993). The gene responsible for ApoE is located on chromosome 19q, and those individuals with the Apo ε4 allele display higher levels of diffuse Aβ42 in the brain than do those without the Apo ε4 allele, even in the absence of AD symptoms. This increase is due either to an enhanced deposition of Aβ, or decreased clearance of the same (Selkoe, 2001).

AD does not naturally occur in animals, although these known mutations have been used to create numerous transgenic mouse models of AD. By introducing genetic mutation into mice, litters can be raised where some mice display AD pathology and their littermates do not, affording an opportunity to study the disease progression and hallmarks with the assurance that 'control' mice have been raised in the same environment as their counterparts with AD (Wong et al, 2002; Price et al, 1998; Chishti et al, 2001; Li et al, 2004). This level of consistency is impossible with studies of human tissue.

1.3 Creatine and the Cr/PCr system

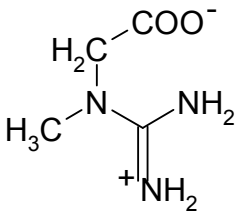

Figure 1.2: The creatine molecule

Creatine (Cr) is a small molecule (Figure 1.2) found in tissues with high energy demands - including the brain (Wyss and Kaddurah-Daouk, 2000) - which plays an important role in cellular energetics. Creatine kinase (CK) catalyzes the reversible transfer of a phosphate group from ATP to Cr, to form ADP and phosphorylcreatine (PCr) (Figure 1.3).

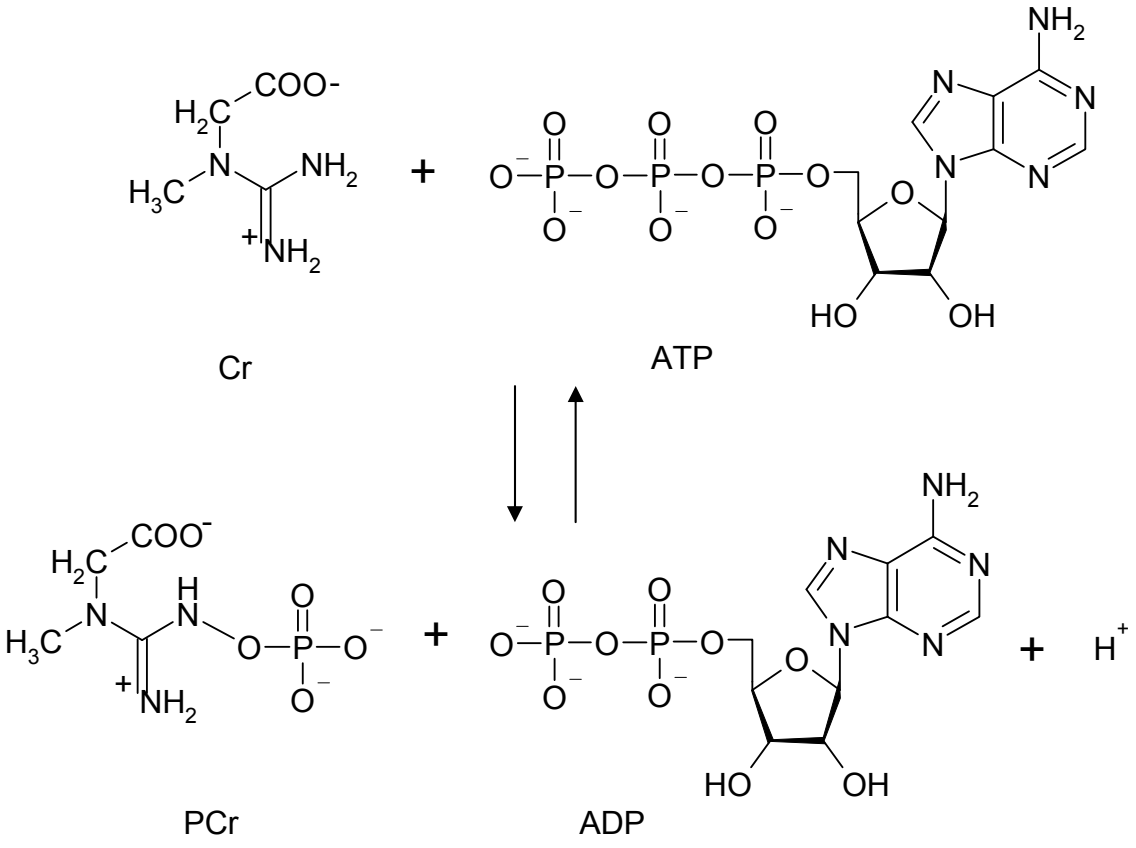

Figure 1.3: The CK reaction.

As PCr and Cr are smaller and less negatively charged than ADP and ATP, they are more easily transported between sites of ATP use and production. This renders the CK/PCr/Cr system central to energy metabolism in tissues with high, fluctuating energy demands that are ill-suited to rely on the diffusion of ATP and ADP between sites of ATP use and production.

Despite a lower concentration of Cr and CK in brain tissue as compared to skeletal muscle or heart tissue, the CK/PCr/Cr system is linked to proper brain function. CK has been noted to be involved in maintaining membrane potentials, calcium homeostasis, and the restoration of ion gradients before and after depolarization (Wallimann and Hemmer, 1994). Within the brain, concentrations of PCr and Cr are higher in gray matter as compared to white matter, mirroring the higher rates of ATP turnover in gray over white matter (Cadoux-Hudson et al, 1989).

Creatine is synthesized in the body in a two step process: an amidino group is transferred from arginine to glycine, catalyzed by L-arginine:glycine amidinotransferase (AGAT), to form L-ornithine and guanidinoacetic acid (GAA). GAA is then methylated, by *S*-adenosyl-L-methionine:*N*-guanidinoacetate methyltransferase (GAMT), to produce creatine (Figure 1.4).

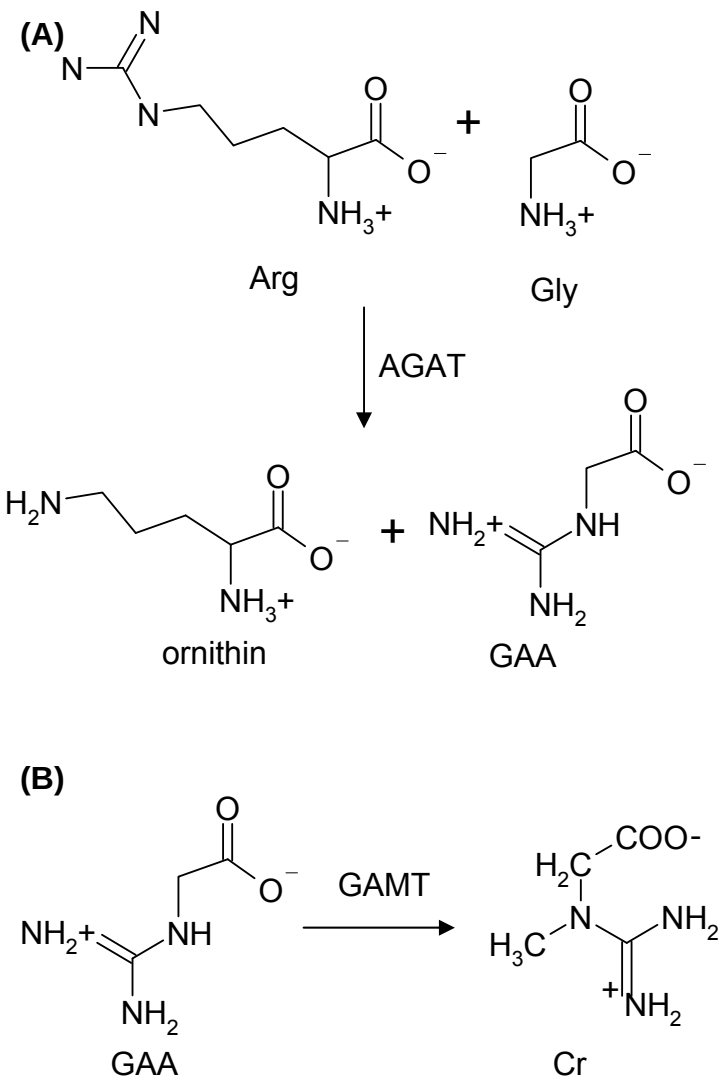

Figure 1.4: Synthesis of creatine. AGAT catalyses the transfer of an amidino group from Arg to Gly, to form ornithin and GAA (A). GAMT methylates GAA to produce Cr (B).

In most tissues, creatine uptake occurs through the blood, as regulated by the creatine transporter, after the first step of synthesis has occurred in the kidney, and the second in the liver, with the intermediate GAA being transported between both sites through the bloodstream (Wyss and Kaddurah-Daouk, 2000). However, transportation of creatine across the blood-brain barrier (BBB) is limited (Ohtsuki, 2004), and additional creatine is

synthesized within the brain, by neuronal and non-neuronal cells (Dringen et al, 1998; Braissant et al, 2001).

Creatine cyclizes reversibly and non-enzymatically to creatinine (Crn), which diffuses out of tissues and eventually is excreted.

M-CK and B-CK (referring to muscle and brain respectively) are subunits that form dimeric MM- MB- and BB-CK isoenzymes. MM-CK is present in muscle tissue, MB-CK is present in heart tissue, and BB-CK is present in brain tissue. BB-CK is known to be oxidatively modified in the AD brain, resulting in decreased activity (David et al, 1998; Castegna et al, 2002; Aksenov et al, 2000).

Due to potential neuroprotective properties, creatine supplementation has been explored for diseases such as Huntington's disease, Parkinson's disease and amyotrophic lateral sclerosis, although the impact of such supplementation may be limited by the ability of creatine to cross the blood-brain barrier (Wyss and Schulze, 2002; Tarnopolsky and Beal, 2001; Ipsiroglu et al, 2001).

1.4 Infrared Microspectroscopy

Infrared (IR) spectroscopy has been used for decades to characterize samples of various types. Light across the mid-infrared spectrum (2-25 μm) is used to excite vibrations in molecules. The spectrum of the infrared light absorbed in inducing these vibrations provides information about the sample in question. IR spectroscopy can be a powerful tool in identifying unknown samples, and in providing information to complement other analytical techniques. Improvements to instrumentation have enhanced the efficiency and reliability of IR spectroscopy, and have resulted in wide-raging applications for the technique.

A full understanding of IR spectroscopy requires some explanation of molecular vibrations and how they are excited, as well as a description of current options and design of instruments in use.

1.4.1 Principles of Infrared Spectroscopy

In classical mechanics, molecular bonds are viewed as springs that connect two balls – the atoms involved. The laws of classical mechanics can be applied to such a model, and as such the back and forth vibration – termed harmonic oscillation – of two atoms connected by such a spring/bond can be described by Hooke's law:

$$F = -kx$$

Here, F is the restoring force of the spring/bond, k is the force constant of the spring, and x describes the displacement of one atom, viewing the other as stationary.

The potential energy of this system will vary as the atom moves back and forth about its equilibrium position, with potential energy at a minimum when the moving atom is at the

equilibrium position and at a maximum when the moving atom is at its maximum displacement. The potential energy, V, can be described mathematically as:

$$V = \tfrac{1}{2} kx^2$$

The change in V as a function of x can be plotted to show the parabolic potential energy profile of the system (Figure 1.5).

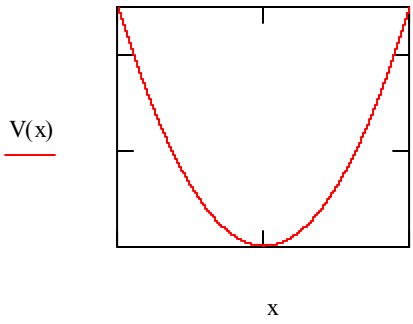

Figure 1.5: The potential energy of the harmonic oscillator

However, the description of a molecular bond as a spring joining two balls/atoms is a gross approximation. Quantum mechanics must be used to obtain a more accurate description of this system.

In quantum mechanics, all information about a given system is described by its wave function (or state function), Ψ, and observable properties of a system are derived using various operators, rather than the functions used in classical mechanics. The Hamiltonian operator yields the total energy (kinetic and potential) of a system and is used in the Schrödinger equation:

$$H\Psi = E\Psi$$

The Schrödinger equation is an eigenvalue equation: Ψ is an eigenfunction of the operator H, as performing H on Ψ results in a constant, or eigenvalue, E, multiplied by

the wave function Ψ. Each value of E that satisfies the equation for a system represents a possible energy state.

For a one-dimensional, single particle system, the Hamiltonian operator is

$$\mathrm{H} = \frac{-\hbar^2}{2m}\frac{d^2}{dx^2} + V(x)$$

The first term describes the kinetic energy of a particle with mass m moving along x. For a diatomic molecule, however, the mass m can be replaced by a term μ, the effective mass, that incorporates the masses of both atoms involved, labeled A and B:

$$\mu = \frac{m_A m_B}{m_A + m_B}$$

The potential energy, V(x), for a harmonic oscillator can then be substituted into the operator, and the Schrödinger equation solved to give:

$$\mathrm{E}_v = (\mathrm{v} + \tfrac{1}{2})h\nu$$

$$\text{Where } \nu = \frac{1}{2\pi}\left(\frac{k}{\mu}\right)^{1/2}$$

What is important to note in this equation is that only certain energy levels are allowed: v, referred to as the vibrational quantum number, must take on real integer values (v = 0, 1, 2, …). This can be understood by superimposing a series of discrete, allowed energy levels on the previously-obtained parabola that described the potential energy of a harmonic oscillator (Figure 1.6).

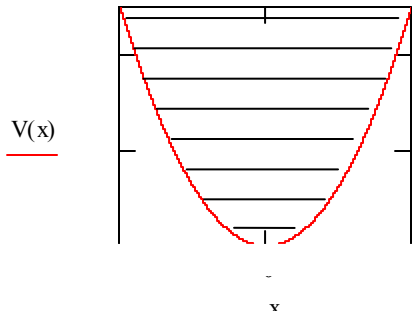

Figure 1.6: The potential energy of the quantum mechanical harmonic oscillator

The difference in energy between two consecutive states, n and n-1, is:

$$\Delta E = E_n - E_{n-1} = (n + \tfrac{1}{2})h\nu - (n - 1 + \tfrac{1}{2})h\nu = h\nu$$

As the change in energy between states is $h\nu$, ν corresponds to the frequency of light that would need to be absorbed by the system in order to induce the change in vibrational state. Using atomic masses and force constants for atomic bonds, it can be shown that light in the infrared range is of the correct energy to induce such vibrational state changes for most molecules.

The description of diatomic molecules as harmonic oscillators is another approximation. While the model is a reasonable approximation when molecules are in lower energy states, at higher energies the molecular vibrations become increasingly anharmonic. The Morse oscillator offers a more accurate, but still approximate, model for vibrations of higher energy. Using this model, the potential energy term used in the Hamiltonian operator must be replaced by:

$$V(x) = hcD_e(1 - e^{-ax})^2 \qquad a = \left(\frac{k}{2hcD_e}\right)^{\frac{1}{2}}$$

Where D_e is the dissociation energy in units of cm^{-1}. Solving the Schrödinger equation using this term for potential energy produces the result:

$$E_v = (v+\tfrac{1}{2})h\nu - (v+\tfrac{1}{2})^2 h\nu X_e$$

The term X_e is an anharmonicity constant. The potential energy curve described under this system deviates significantly from that of the harmonic oscillator at higher energy levels, with the separation between consecutive energy levels decreasing (Figure 1.7). Eventually the increasing energy becomes sufficient to cause dissociation of the bond (Herzberg, 1939).

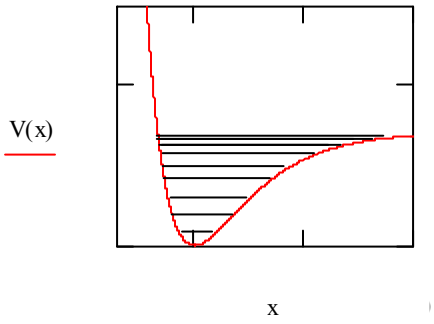

Figure 1.7: The potential energy of the anharmonic oscillator

For polyatomic molecules, many different vibrations are possible: each atom in the molecule can move in three directions, or has three degrees of freedom. For a molecule with N atoms, there are 3N ways the molecule can move. However, if all atoms move at once in the x, y, or z direction, translation, rather than vibration, occurs. Similarly, there are three possible rotations of nonlinear molecules: over an x, y, or z axis. Thus there are 3N-6 so-called normal modes of vibration, each independent of one another and having its own potential energy curve with a characteristic frequency of light needed to excite vibrations.

Not all transitions can be excited through absorption of infrared radiation. For a vibration to be infrared active, there must be a change in the molecular dipole as the molecule

vibrates. For those modes that are infrared active, the transition from the ground, or lowest energy, state to the first excited state is the most likely. Transitions to higher excited states, called overtones, may occur but are less likely. It is also possible for more than one vibrational mode to be excited simultaneously, as a combination (Herzberg, 1945).

An infrared spectrum is acquired by exposing a molecule to a full spectrum of infrared radiation (usually 4000-600 cm^{-1}, where cm^{-1} represents the inverse of the wavelength) and then detecting those frequencies that are absorbed to induce molecular vibrations. The resultant spectrum will be characteristic of the molecule that produces it, and can be used to identify the molecule. While specific functional groups will produce similar absorption profiles in each molecule in which they appear, the overall infrared spectrum of a molecule is unique, and can be used to identify specific molecules.

1.4.2 Infrared Spectroscopy Instrumentation

The first instruments used for infrared spectroscopy were dispersive spectrophotometers. With these instruments, infrared radiation from one source was split into two beams, one of which would act as a reference, and the other would pass through the sample to be analyzed. The reference would act to ensure that infrared absorption from atmosphere would not be seen in the sample spectrum. A dispersive grating would then be used to scan across the infrared spectrum, and the absorbance or transmission of infrared radiation by the sample at each wavelength would be detected and converted into a readable spectrum.

There are numerous restrictions that are inherent to this system, including the time taken to obtain a single spectrum. Fourier transform instruments have since been introduced that allow for spectra to be obtained more rapidly and with greater reproducibility (Griffiths et al, 1977).

A Fourier transform spectrometer uses an interferometer to collect data from a full infrared region simultaneously (Figure 1.8). Light from an infrared source is split by a beam splitter, directing half of the incident radiation to a fixed mirror and the other half to a moving mirror. Both mirrors redirect the light to the same beam splitter, which sends half the radiation from each mirror through the sample to a detector, while the other half is lost.

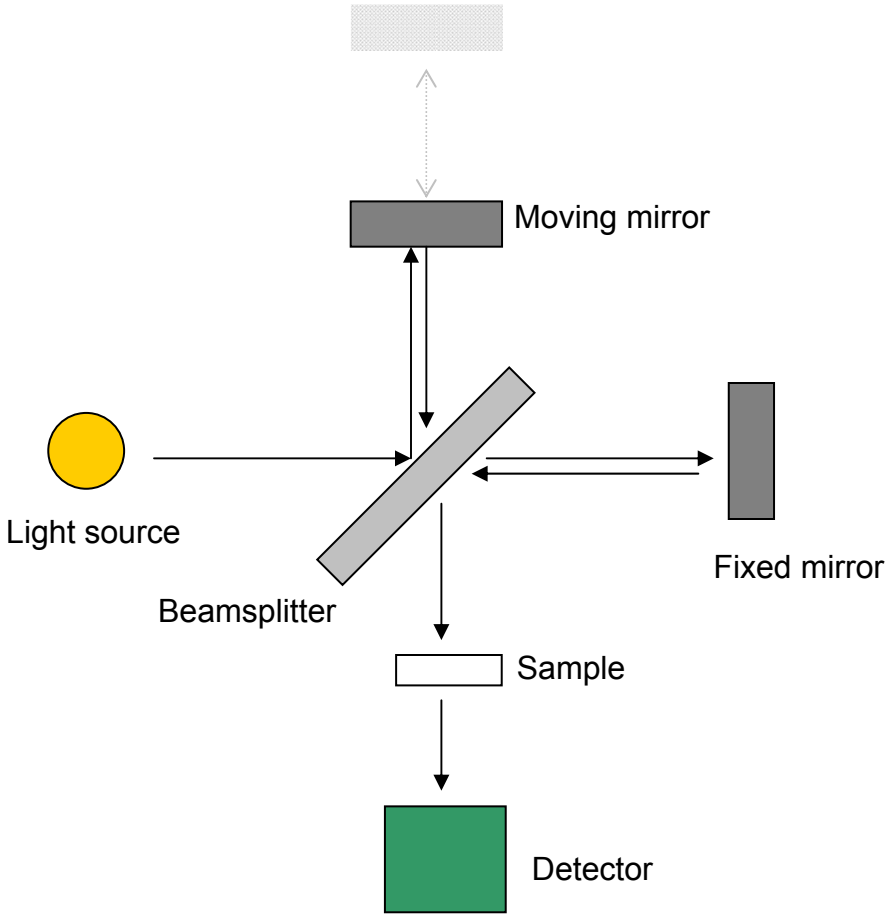

Figure 1.8: The Michaelson interferometer.

Information is derived from the intensity of the light detected as a function of the position of the moving mirror. If light of one wavelength is transmitted through the interferometer, the intensity at the detector will be highest when the moving mirror is at the same distance from the beam splitter as is the fixed mirror, due to constructive interference of the waves. If the mirror is moved 1/4λ away, the light traveling via the moving mirror will have traveled a distance of 1/2λ more than that traveling via the fixed mirror, resulting in destructive interference and a lack of signal at the detector. When multiple wavelengths are transmitted through an interferometer, the result is an interferogram that represents the sum of the contributions of each wavelength (Figure 1.9A). This interferogram is converted by a Fourier transform (FT) operation to a spectrum showing the absorbance or transmittance of each wavelength of radiation as it passed through the sample (Figure 1.9B).

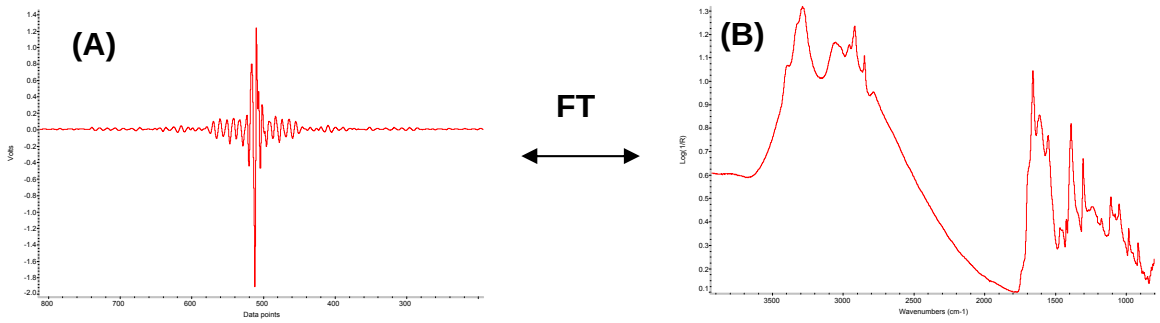

Figure 1.9: The Fourier Transform. An interferogram (A) and an infrared spectrum (B) can be interconverted by the Fourier transform.

Mathematically, the Fourier transform is a pair of equations that describe the relationship between interferogram and spectrum:

$$I(\delta) = \int_0^\infty B(\upsilon)\cos(2\pi\delta\upsilon)d\upsilon$$

$$B(\upsilon) = \int_{-\infty}^{\infty} I(\delta)\cos(2\pi\upsilon\delta)d\delta$$

The first of these equations is a description of the interferogram: the intensity of light detected, I, as a function of the displacement, δ, of the moving mirror in the interferometer. The second equation describes the spectrum: the intensity of light, B, as a function of the frequency, ν, of that light. The Fourier transform equations not only describe the reality of the interrelation of spectrum and interferogram, but allow the two descriptions of the same properties to be interconverted.

It is worth noting that the second equation, which would convert an interferogram to a spectrum, requires taking the integral from negative infinity to positive infinity of the displacement of a mirror. Clearly, this poses a practical dilemma. Truncating this displacement introduces artifacts into the resultant spectrum, and numerous apodization functions can be applied to minimize these effects. In addition, the resolution of spectral features is limited by the distance this mirror can move.

Detectors for infrared spectrometers are generally mercury/cadmium telluride (MCT) photoconducting transducers. When radiation strikes these detectors, electrons in the semi-conducting surface are excited to a higher conducting state, and the magnitude of this change is a function of the power of the incident radiation. In order to reduce the random thermal excitation of these electrons, which is a major source of noise, the detector must be cooled to 77 K with liquid nitrogen.

1.4.3 Infrared Microspectroscopy

Infrared microspectroscopy has been performed since the 1950s by coupling an infrared spectrometer to a microscope, allowing a small region of a sample to be selected for

analysis (Fraser, 1950). While the principles of infrared microspectroscopy are the same as those of conventional infrared spectroscopy, there are some particulars to the instrumentation that are worth noting.

Infrared microscopes differ from conventional light microscopes by their lack of lenses, which would absorb infrared radiation. Infrared radiation, having passed through an interferometer, is focused through a Schwarzschild objective onto the sample and either transmitted or reflected, depending on the sample and the substrate on which it is mounted (Figure 1.10). With transmission measurements, the radiation is refocused through a second Schwarzschild objective before reaching the detector, while in reflectance, the radiation is reflected through the same objective before reaching the detector.

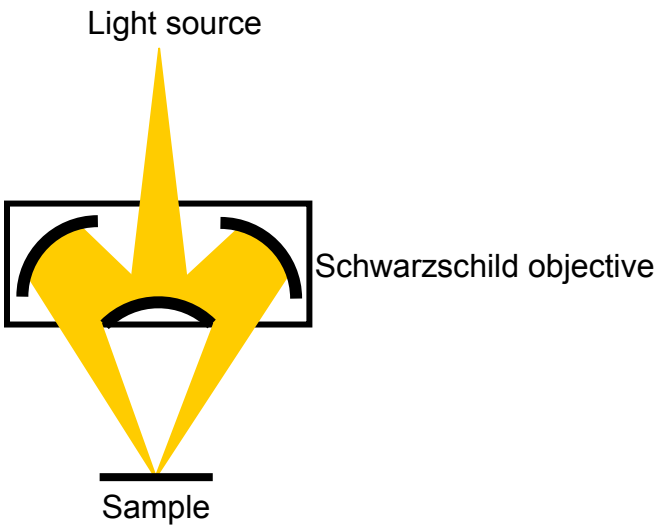

Figure 1.10: The Schwarzschild objective.

Two types of detectors are used for infrared microspectroscopy. With single-point detectors, an aperture is used to limit the spot size of the light before it reaches the sample, defining the size of the area, or the pixel, where a spectrum will be acquired, and

a second aperture can be used to constrain the light before reaching the detector. A series of spectra can be acquired in this way, by raster scanning the sample, to allow for spectral analysis over broad areas of a sample.

With the second type of detector, no apertures are used and a broader beam of light is used to illuminate the sample. Rather than a point detector, however, a series of detectors are arranged as a focal-plane array (FPA) and spectra from adjacent pixels can be collected simultaneously (Lewis et al, 1995; Huffman et al, 2002).

1.4.4 Infrared Light Sources

The excitation of atoms and electrons in a heated object leads to emission of electromagnetic radiation as atoms and electrons return to their low energy ground state. Radiation produced in this way is of broad spectrum, and the total emission increases, while the wavelength of maximum emission decreases, with increasing temperature.

By heating an object, such as a ceramic bar, infrared radiation can be produced. Referred as a globar, this has been the most common means of producing infrared radiation for spectroscopic analysis for decades.

Synchrotron light sources house relativistic electrons in storage rings using bending magnets to control the electrons' trajectory and to induce emission of synchrotron radiation. These electrons radiate broadband radiation – including infrared – that is of high flux and is highly collimated (Duncan and Williams, 1983). While the broadband x-ray radiation available from synchrotron light sources has been the most common use of these facilities, infrared synchrotron radiation is being used to an increasing degree, with infrared ports now in place at many, if not most, synchrotron facilities (Carr et al, 1995;

Nucara et al, 2003; Dumas et al, 2006; Miller and Dumas, 2006). The infrared radiation produced from synchrotron light sources in considerably brighter – approximately 1,000 times brighter in the infrared region – than that available from globar sources (Duncan and Williams, 1983).

With single-point measurements, the aperture size can be reduced considerably more using synchrotron radiation as compared to radiation produced by a globar source. With a globar, the signal/noise ratio is reduced beyond a workable level at aperture sizes of less than 20 μm. Using a synchrotron source, the aperture can be reduced until resolution becomes diffraction-limited: when the size of the opening through the aperture reaches the wavelength of the light passing through, diffraction of light becomes problematic, reducing the spatial resolution obtained, despite a narrower aperture. For microscopes using a single aperture, the spatial resolution at the diffraction limit is approximately $2\lambda/3$, while the limit for confocal microscopes, using a second aperture, is approximately $\lambda/2$ (Carr, 2001).

While synchrotron sources are preferable for single-point measurements, both globar and synchrotron sources can be used with success for measurement using FPA detectors. As the purpose is to illuminate a large area, the brightness advantage of synchrotron radiation is reduced. While an FPA allows rapid data collection, the spatial resolution is limited due to individual detectors being smaller than some infrared wavelengths, introducing diffraction artifacts (Miller and Smith, 2005).

1.4.5 Infrared Analysis of Biological Samples

Like all molecules, biological samples can be analyzed using infrared spectroscopy. Tissue components, including proteins, lipids, and nucleic acids, display unique spectra and contribute to the infrared absorbance profile of tissue samples (Mantsch and Chapman, 1996). The relative levels of various components can be determined by their absorbance levels within an infrared spectrum.

The amide bonds of proteins display three characteristic absorbance bands: the amide I profile ranges from 1600-1700 cm^{-1}, the amide II profile ranges from 1500-1600 cm^{-1} and the amide III profile from 1200-1350 cm^{-1}. These absorbance profiles, in particular the amide I region, are sensitive to the secondary structure of the protein and so can be used to evaluate relative levels of α-helix, β-sheet, or random coil folding within protein aggregates. Within the amide I region, proteins with α-helix conformations show a maximum absorbance between 1650-1660 cm^{-1}, and proteins with β-sheet conformations show maximum absorbance between 1615-1643 cm^{-1} (Surewicz et al, 1993) (Figure 1.11).

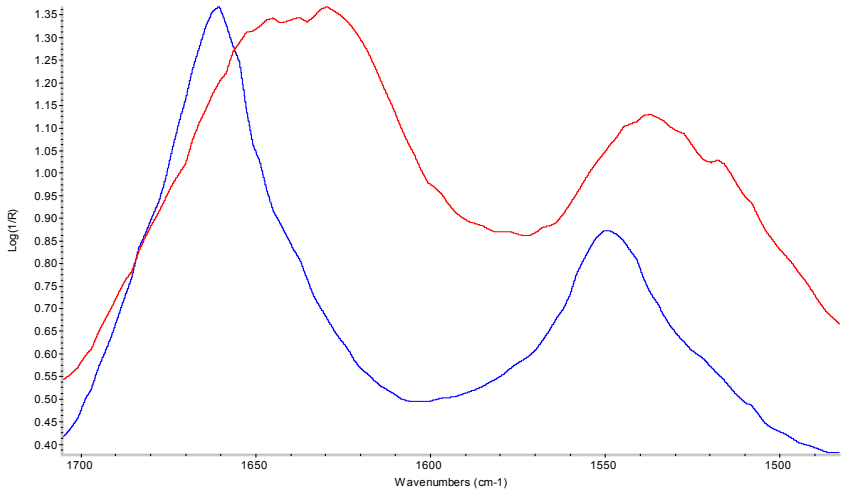

Figure 1.11: Amide I and II profiles. The absorbance profiles in the amide I and II regions of tissue with high (red) and low (blue) β-sheet.

Sample preparation for infrared spectroscopy involves sectioning a sample into slices approximately 8 μm thick and does not require any solvent treatments or chemical modifications of the sample. As nothing is added to, or removed from, the sample, infrared analysis allows the sample to be analyzed in its original state, *in situ*.

Infrared microspectroscopy has been used to analyze biological tissues to study numerous conditions, ranging from plaque deposition in Alzheimer's Disease (Choo et al, 1996), scarring in the cardiomyopathic heart (Gough et al, 2003), collagen and proteoglycan in cartilage (Camacho et al, 2000), colorectal adenocarcinoma (Lasch et al, 2004), and live cell imaging (Jamin et al, 2006). Applications of this rapidly-developing technique have been reviewed extensively (Dumas and Miller, J Biol Physics, 2003; Dumas and Miller, Vib Spec, 2003; Miller and Dumas, 2006; Dumas et al, 2006).

2. Materials and Methods

2.1 Transgenic mice

The TgCRND8 mice were developed at the Centre for Research in Neurodegenerative Disease (CRND) at the University of Toronto and were donated by Dr David Westaway. These mice express a double mutant form of human APP 695 (KM670/671NL + V717F). The first mutation, termed the Swedish mutation, is a double mutation in the APP gene that results in the substitution of Lys to Asn at codon 670 and Met to Leu at codon 671. The second mutation, the Indiana mutation, is a substitution from Val to Phe at position 717 of APP. As a result, TgCRND8 mice display Aβ deposits at 3 months of age, and dense-cored plaques and neuritic pathology at 5 months of age (Chishti et al, 2001).

The Tg19959 mice contain the same mutations to APP695 but are maintained on a different genetic background than the TgCRND8 mice. Tg19959 display similar levels of APP holoprotein expression and associated pathology, with plaque formation beginning at approximately 3 months of age (Li et al, 2004).

Twenty-five mice were provided by Westaway, ranging in age from 241 to 624 days and including 5 pairs of TgCRND8 and control littermates of the same sex, 2 pairs of Tg19959 and control littermates of the same sex, and 3 pairs of TgCRND8 and control littermates of opposite sexes (Table 2.1).

Table 2.1: Age and sex of transgenic and littermate mice.

Mouse	Sex	Age	Genotype
A01	Female	624	Tg(KM670/671NL+V717F)8 +/- (C3H/C57)
A02	Female	624	Tg(KM670/671NL+V717F)8 -/- (C3H/C57)
A03	Female	504	Tg(KM670/671NL+V717F)8 +/- (C3H/C57)
A04	Male	504	Tg(KM670/671NL+V717F)8 -/- (C3H/C57)
A05	Male	478	Tg(KM670/671NL+V717F)8 +/- (C3H/C57)
A06	Male	478	Tg(KM670/671NL+V717F)8 -/- (C3H/C57)
A07	Female	457	Tg(KM670/671NL+V717F)8 -/- (C3H/C57)
A08	Female	457	Tg(KM670/671NL+V717F)8 -/- (C3H/C57)
A09	Female	457	Tg(KM670/671NL+V717F)8 -/- (C3H/C57)
A10	Female	457	Tg(KM670/671NL+V717F)8 -/- (C3H/C57)
A11	Female	457	Tg(KM670/671NL+V717F)8 +/- (C3H/C57)
A12	Male	435	Tg(KM670/671NL+V717F)8 +/- (C3H/C57)
A13	Female	429	Tg(KM670/671NL+V717F)8 -/- (C3H/C57)
A14	Female	429	Tg(KM670/671NL+V717F)8 +/- (C3H/C57)
A15	Male	429	Tg(KM670/671NL+V717F)8 -/- (C3H/C57)
A16	Male	429	Tg(KM670/671NL+V717F)8 +/- (C3H/C57)
A17	Female	419	Tg(KM670/671NL+V717F)8 +/- (C3H/C57)
A18	Female	419	Tg(KM670/671NL+V717F)8 +/- (C3H/C57)
A19	Male	419	Tg(KM670/671NL+V717F)8 -/- (C3H/C57)
A20	Male	419	Tg(KM670/671NL+V717F)8 -/- (C3H/C57)
A21	Female	266	Tg(KM670/671NL+V717F)19959 -/-
A22	Female	266	Tg(KM670/671NL+V717F)19959 +/-
A23	Female	266	Tg(KM670/671NL+V717F)19959 -/-
A24	Male	241	Tg(KM670/671NL+V717F)19959 -/-
A25	Male	241	Tg(KM670/671NL+V717F)19959 +/-

2.2 Tissue Preparation

All 25 mice were sacrificed in Dr Marc Del Bigio's laboratory at the John Buhler Research Centre by members of the Gough research group. Mice were sacrificed by cervical dislocation, after which the brains were removed and bisected at the midline. The right hemisphere of each brain was placed in cold 3% paraformaldehyde in 0.1M phosphate-buffered saline for fixation. These were dehydrated and embedded in paraffin to be used for histochemical analysis. The left hemisphere of each brain was embedded in OCT (Optimal Cutting Temperature, Sakura, Tokyo, Japan) and snap-frozen by immersion in liquid nitrogen for 30 seconds. OCT-embedded brains were stored at -80^{o}C until sectioning. Animals were treated in accordance with the guidelines of the Canadian Council of Animal Care. Protocols were approved by the University of Toronto and the University of Manitoba.

2.3 Sectioning

Samples A01-A06, A10, A11, A13-A16, A18, and A21-A25 were warmed to -20^{o}C and cryosectioned at 8 μm thickness by Meghan Gallant and Margaret Rak, graduate students in the Gough research group. Serial sections were mounted on glass slides for Congo Red staining and on IR reflective slides (Low-e MirrIRTM, Kevley Techologies, Chesterland, OH) and gold-coated silicon chips (Sychrotron Radiation Centre) for infrared analysis.

Twenty serial sections of sample A14 were cryosectioned at 8 μm thickness and mounted on gold-coated slides for infrared analysis.

2.4 Staining

For each of samples A01-A06, A18 and A21-A25, the section serial to the section mounted on gold for IR analysis was stained with Congo Red and Hematoxylin using kits purchased through Sigma Diagnostics and protocols based on those developed by Puchtler, and modified by Margaret Rak (Puchtler et al, 1961; Rak, 2007).

2.5 Infrared data acquisition

Infrared spectra were acquired using a Bruker Tensor 27 FTIR with Bruker Hyperion microscope available at the University of Manitoba or a Nicolet Magna 500 FTIR with Nic-Plan or Nicolet Continuum IR microscope at the Synchrotron Radiation Centre, University of Wisconsin. All spectra were acquired at 4 cm^{-1} resolution, in reflectance mode, using a Happ-Genzel apodization function and saved in log(1/R) format.
Point spectra were acquired stepwise over specified areas to create infrared maps that would be processed for various tissue components. Sequential maps were acquired across the hippocampi of transgenic and littermate mice, and of serial sections of one mouse, such that processed maps could be tiled together to give a false-colour image of the distribution of various tissue components across the hippocampus of each sample.

2.5.1 Maps using globar light source

The aperture limiting the spot size of IR light through the Bruker Hyperion microscope was limited to 25 μm by 25 μm, and spectra were acquired with a step size of 20 μm. At each point, 128 spectra were summed in order to ensure adequate signal-to-noise ratios and high-quality spectra for analysis.

The Hyperion microscope was not equipped with an enclosed compartment to protect the sample, and IR absorbance bands from atmospheric components were removed by collecting a background spectrum, taking the ratio of the sample spectrum over the background spectrum, and using the resultant value as the Reflectance in the final log(1/R) format.

2.5.2 Maps using synchrotron light source

The aperture on both the Nicolet Nic-plan and Continuum microscope was set to 12 μm on either side, and spectra were acquired with a step size of 10 μm. Between 16 and 128 spectra were summed at each point, depending on the quality of the signal and anticipated size of the map.

The Nic-plan microscope featured an enclosed chamber in which the sample was held. Dry nitrogen flowed through this chamber continuously in order to minimize absorbance from atmospheric carbon dioxide and water vapour. At the time maps were collected using the Continuum microscope, the enclosed chamber and purge system had not yet been installed. Absorbance bands from the diamond window separating the ultra-high vacuum synchrotron storage ring and the microscope were removed by collecting a background spectrum, taking the ratio of the sample spectrum over the background spectrum, and using the resultant value as the Reflectance in the final log(1/R) format.

2.6 Infrared analysis

Characteristic IR absorbance bands were used to analyze raw, unprocessed IR spectra for levels of creatine, plaque and other tissue components. Data acquired using the Nicolet FTIR and microscopes were analyzed using the proprietary Omnic and Atlμs software,

while data acquired using the Bruker FTIR and microscope were analyzed using Cytospec software (Cytospec, Inc.).

With both software packages, creatine identification was based on the peak at 1304 cm^{-1} and plaque based on the ratio of peaks between 1660-1650 cm^{-1} and 1640-1620 cm^{-1}. In both cases, peak area rather than peak height was used for analysis.

All pixels identified as containing creatine were checked to ensure that no false positives were reported.

2.6.1 Processing using Omnic and Atlμs

For analysis of creatine with Omnic/Atlμs, the absorbance levels at 1321 cm^{-1} and 1295 cm^{-1} were set as baseline values and the area between this baseline and the peak between 1313-1303 cm^{-1} was measured (Figure 2.1).

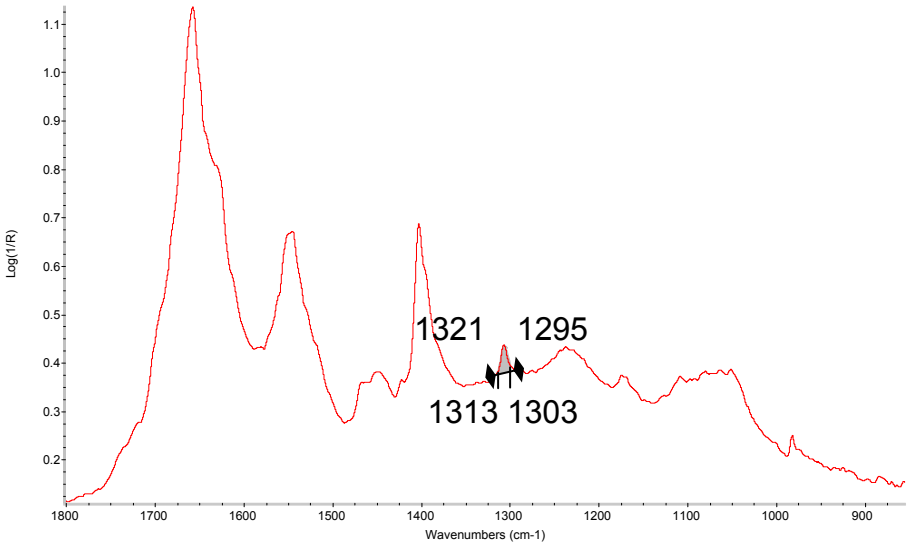

Figure 2.1: Creatine processing parameters using Atlμs.

Display limits (area under the set curve) were set at 0.18-0.35, and colours ranging from red (low) to blue (high) were assigned progressively to pixels falling within this range.

For samples A11 and A22, these parameters did not accurately assess creatine levels. For these samples, an alternate set of parameters was used, with a baseline set at absorbance

values at 1322 cm^{-1} and 1289 cm^{-1}. The area under the peak between 1311 cm^{-1} and 1300 cm^{-1} was determined, with display limits set at 0.375-0.6 (Figure 2.2).

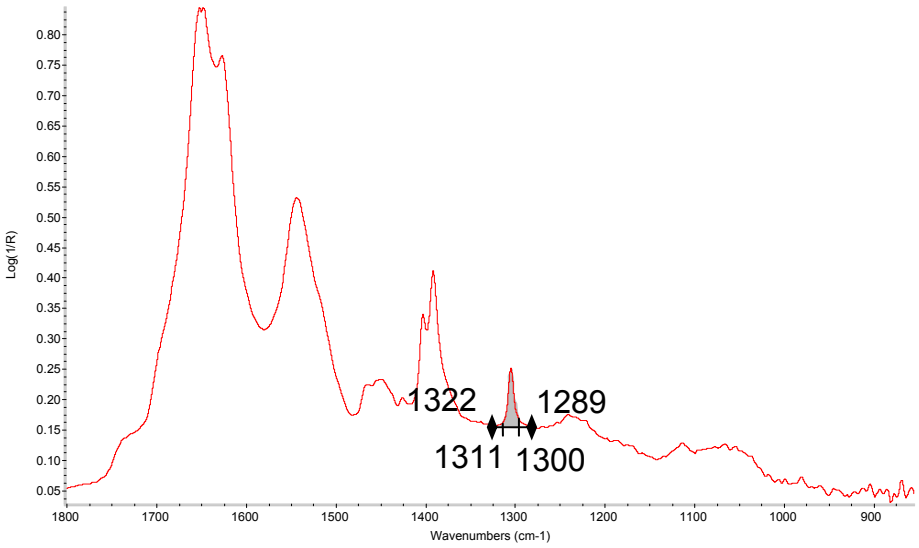

Figure 2.2: Alternate creatine processing parameters using Atlμs.

For analysis of plaque with Omnic/Atlμs, a ratio was taken between the peak area between 1662-1652 cm^{-1} and the peak area between 1630-1620 cm^{-1}. For both, the absorbance levels at 1806 cm^{-1} and 900 cm^{-1} were set as baseline. Display limits were set at 0.8-2.2 (Figure 2.3).

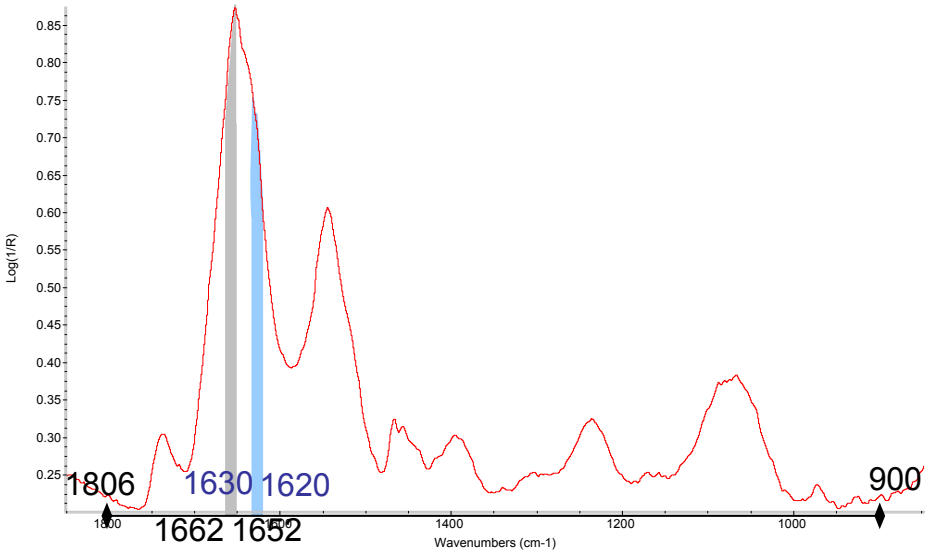

Figure 2.3: Plaque processing parameters using Atlμs.

2.6.2 Processing using Cytospec

For uni-variate analysis of creatine using Cytospec, the area under the peak between 1295-1315 cm^{-1} was used, with the absorbance at these points establishing the baseline (Figure 2.3). Display limits were set at 0.17-0.11.

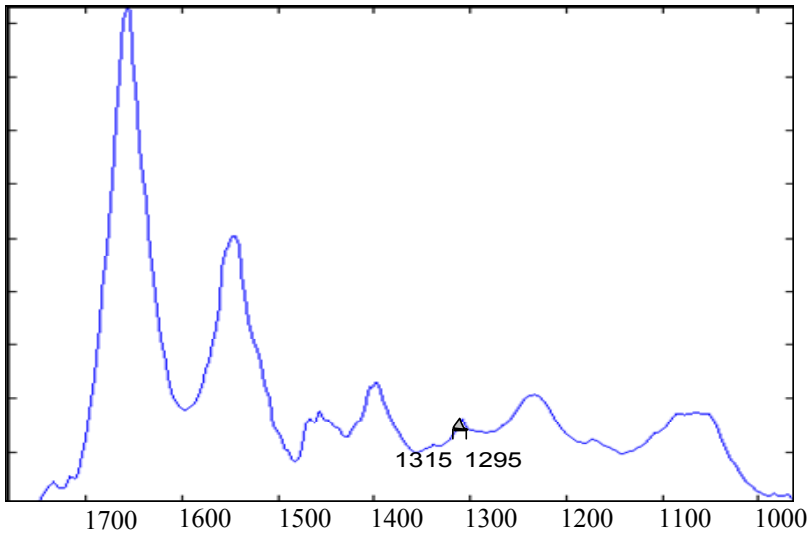

Figure 2.4: Creatine processing parameters in Cytospec

For analysis of plaque using Cytospec, a ratio was taken between the area under the peak between 1630-1620 cm^{-1} and the peak between 1662-1652 cm^{-1} (Figure 2.4). Display limits were set between 0.71-0.45.

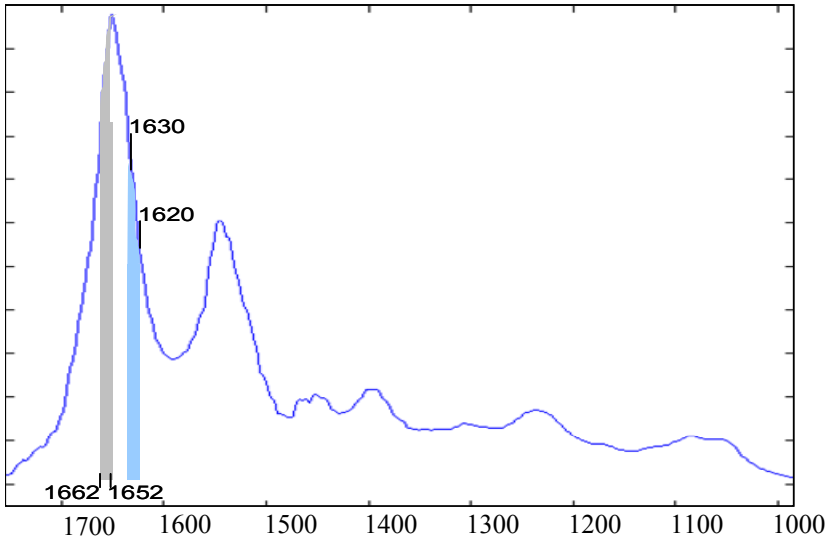

Figure 2.5: Plaque processing parameters in Cytospec

3. Results

Previous and ongoing research in the Gough group has included acquisition and analysis of infrared maps of the plaques that characterize AD (Rak, 2007; Ogg, 2002). When analyzing these maps, it was observed that an anomalous spectrum sometimes overlaid that of normal tissue. This spectrum featured sharp peaks, suggesting a crystalline substance as its origin, and interfered with assessment of β-sheet content as a prominent peak was present in the same region as the amide I absorbance bands.

IR spectra of various potential contaminants were collected in an effort to identify this compound, with no success. A literature search, by Paul Dumas of LURE in Paris, France, suggested a match between the IR spectra of creatine and the unknown compound. This match was confirmed by acquiring IR and Raman spectra of creatine in-house (Figure 3.1).

The maps in which creatine was detected were collected from random locations in the mouse brain, as the focus of this research had been on plaques that were seen on visual inspection of the tissue. As such, it was impossible to assess from these maps whether the creatine deposits were occurring more frequently in the transgenic, as compared to control, mice, or whether the creatine deposits were co-localized with plaques.

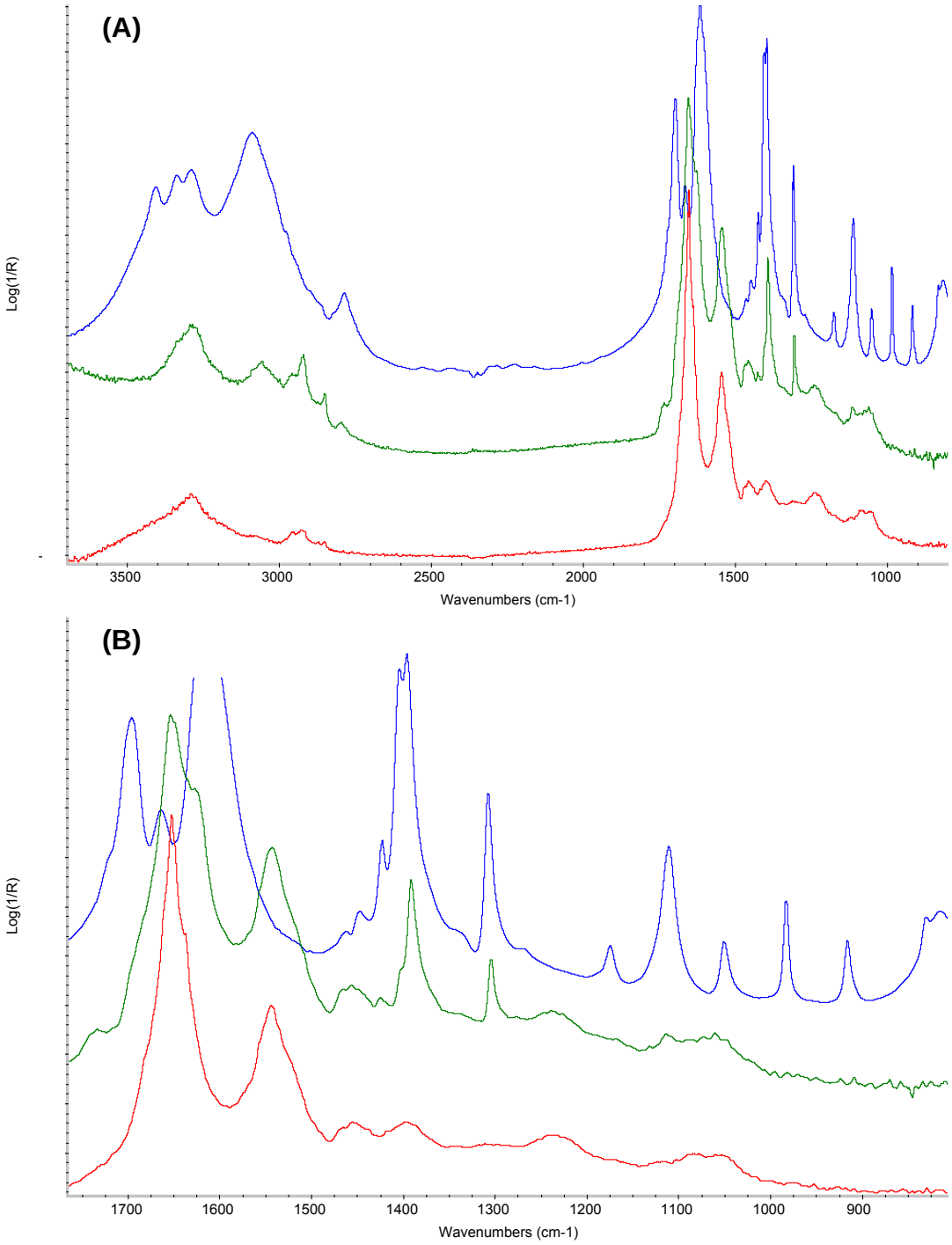

Figure 3.1: Identification of creatine. The infrared spectrum of pure creatine (blue) is shown in the region between 3500-900 cm^{-1} (A) and, enlarged, between 1700-800 cm^{-1} (B). This can be contrasted with the infrared spectrum of a creatine deposit in brain tissue (green) and neuropil (red). The peak at 1304 cm-1 was used for identification of creatine in brain tissue as it is prominent in the spectra of creatine in tissue and is isolated from absorbance bands characteristic of normal tissue.

3.1 Focally elevated creatine is detected in AD mice

In order to gain a better understanding of the distribution and frequency of these deposits, a controlled and systematic study was required. The hippocampus was selected as a region in which to conduct large area surveys because creatine was detected frequently in IR maps of the area, lesions characteristic of AD appear in the region in early stages of disease progression, and the hippocampus is a contained area within the brain, of manageable size (Figure 3.2).

Maps were taken in sequence across large areas (ranging from 3,904,000 to 262,400 μm^2) of the hippocampi of AD mice and their littermate controls, for 7 pairs of mice and one individual mouse. Maps were acquired with both the Nicolet FTIR and microscope with synchrotron light source and the Bruker Tensor 21 FTIR and Hyperion microscope with globar lightsource. The time needed to acquire sufficient maps to cover a full hippocampus was up to one week using the Nicolet FTIR and microscope and synchrotron source with 10 μm by 10 μm pixels, or up to one month, using the Bruker FTIR and microscope and globar source with lower spatial resolution, 25 μm by 25 μm pixels.

Maps were processed for levels of creatine and β-sheet signal, and processed maps were tiled together to reveal the distribution of creatine and β-sheet across the area surveyed. These tiled maps were compared to photographs of the tissue to identify the location of creatine deposits and plaques, and to compare the locations of both, in case of co-localization (Figures 3.3-3.21).

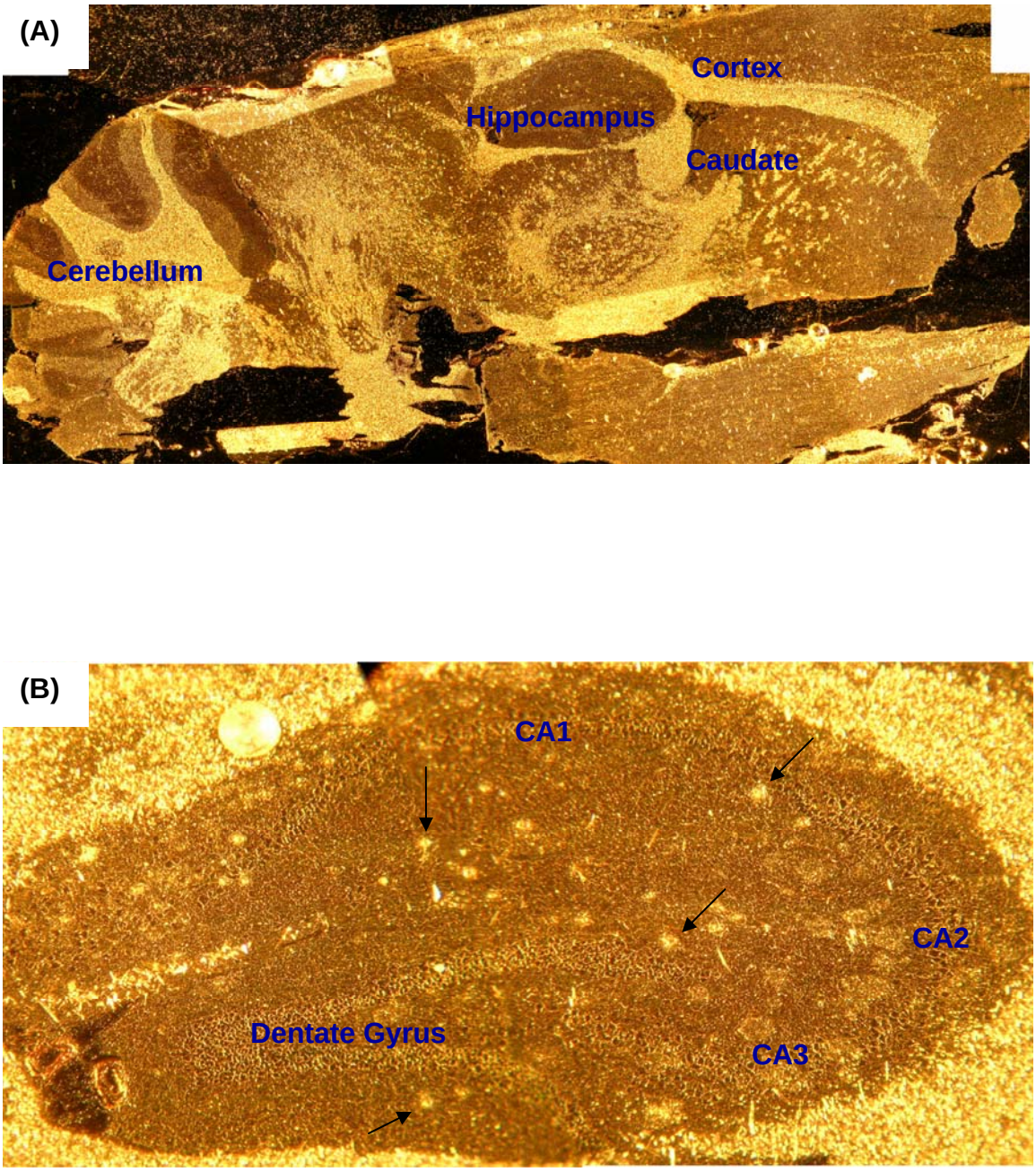

Figure 3.2: Sagittal sections of the Tg mouse brain and hippocampus. (A) Sagittal section of transgenic mouse brain showing major regions of interest and (B) a close up of the hippocampus. The small white spots such as those indicated with arrows are visible indications of plaque locations. The tissue is unstained, flash frozen, sectioned at 8 μm, and mounted on gold coated silicon wafers.

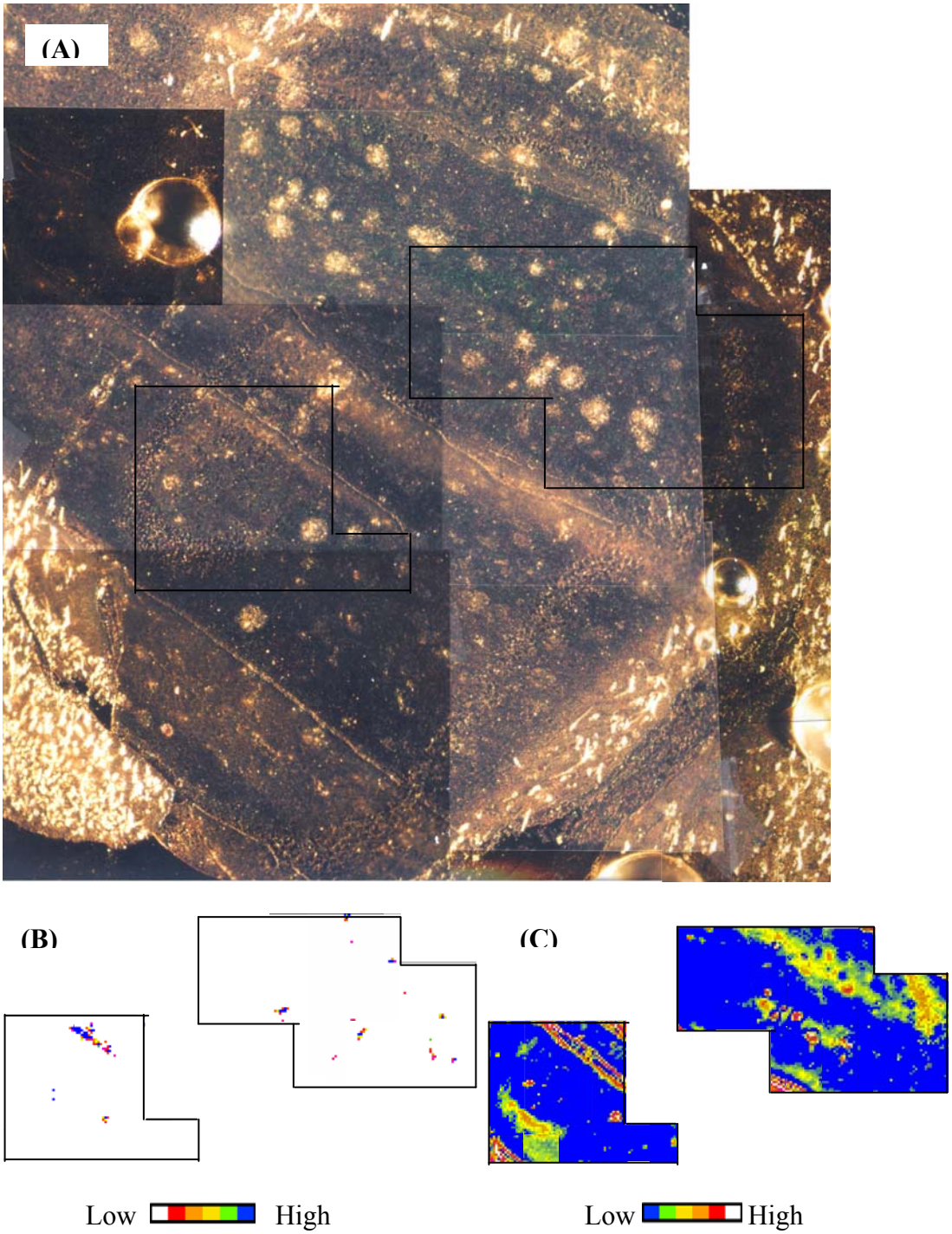

Figure 3.3: Creatine and plaque distribution in the hippocampus of A01. The region of the hippocampus surveyed is outlined in image (A). Creatine distribution is represented in (B) and β-sheet distribution in (C). A01 is a transgenic mouse, littermate to A02, and plaques can be seen throughout the tissue (appearing as white spots). As this section was acquired deep in the brain, the beginning of the connection to the second hippocampal lobe is present.

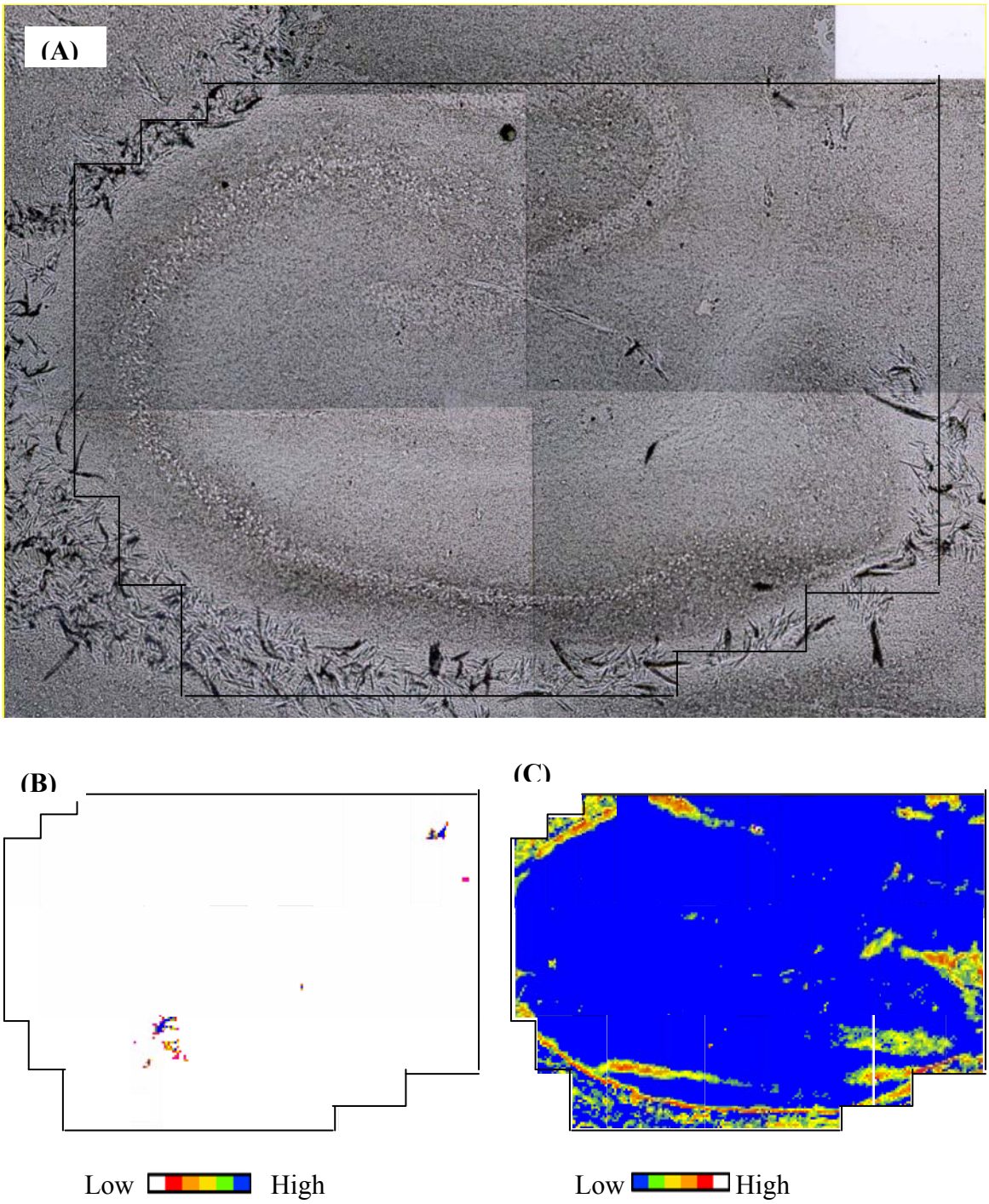

Figure 3.4: Creatine and plaque distribution in the hippocampus of A02. The region of the hippocampus surveyed is outlined in image (A). Creatine distribution is represented in (B) and β-sheet distribution in (C). False-positive for β-sheet signal due to lipid content is evident in (C) (Rak, 2007; Rak et al, 2007). A02 is a non-transgenic mouse, littermate to A01. The tissue in this sample is visibly smoother, and without lesions, as compared to A01.

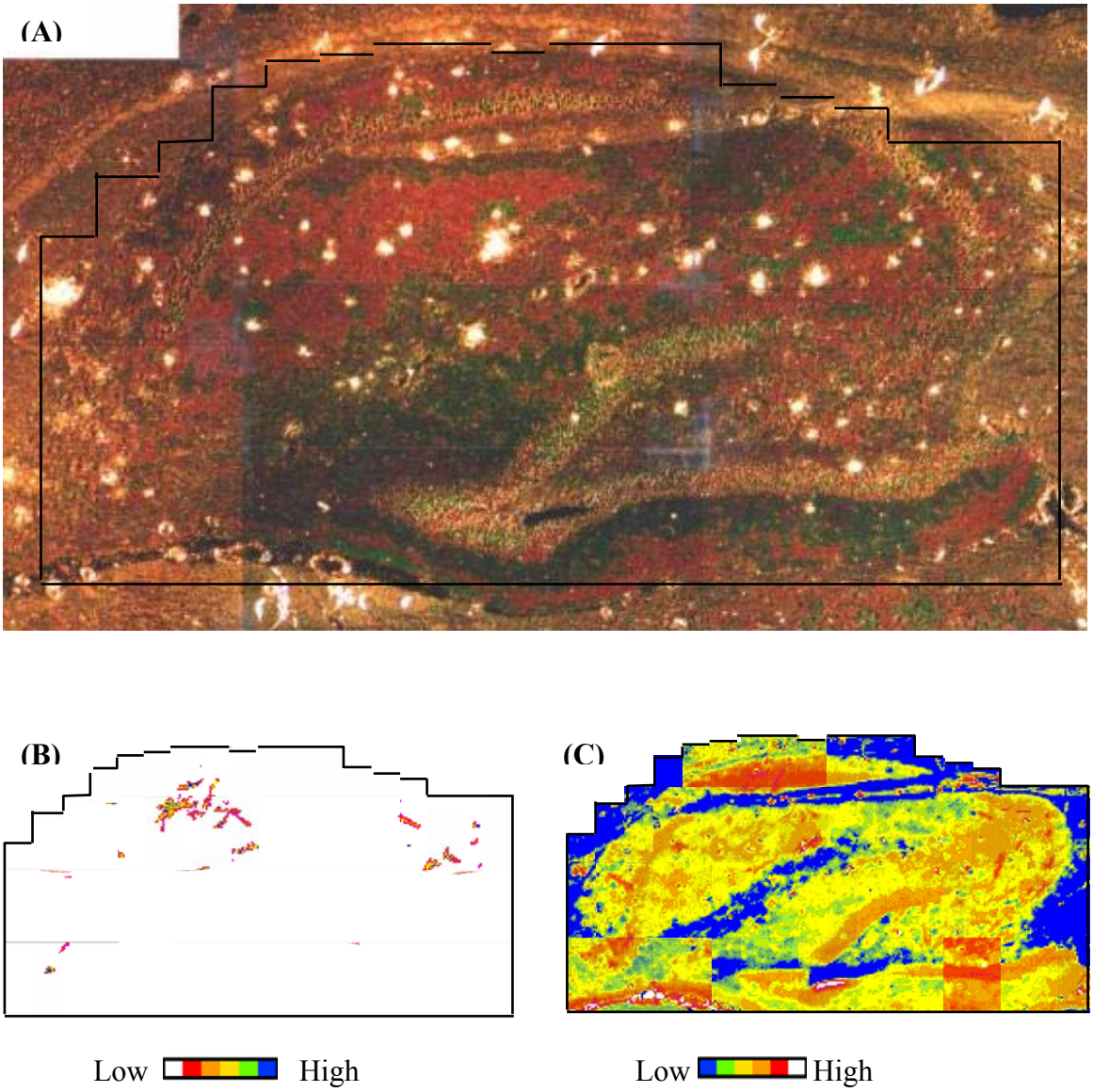

Figure 3.5: Creatine and plaque distribution in the hippocampus of A03. The region of the hippocampus surveyed is outlined in image (A). Creatine distribution is represented in (B) and β-sheet distribution in (C). A03 is a transgenic mouse, littermate to A04. Many dense-core plaques are visible as bright white spots throughout the tissue.

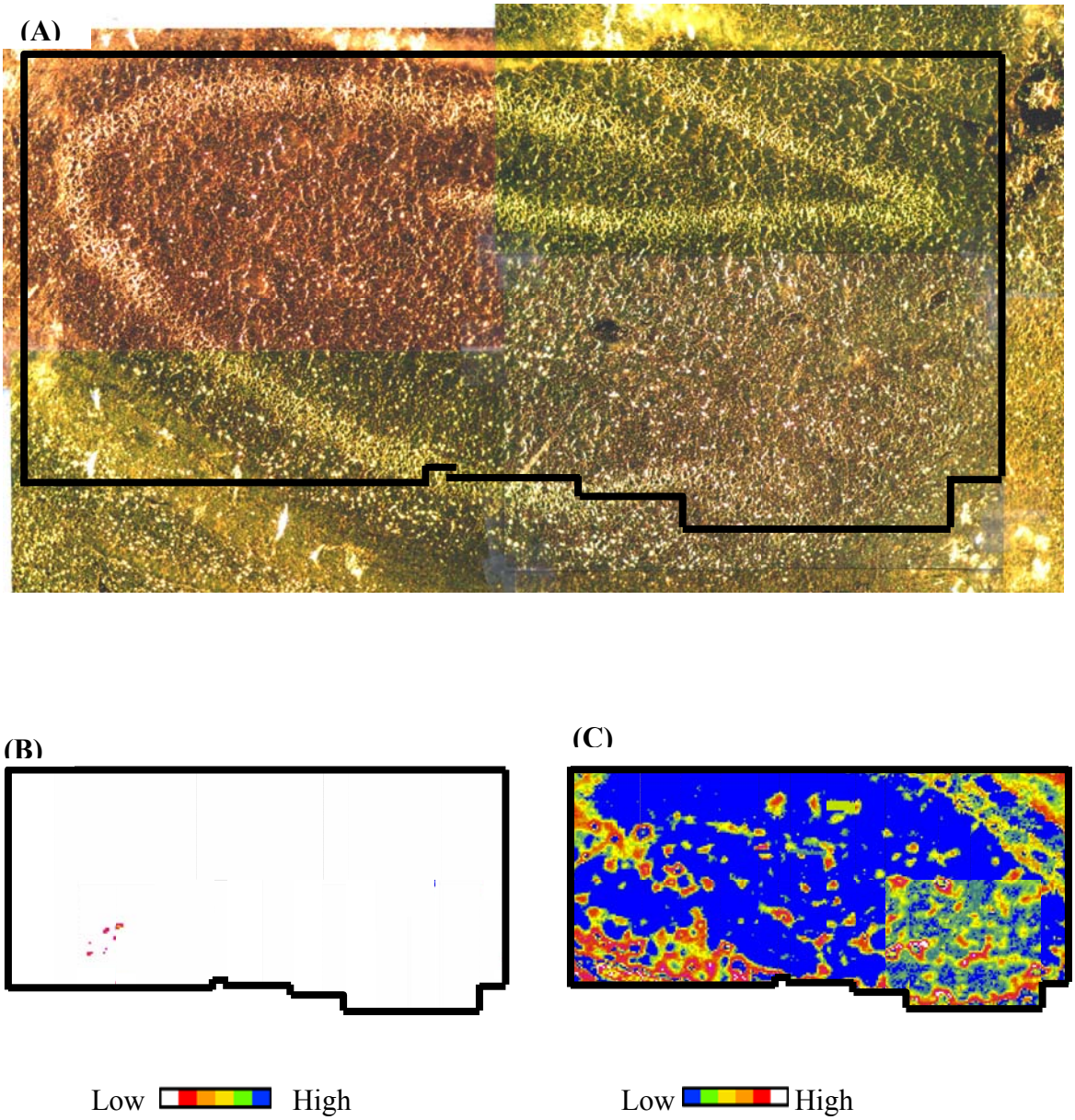

Figure 3.6: Creatine and plaque distribution in the hippocampus of A04. The region of the hippocampus surveyed is outlined in image (A). Creatine distribution is represented in (B) and β-sheet distribution in (C). False-positive for β-sheet signal due to lipid content is evident in (C) (Rak, 2007; Rak et al, 2007). A04 is a non-transgenic mouse, littermate to A03.

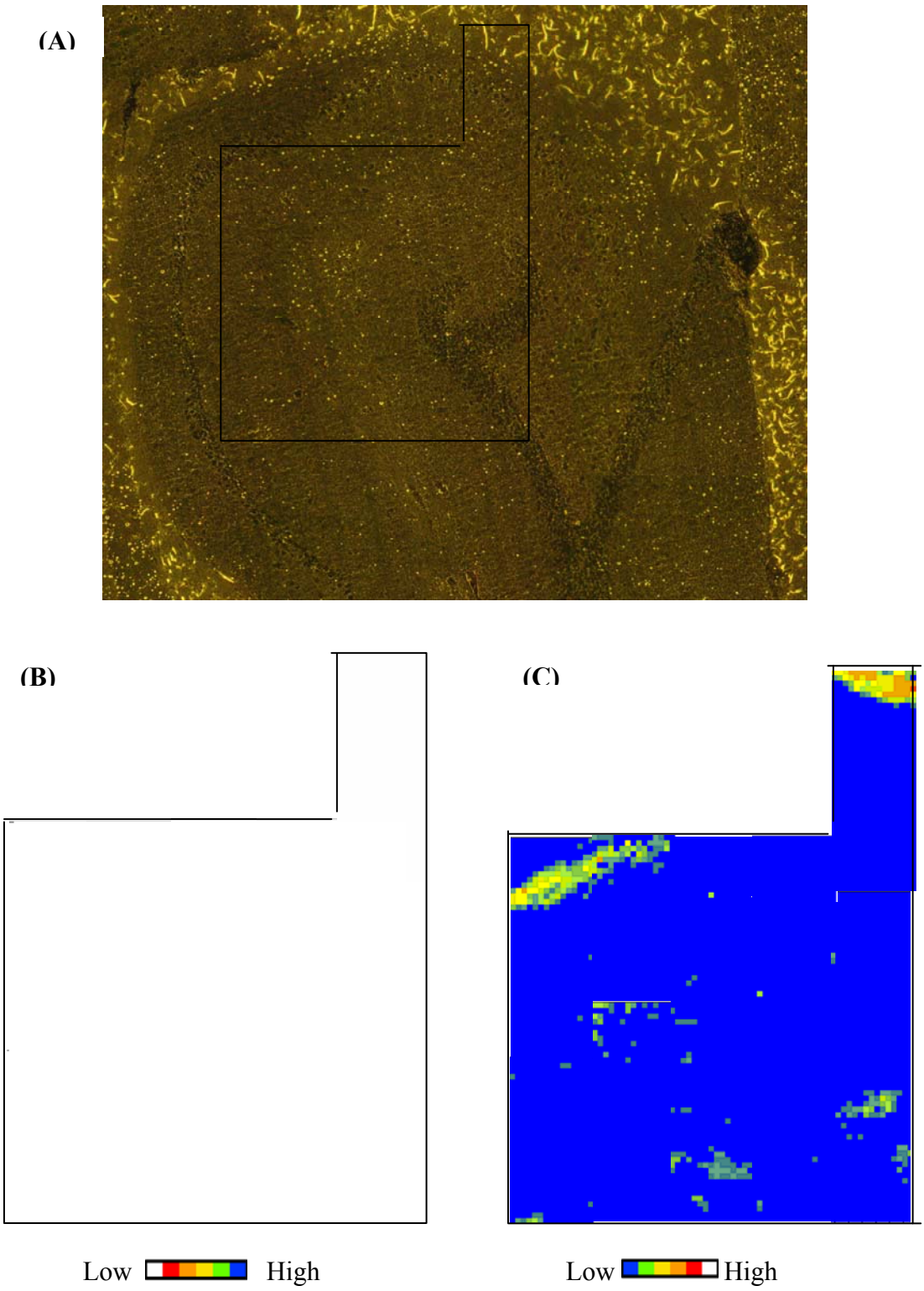

Figure 3.7: Creatine and plaque distribution in the hippocampus of A06. The region of the hippocampus surveyed is outlined in image (A). Creatine distribution is represented in (B) and β-sheet distribution in (C). A06 is a non-transgenic mouse, but the Tg littermate has not been surveyed yet.

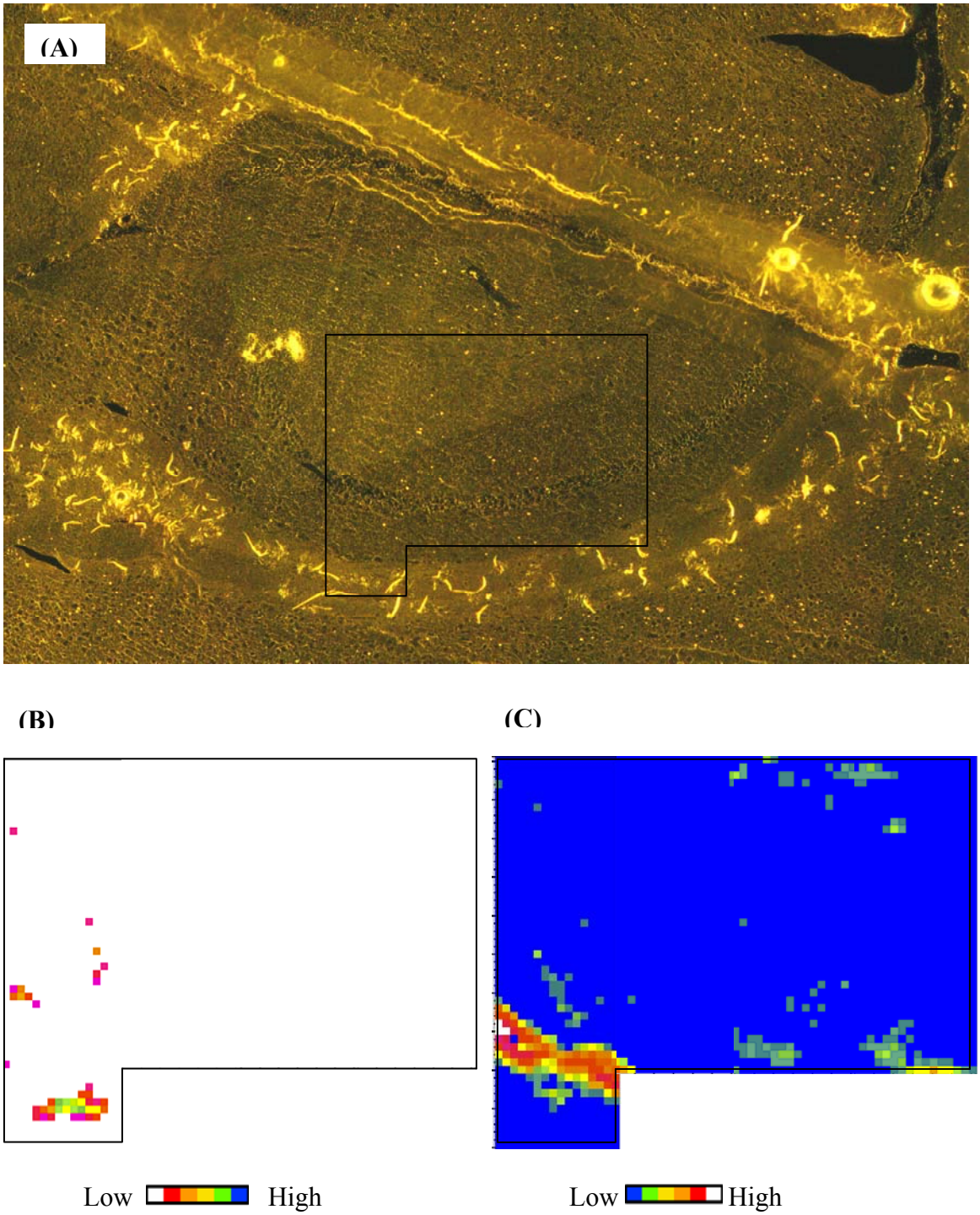

Figure 3.8: Creatine and plaque distribution in the hippocampus of A10. The region of the hippocampus surveyed is outlined in image (A). Creatine distribution is represented in (B) and β-sheet distribution in (C). False-positive for β-sheet signal due to lipid content is evident in (C) (Rak, 2007; Rak et al, 2007). A10 is a non-transgenic mouse, littermate to A11.

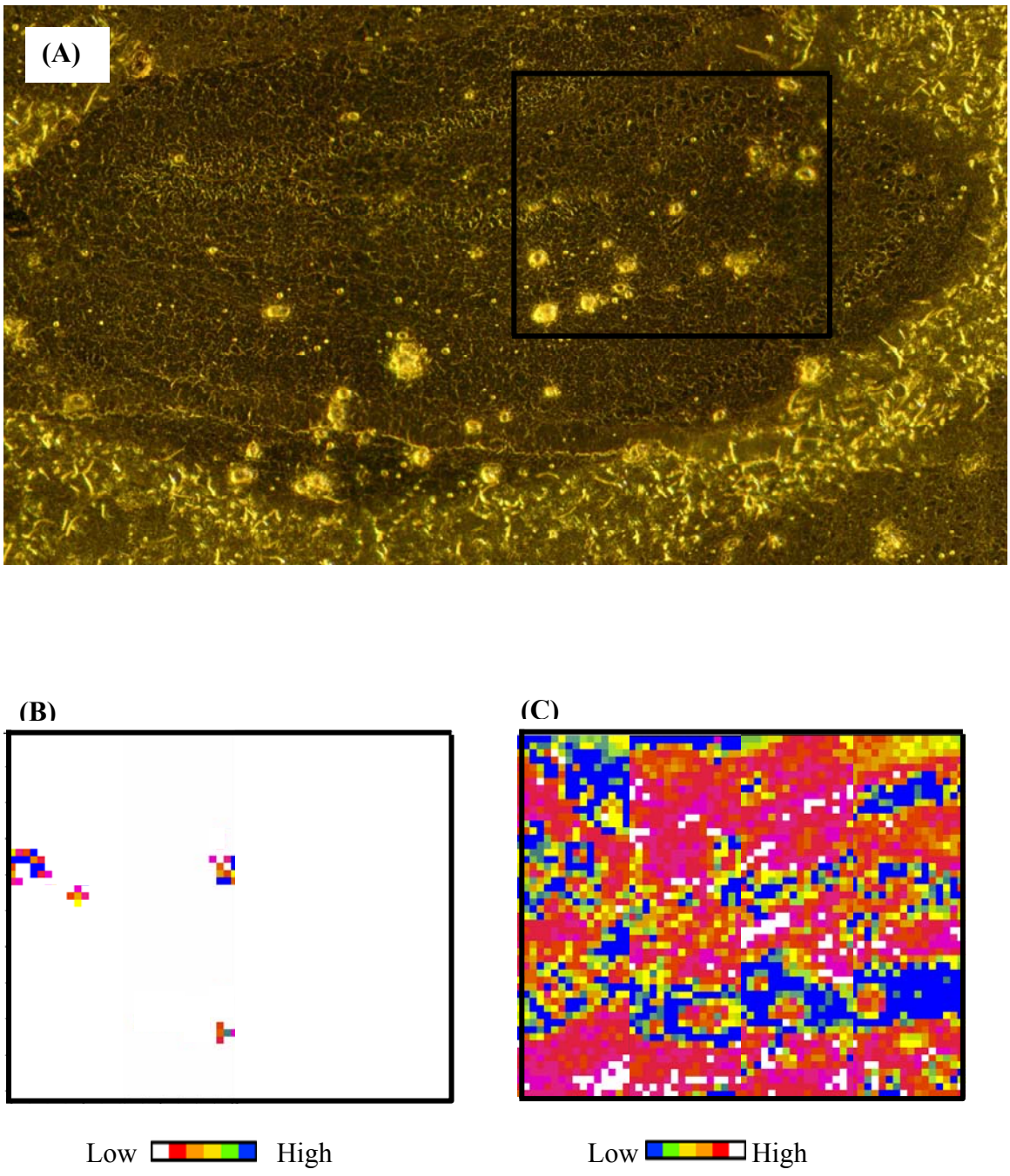

Figure 3.9: Creatine and plaque distribution in the hippocampus of A11. The region of the hippocampus surveyed is outlined in image (A). Creatine distribution is represented in (B) and β-sheet distribution in (C). A11 is a non-transgenic mouse, littermate to A10.

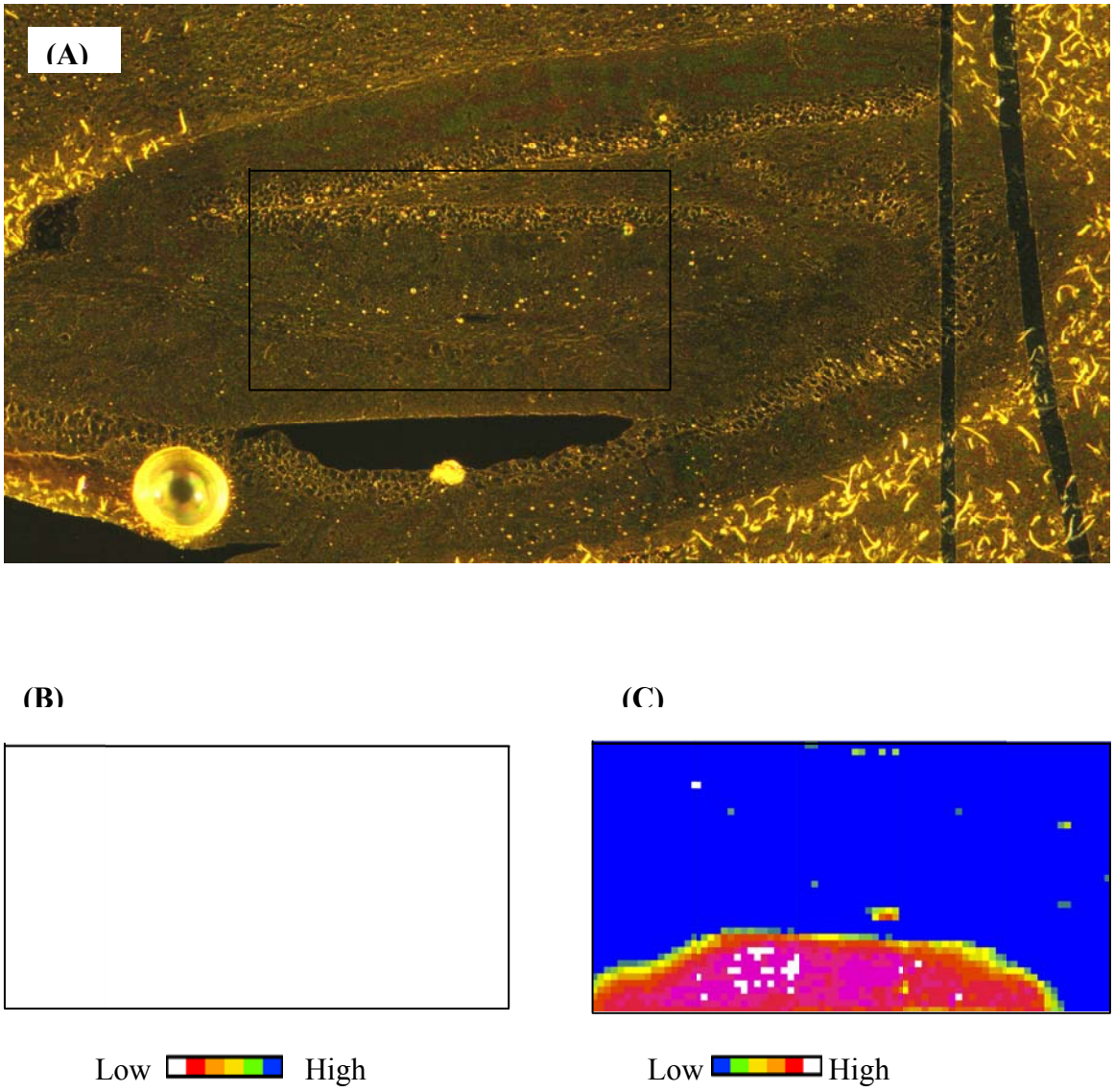

Figure 3.10: Creatine and plaque distribution in the hippocampus of A13. The region of the hippocampus surveyed is outlined in image (A). Creatine distribution is represented in (B) and β-sheet distribution in (C). A13 is a non-transgenic mouse, littermate to A14. The tissue immediately above the hole visible in (A) is compressed, and the resulting dense tissue gives a false-positive β-sheet signal in (C).

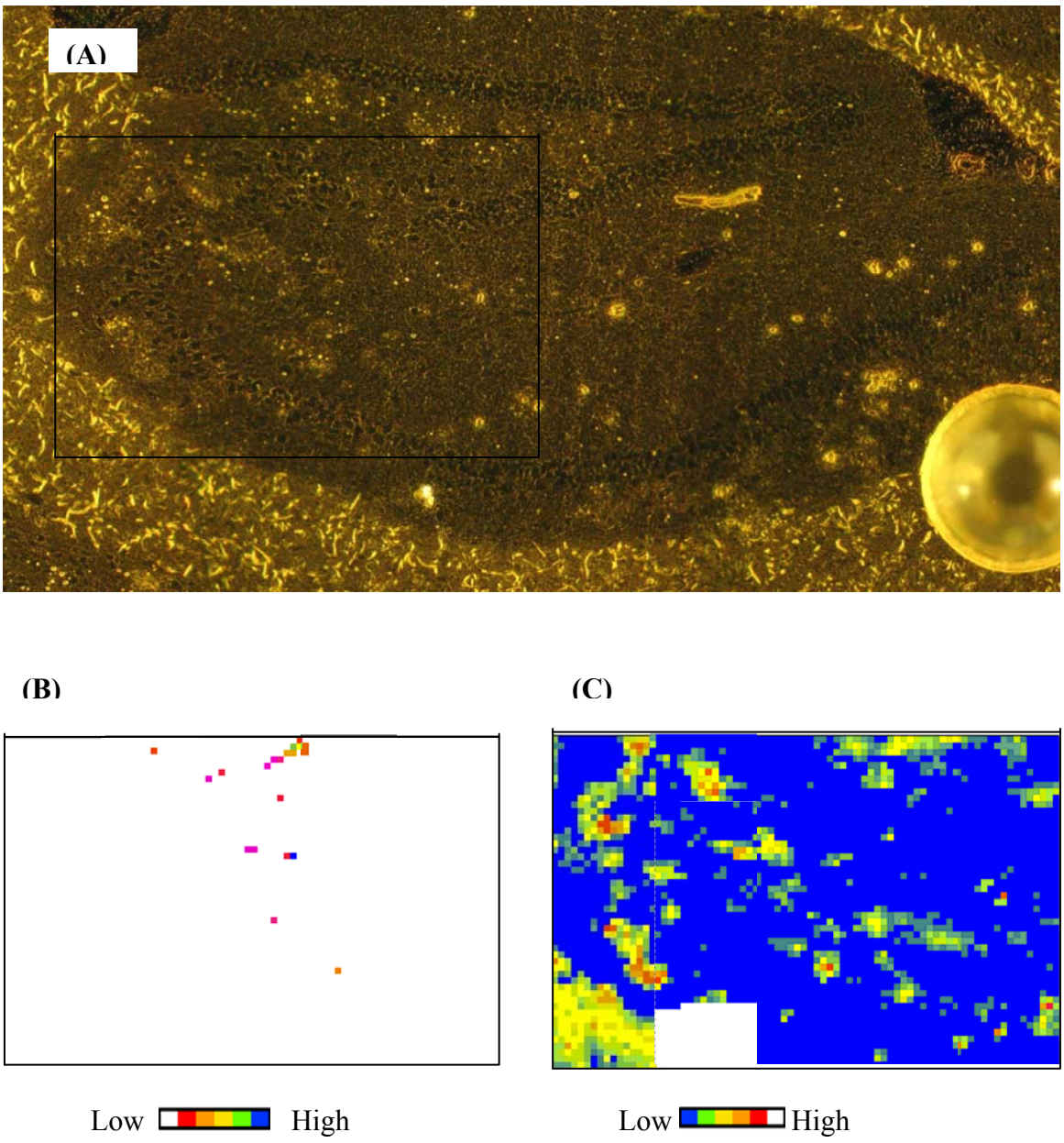

Figure 3.11: Creatine and plaque distribution in the hippocampus of A14. The region of the hippocampus surveyed is outlined in image (A). Creatine distribution is represented in (B) and β-sheet distribution in (C). A14 is a transgenic mouse, littermate to A13. One small map could not be transferred out of Omnic.

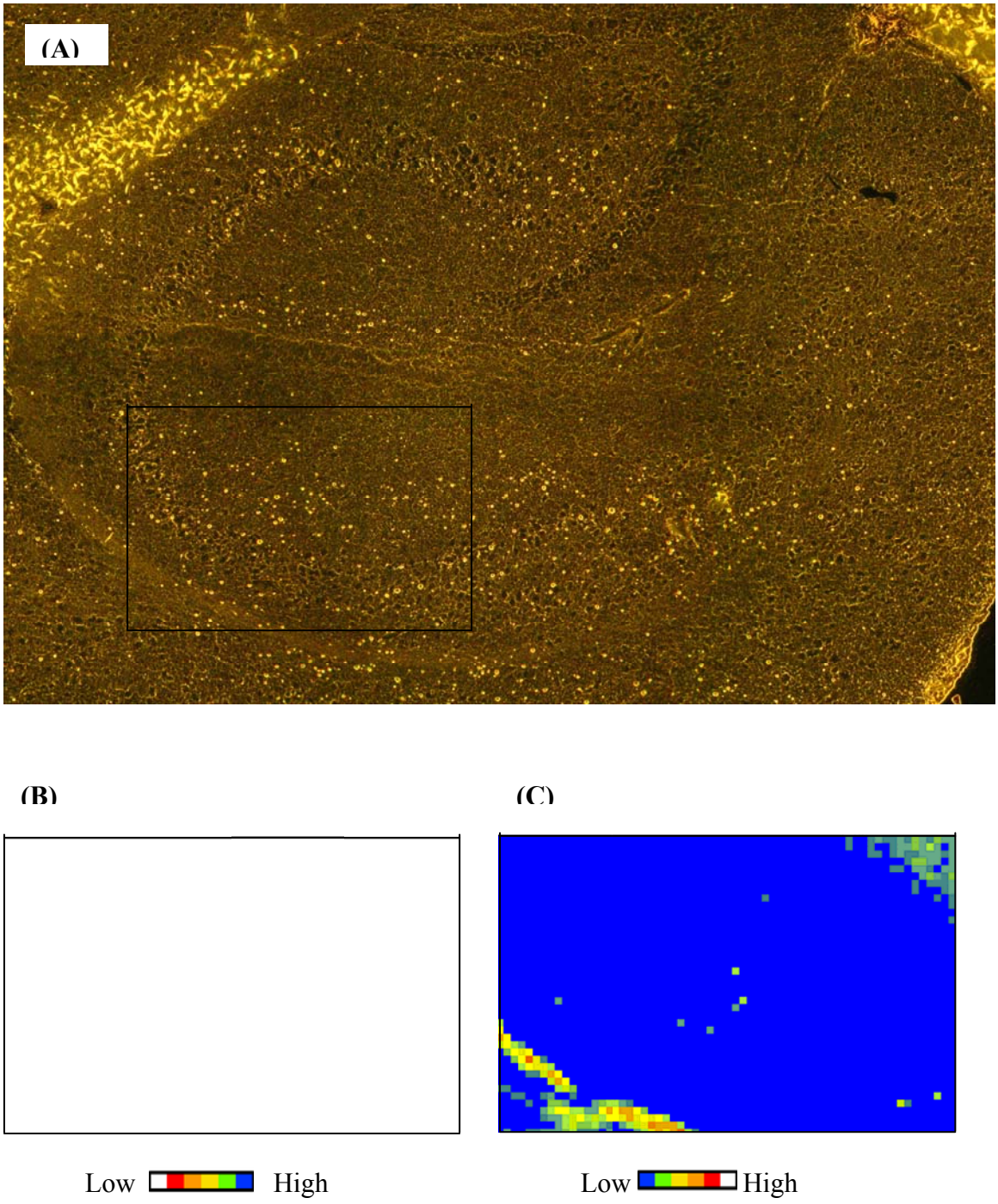

Figure 3.12: Creatine and plaque distribution in the hippocampus of A15. The region of the hippocampus surveyed is outlined in image (A). Creatine distribution is represented in (B) and β-sheet distribution in (C). False-positive for β-sheet signal due to lipid content is evident in (C) (Rak, 2007; Rak et al, 2007). A15 is a non-transgenic mouse, littermate to A16.

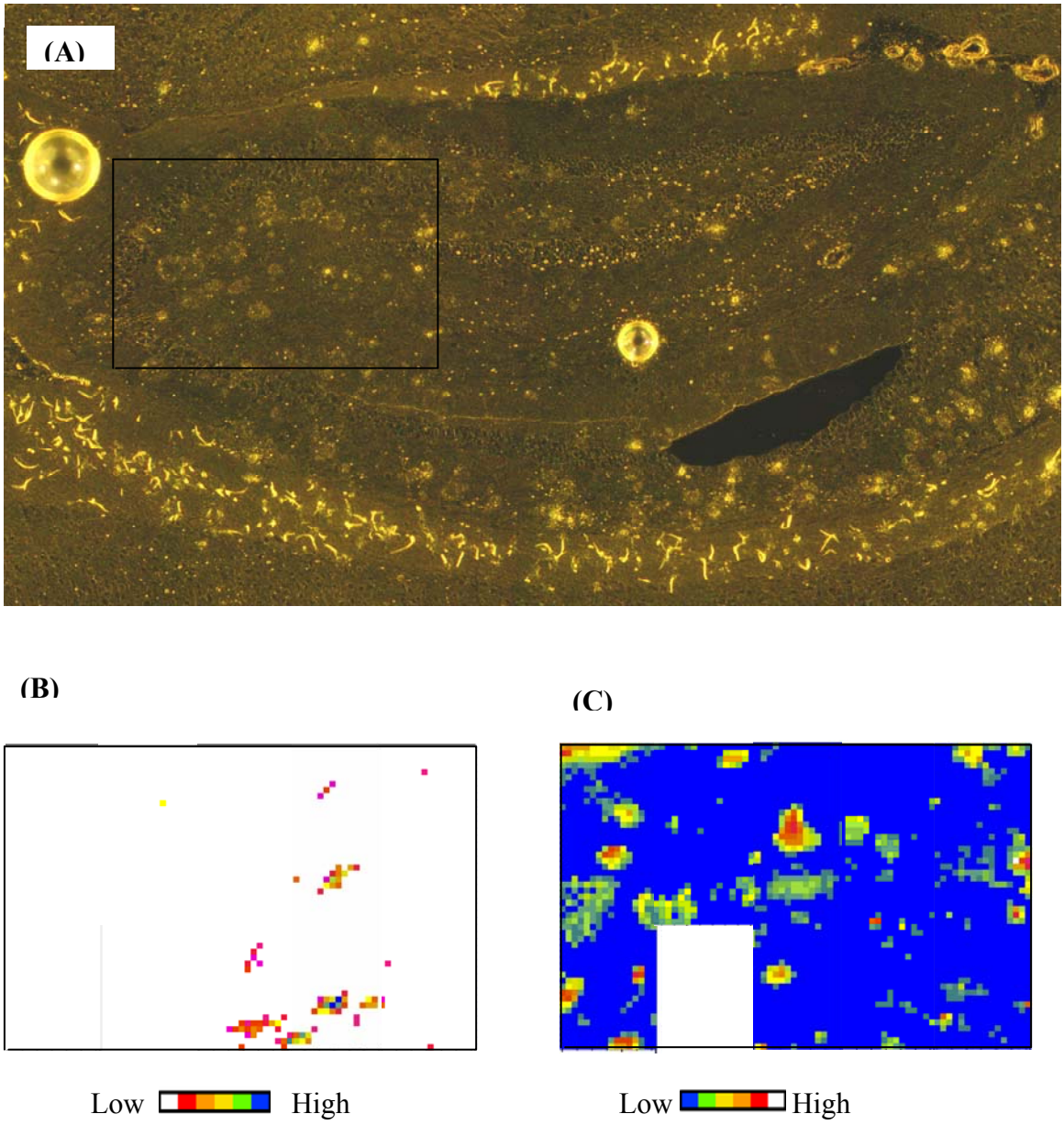

Figure 3.13: Creatine and plaque distribution in the hippocampus of A16. The region of the hippocampus surveyed is outlined in image (A). Creatine distribution is represented in (B) and β-sheet distribution in (C). A16 is a transgenic mouse, littermate to A15. One map could not be transferred out of Omnic.

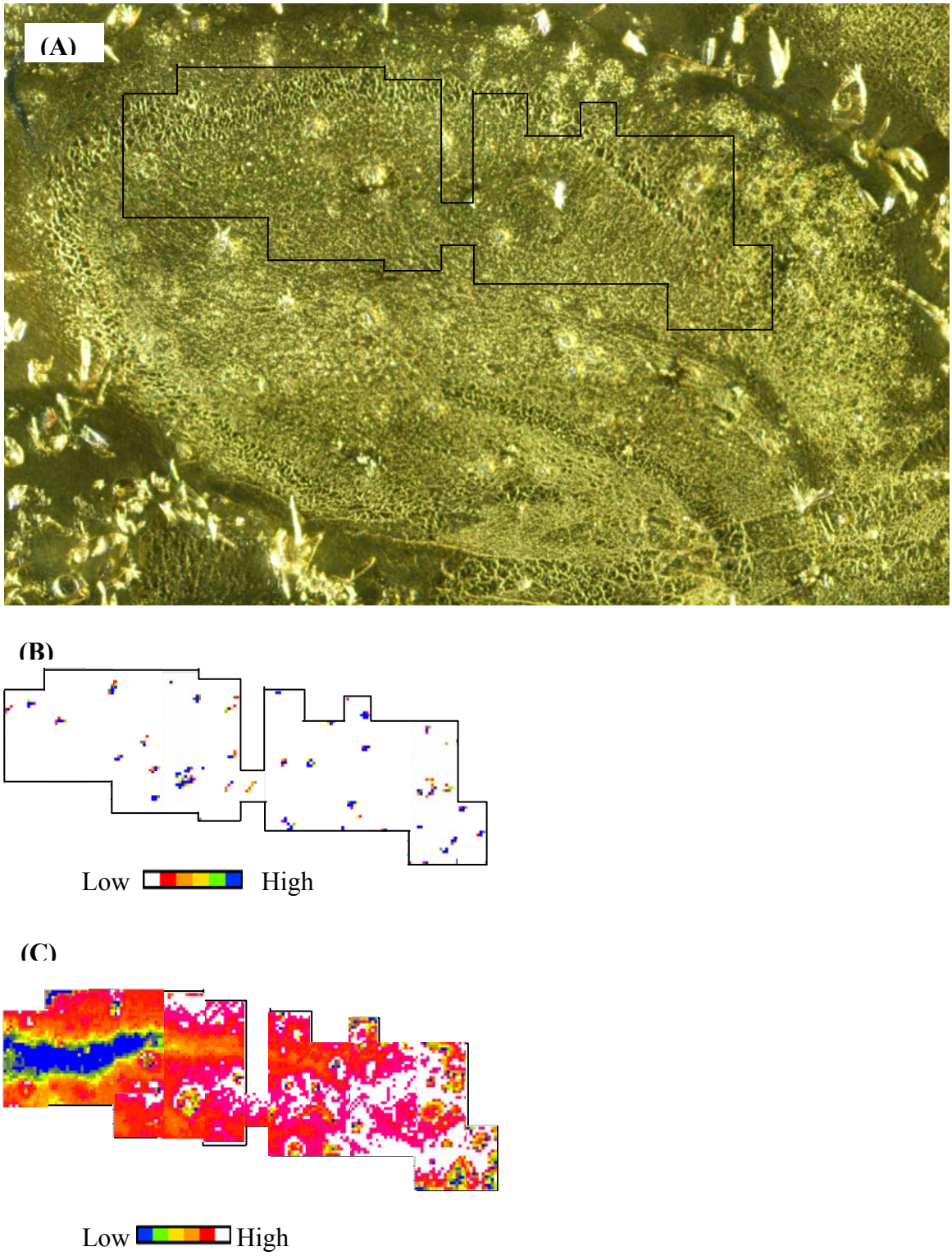

Figure 3.14: Creatine and plaque distribution in the hippocampus of A22. The region of the hippocampus surveyed is outlined in image (A). Creatine distribution is represented in (B) and β-sheet distribution in (C). A22 is a transgenic mouse, littermate to A23. The tissue from this sample was exceptionally dense.

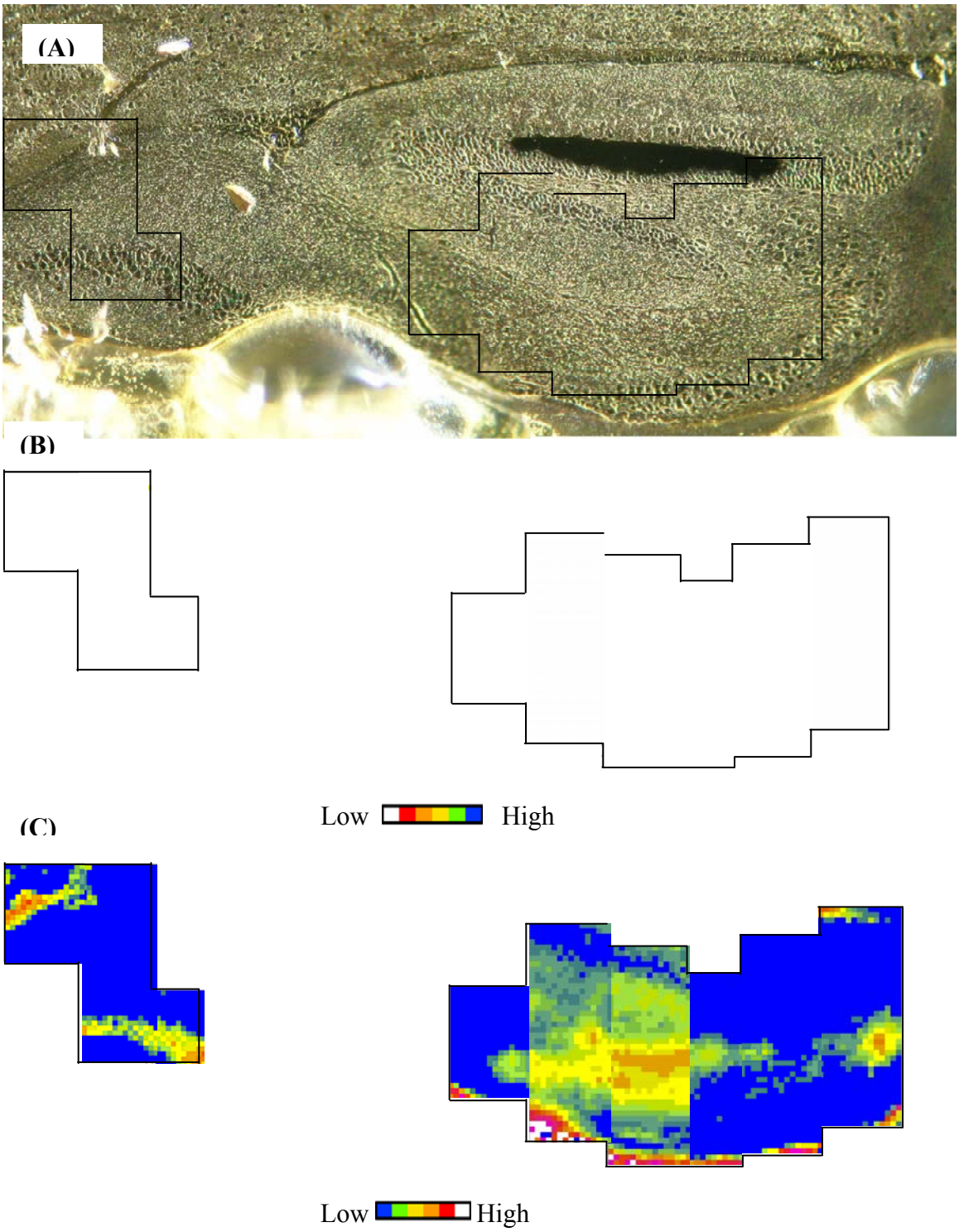

Figure 3.15: Creatine and plaque distribution in the hippocampus of A23. The region of the hippocampus surveyed is outlined in image (A). Creatine distribution is represented in (B) and β-sheet distribution in (C). False-positive for β-sheet signal due to lipid content is evident in (C) (Rak, 2007; Rak et al, 2007). A23 was a non-transgenic mouse, littermate to A22.

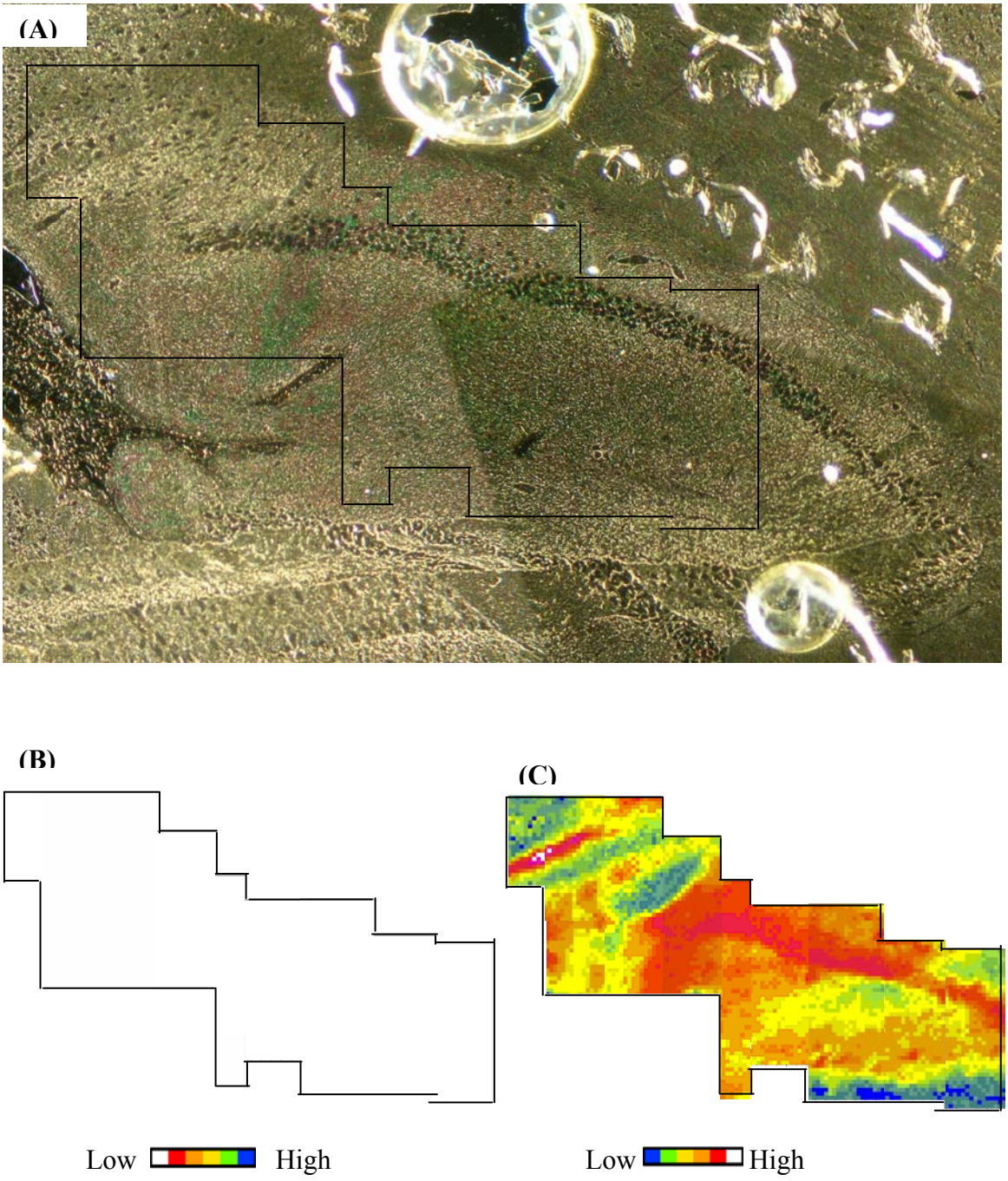

Figure 3.16: Creatine and plaque distribution in the hippocampus of A24. The region of the hippocampus surveyed is outlined in image (A). Creatine distribution is represented in (B) and β-sheet distribution in (C). A24 is a non-transgenic mouse, littermate to A25.

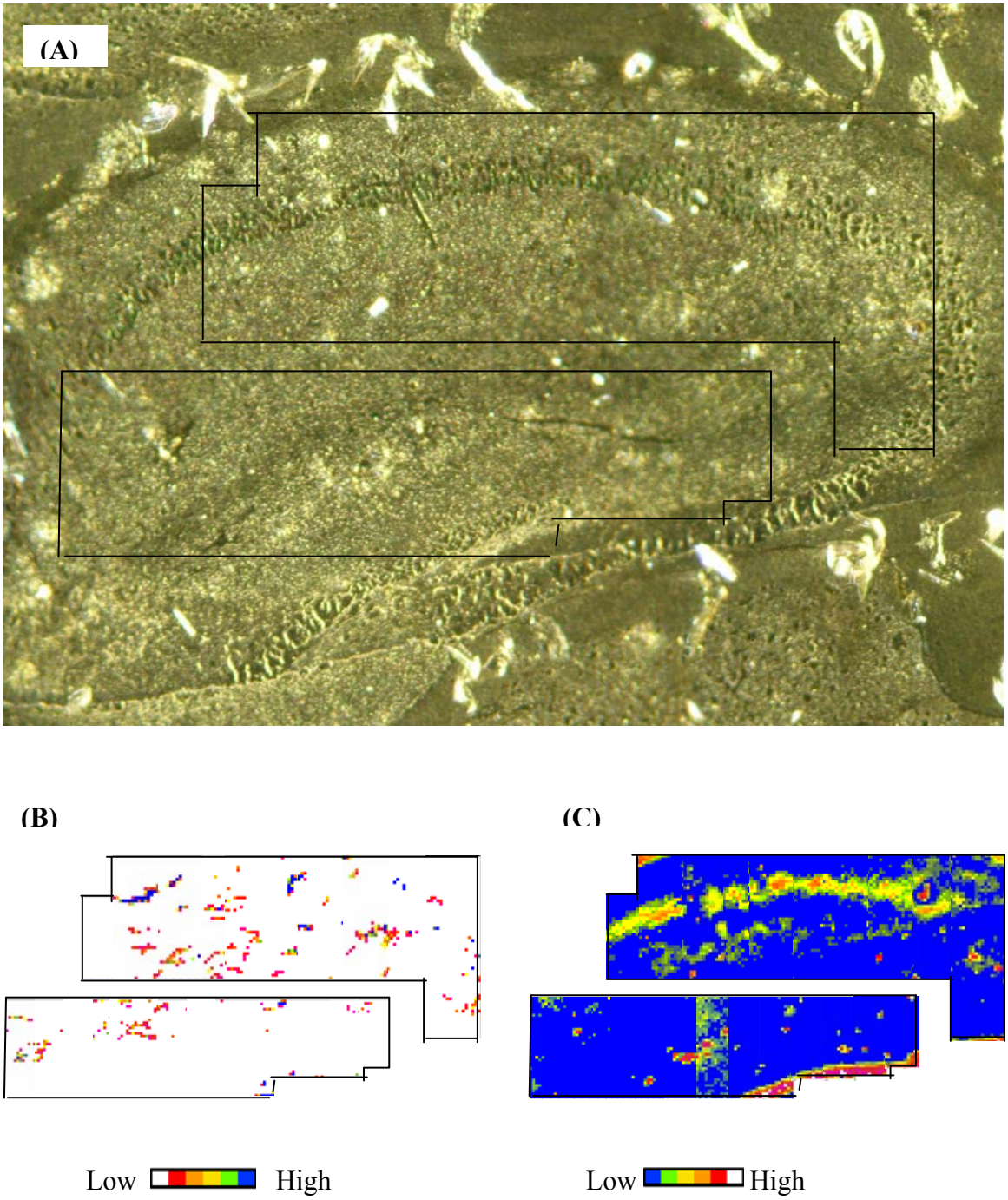

Figure 3.17: Creatine and plaque distribution in the hippocampus of A25. The region of the hippocampus surveyed is outlined in image (A). Creatine distribution is represented in (B) and plaque distribution in (C). A25 is a transgenic mouse, littermate to A24.

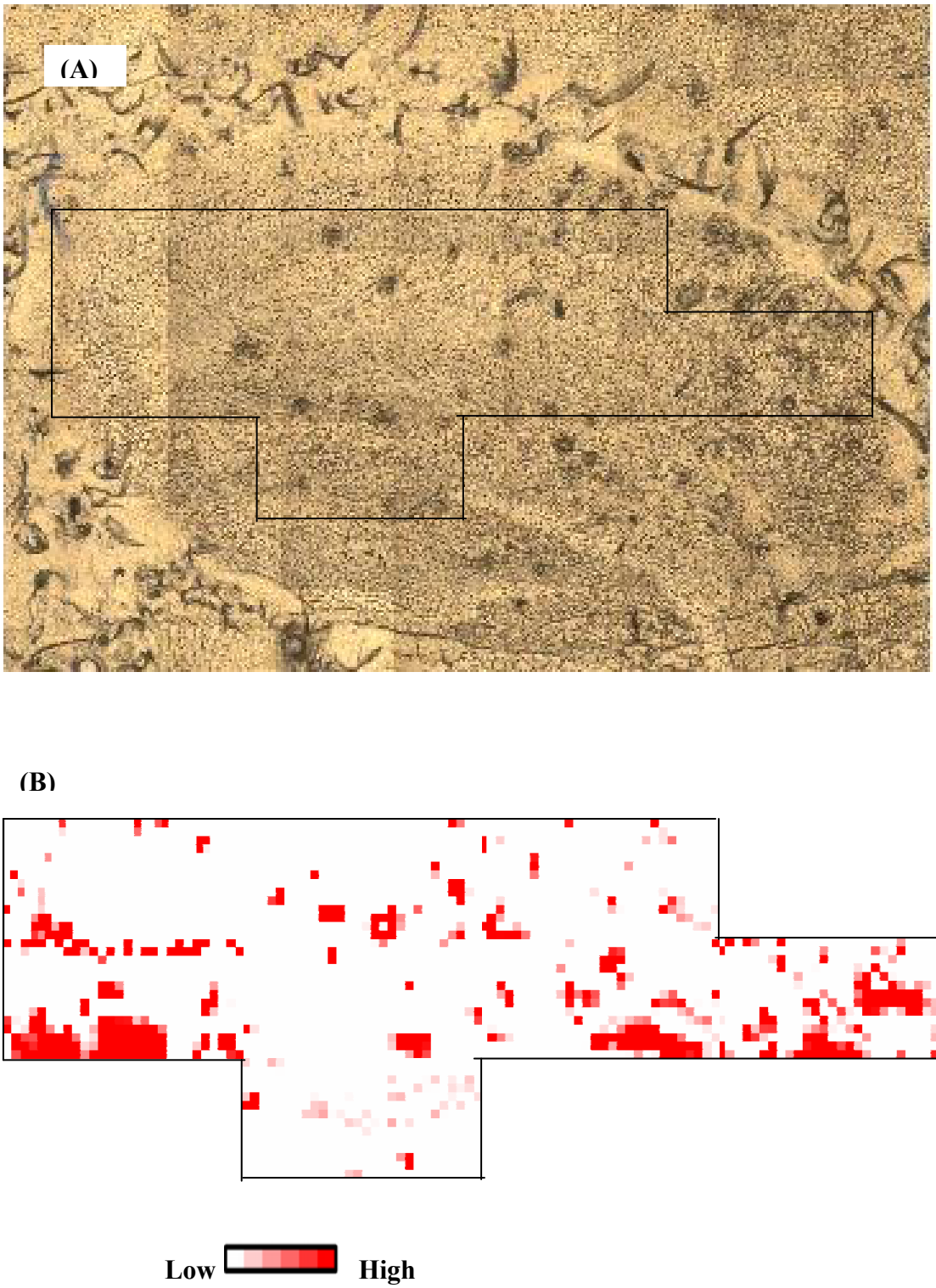

Figure 3.18: Creatine distribution in the hippocampus of A22 from globar light source. The region of the hippocampus surveyed is outlined in image (A). Creatine distribution is represented in (B). Pixel size is 25µm x 25µm. A22 is a transgenic mouse, littermate to A23.

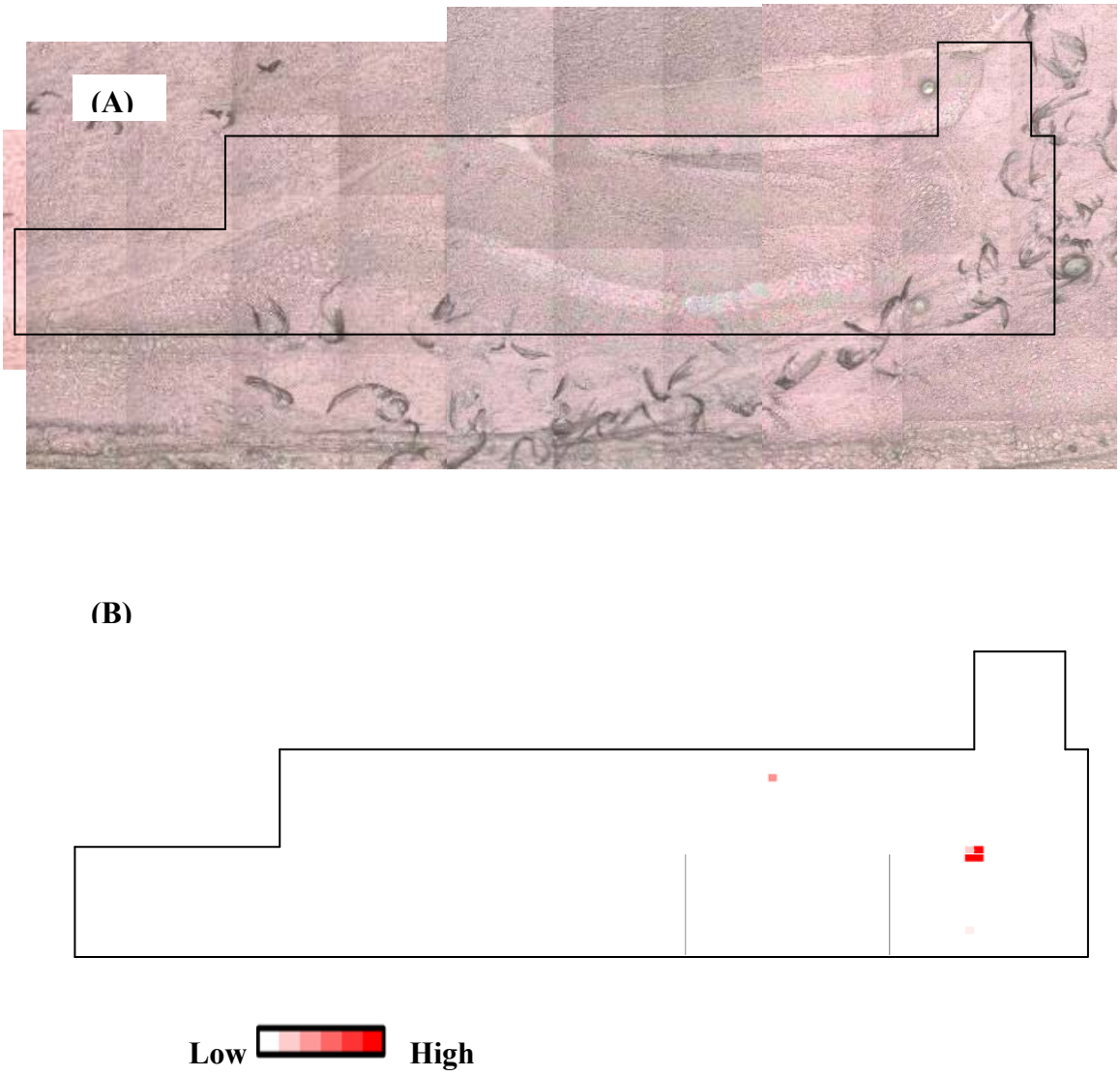

Figure 3.19: Creatine distribution in the hippocampus of A23 from globar light source. The region of the hippocampus surveyed is outlined in image (A). Creatine distribution is represented in (B). Pixel size is 25µm x 25µm. A23 is a non-transgenic mouse, littermate to A22.

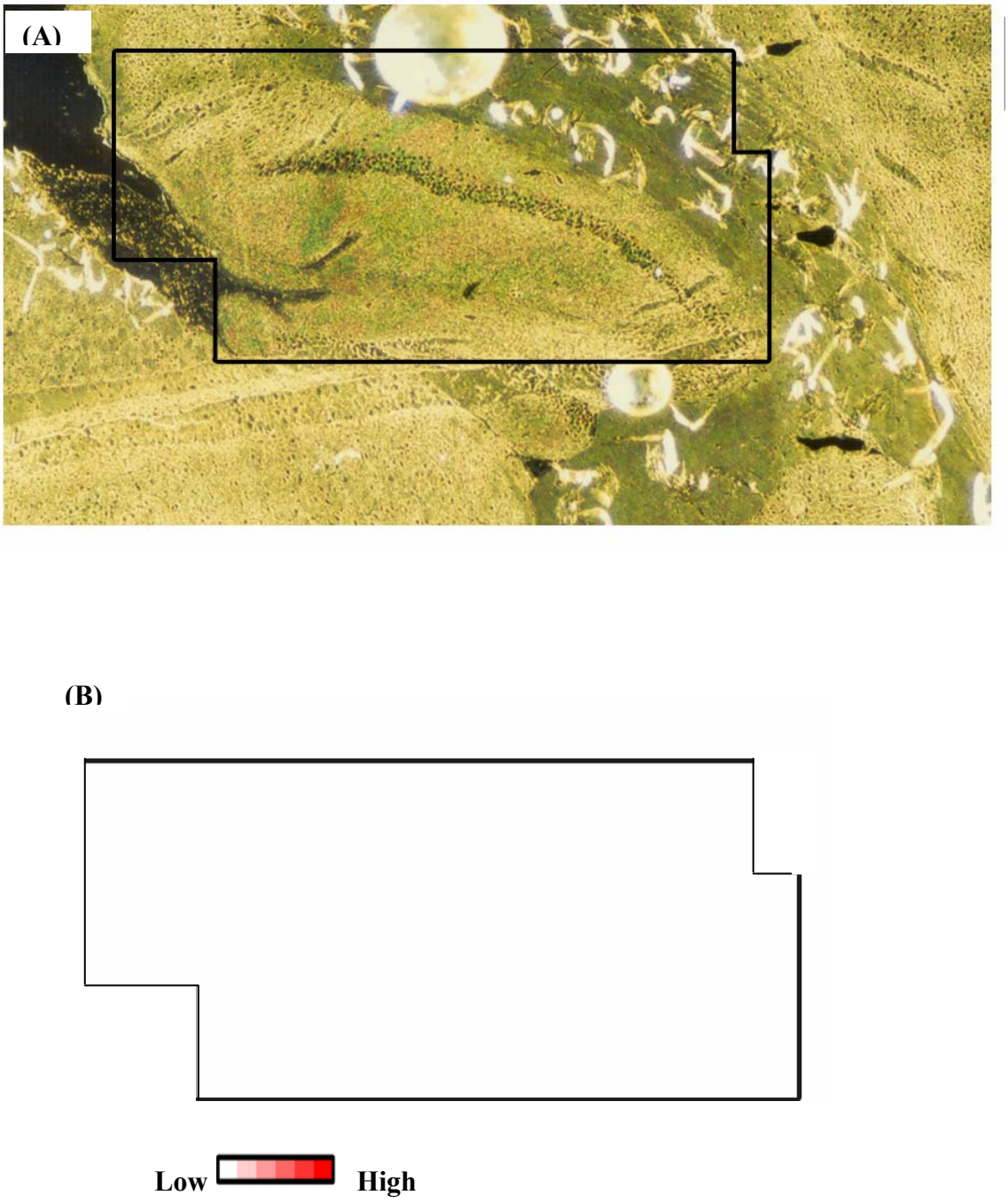

Figure 3.20: Creatine distribution in the hippocampus of A24 from globar light source. The region of the hippocampus surveyed is outlined in image (A). Creatine distribution is represented in (B). Pixel size is 25µm x 25µm. A24 is a non-transgenic mouse, littermate to A25.

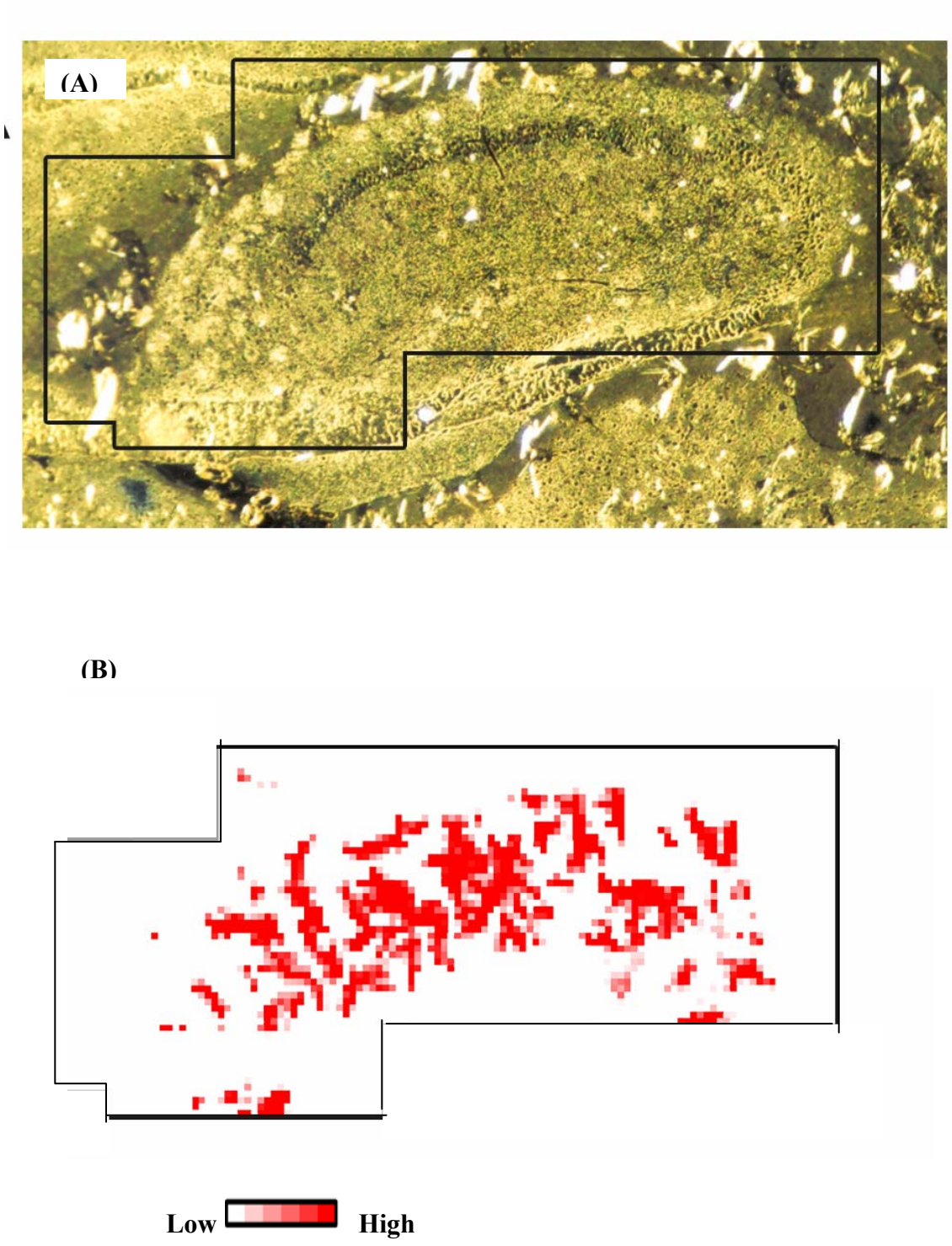

Figure 3.21: Creatine distribution in the hippocampus of A25 from globar light source. The region of the hippocampus surveyed is outlined in image (A). Creatine distribution is represented in (B). Pixel size is 25µm x 25µm. A25 is a transgenic mouse, littermate to A24.

Each pixel that was coloured to indicate the presence of creatine was checked to ensure no false-postives. Visual inspection of processed maps shows that creatine is found in localized deposits throughout the hippocampi of the mice. These deposits are focally elevated in transgenic, as compared to control, mice. Despite the increased frequency of the deposits in transgenic mice, the distribution of creatine in these mice does not mimic the distribution of plaques: the deposits are not co-localized with one another. Although percentages vary between sets of mice, creatine was detected in a greater percentage of pixels in transgenic mice, as compared to their littermate controls (Table 3.1).

Table 3.1: Number of pixels containing creatine across area of hippocampus surveyed using Nicolet FTIR and microscope with synchrotron light source.

Mouse	AD/Control	Age (Days)	Total Pixels	Pixels Creatine	% Creatine
A01	TgCRND8	624	11188	120	1.07
A02	Control	624	31456	152	0.48
A03	TgCRND8	504	39040	907	2.32
A04	Control	504	31009	34	0.11
A06	Control	478	5730	0	0.00
A10	Control	457	2784	41	1.47
A11	TgCRND8	457	3264	39	1.19
A13	Control	429	3280	0	0.00
A14	TgCRND8	429	4080	23	0.56
A15	Control	429	2624	0	0.00
A16	TgCRND8	429	4080	98	2.40
A22	Tg19959	266	7882	220	2.79
A23	Control	266	4150	1	0.02
A24	Control	241	5996	0	0.00
A25	Tg19959	241	10819	1507	13.93

As the focus of this research was on the identification of creatine deposits within brain tissue, data were acquired with the minimum number of spectra summed that would

allow appropriate signal/noise to identify creatine. The number of spectra summed was kept to a minimum to ensure the maximum area of the brain could be scanned during the time available at the synchrotron light source. The signal/noise that was appropriate for detection of creatine was insufficient to obtain high quality spectra of dense-core plaque and dense tissue surrounding plaques (Figure 3.22). As a result, the quality of maps processed for β-sheet content is vulnerable to the density of, or presence of lesions in, tissue and many of the processed maps display colour schemes that may not accurately represent plaque levels.

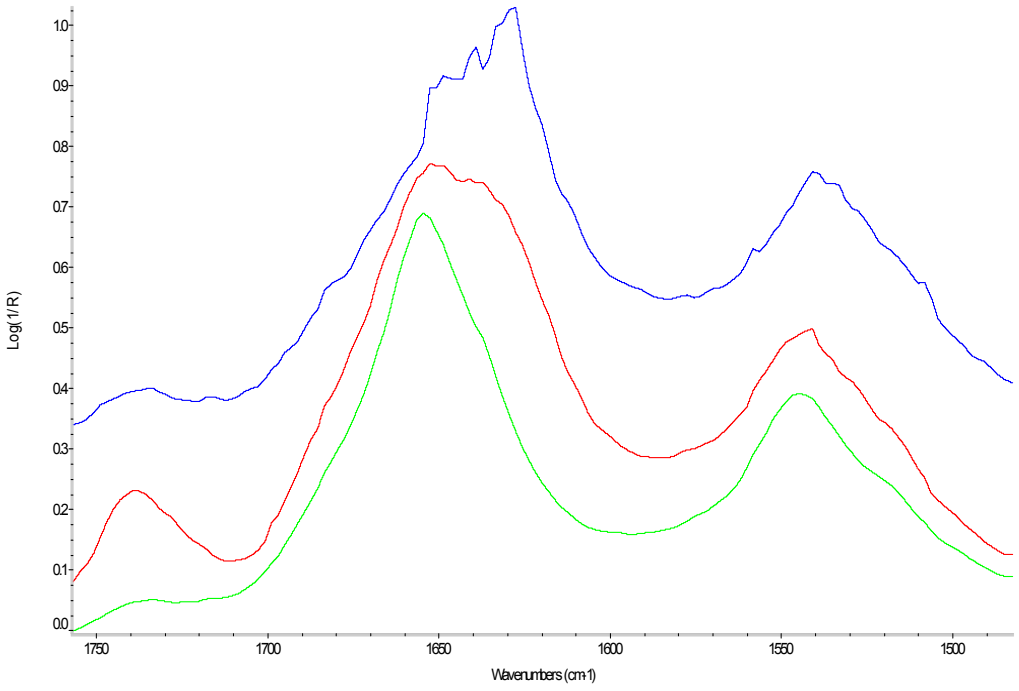

Figure 3.22: Amide I profiles resulting in positive β-sheet signal. The spectrum from a plaque core (red) produces a positive signal for β-sheet. In addition, spectra from some samples consistently produced false-positives for β-sheet. Examples of this are noisy spectra from dense tissue in A11 (blue) and slightly shifted spectra from A03 (green).

In addition, neurons and white matter produce infrared spectra with Amide I profiles with a slight shoulder and broader absorption, respectively (Figure 3.23). In both cases, this leads to false positives for β-sheet signal (Rak, 2007; Rak et al 2007). Individual spectra were examined for accuracy in β-sheet representation, but alternate processing parameters were not developed as this was not the focus of the project. As a result of these factors, processed maps and visual inspection of tissue samples were used in combination to determine that creatine deposits were not co-localized with plaques.

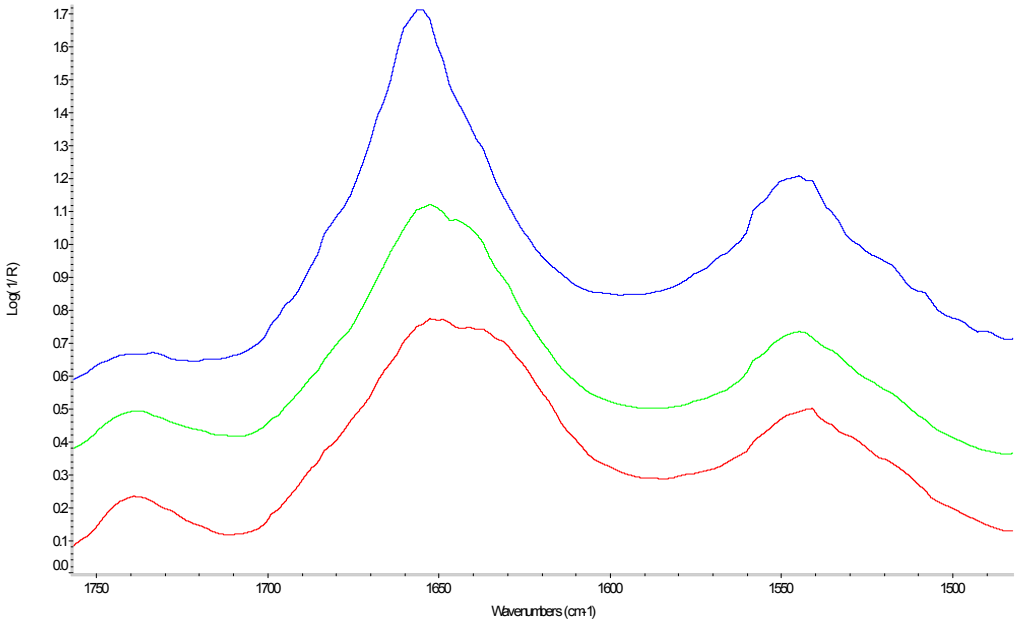

Figure 3.23: Amide I profiles from different regions of one hippocampus. Neuropil (Blue) produces a negative signal when pixels are processed for β-sheet content. Both the spectra of white matter (green) and plaque core (red) produce positive signals for β-sheet.

3.2 Depth profile of creatine in a Transgenic Mouse

Depth profiling, by analysis of serial sections, was undertaken in an effort to better characterize the creatine deposits and their distribution through the hippocampus of one mouse.

Serial sections were acquired from one TgCRND8 mouse, A14, and four of these were selected for analysis, based on the quality and proximity of the sections. Three of these were serial to one another, and the fourth section was separated by only one missing section.

Maps were acquired across the hippocampus of each section. These maps were acquired using the new Nicolet Continuum IR microscope at the Synchrotron Radiation Centre in Wisconsin. While similar areas were covered for these samples, the time required for data collection was reduced significantly from that required for previous samples – acquisition of maps to cover a full hippocampus took approximately one and a half days per sample. This reduction in time was possible because of improved signal/noise and a subsequent reduction in the number of spectra needed to be summed to obtain a useful result.

Maps were processed for creatine, plaque, and lipid levels. Dramatic changes in lipid levels are observed between regions containing grey and white matter, and this quality was used to ensure proper superposition of processed and tiled maps, allowing a comparison of the location of creatine deposits in each section (Figures 3.24-3.26).

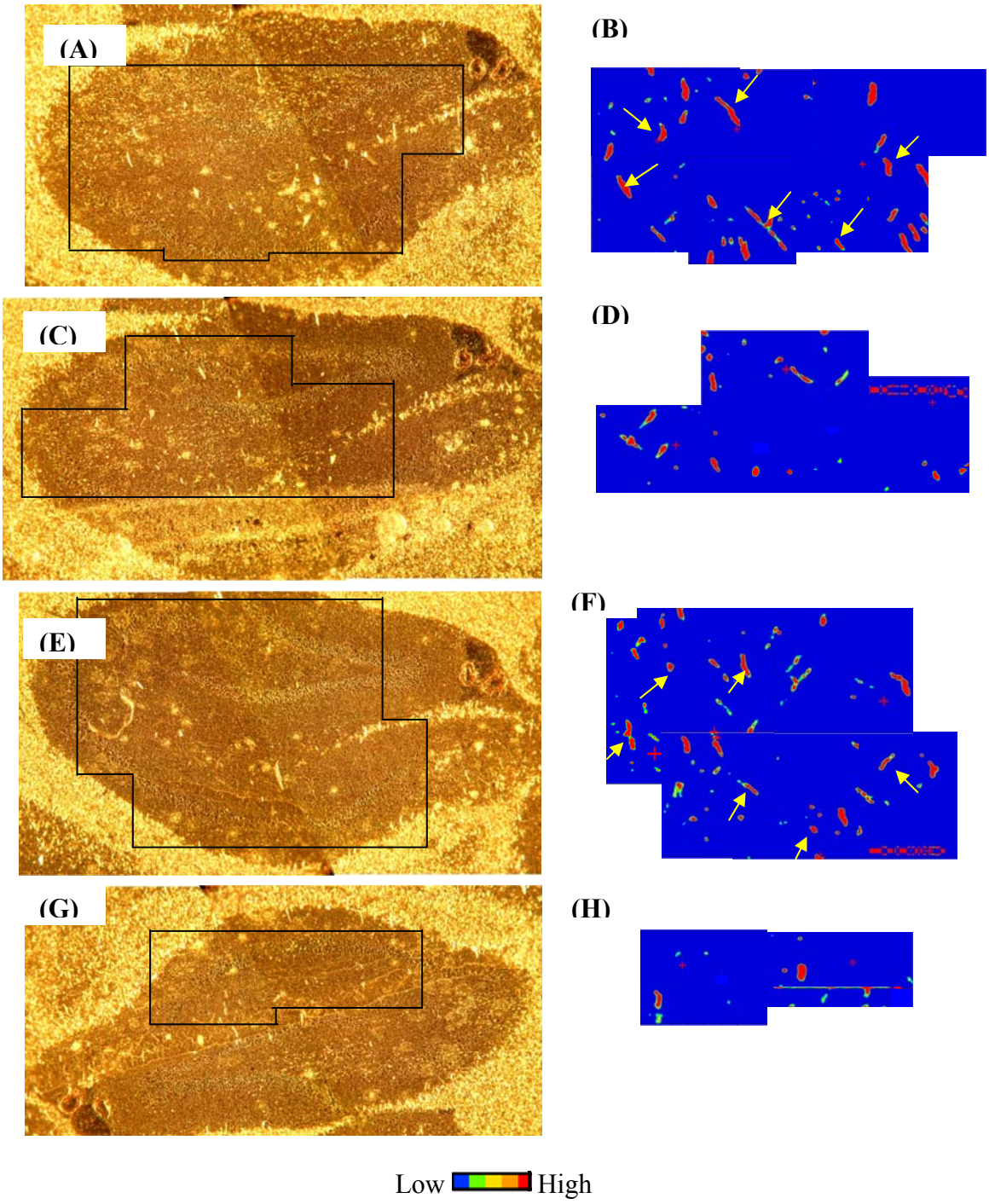

Figure 3.24: Creatine distribution in serial sections from the hippocampus of A14. The region of the hippocampus surveyed is outlined in images (A), (C), (E), (G). Creatine distribution is represented in the adjacent sections (B), (D), (F), (H). Sections A, C, and E are serial to one another, while one section was lost between E and G. Creatine deposits indicated with arrows occur in the same location in sections A and E.

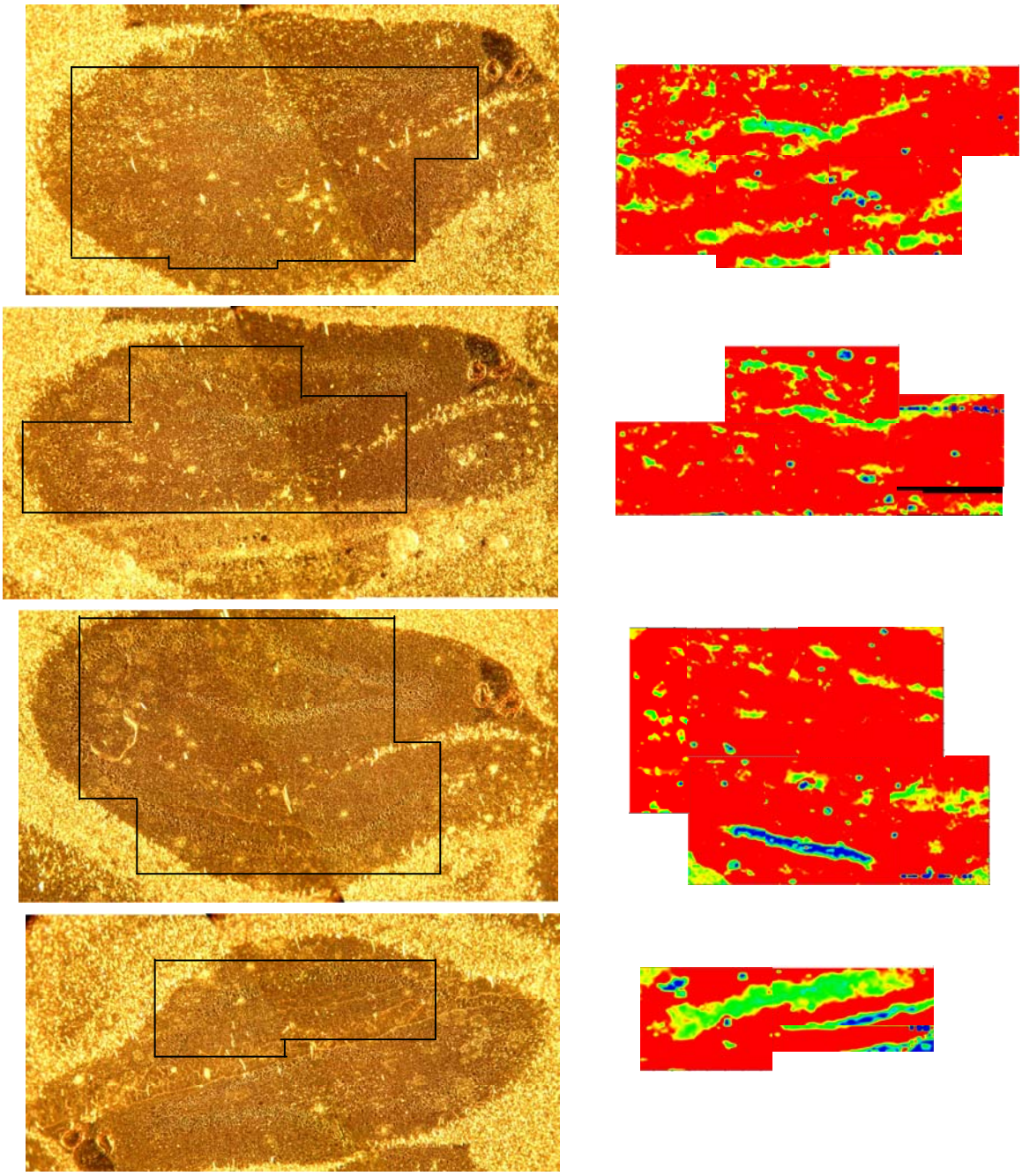

Figure 3.25: β-sheet distribution in serial sections from the hippocampus of A14. The region of the hippocampus surveyed is outlined in images (A), (C), (E), (G). β-sheet distribution is represented in the adjacent sections (B), (D), (F), (H). Sections A, C, and E are serial to one another, while one section was lost between E and G.

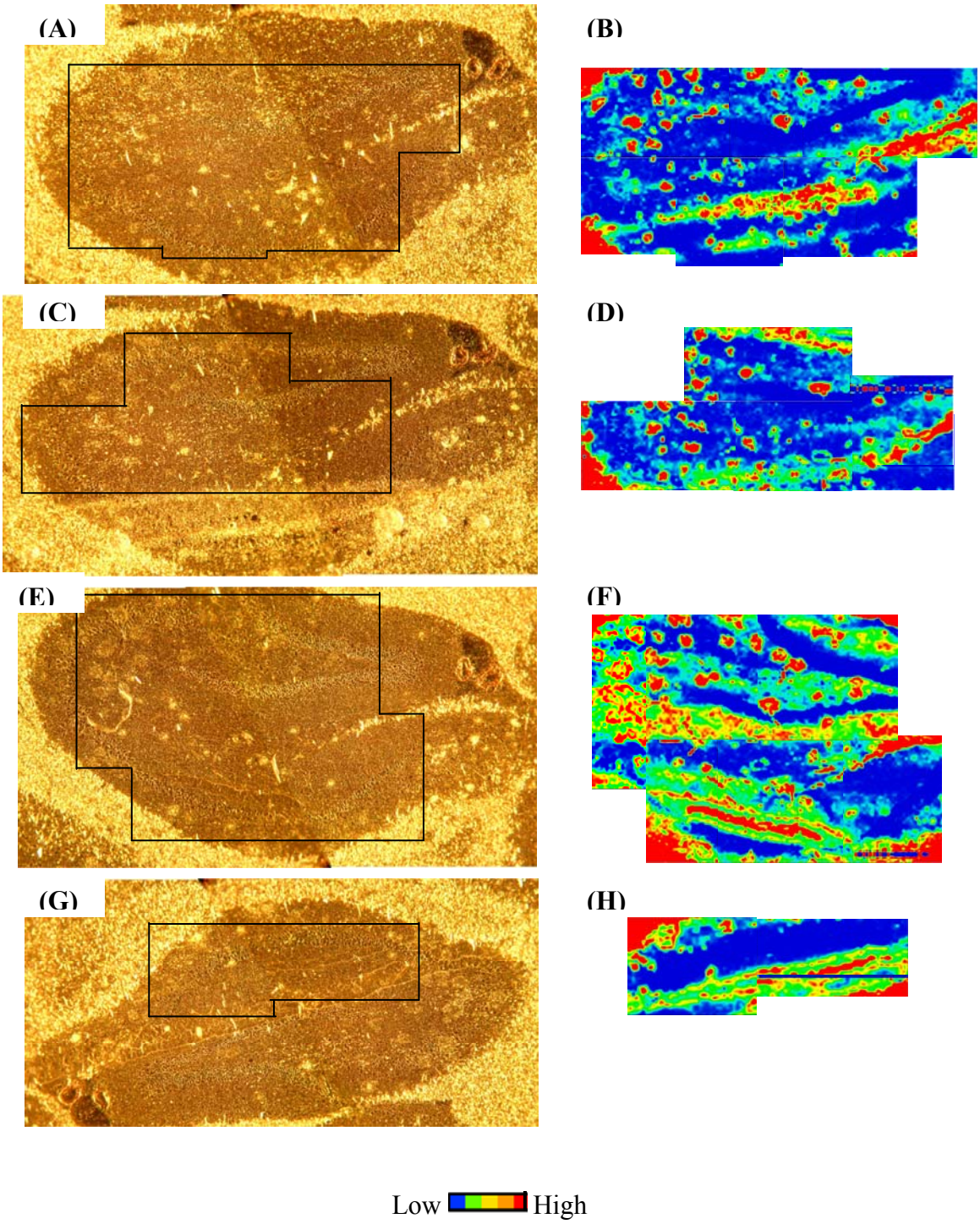

Figure 3.26: Lipid distribution in serial sections from the hippocampus of A14. The region of the hippocampus surveyed is outlined in images (A), (C), (E), (G). Lipid distribution is represented in the adjacent sections (B), (D), (F), (H). Sections A, C, and E are serial to one another, while one section was lost between E and G.

Several creatine deposits are apparent through the sections, and notable parallels are seen in the first and third section (Figures 3.24 (B) and (F)). The reduced association with the second and fourth section may be explained, in part, by distortion of the tissue at the time of sectioning. Some compression can be visually identified in images of the tissue (Figure 3.24 (G)).

As with previous maps, analysis for β-sheet revealed the distribution of plaques as well as neurons and white matter. Further, elevated lipid has been found surrounding dense-core plaques (Rak, 2007; Rak et al, 2007), allowing lipid maps to be compared with β-sheet maps for plaque location.

Processed, tiled maps were printed onto transparencies and serial maps were superimposed; features consistent through the samples were aligned. Maps processed for lipid provide a useful reference, due to the dramatic differences seen in grey and white matter. This superposition allowed for comparison of the location of creatine, plaques, and lipid in serial sections. As in the previous study, co-localization was not seen between plaques and creatine deposit

3.3 Detection of creatine is dependent on crystal orientation

Following submission of this thesis, further investigation of the samples by Veena Agrawal revealed that detection of creatine using the absorbance band at 1304 cm^{-1} is dependent on crystal orientation. As synchrotron radiation is linearly polarized, some vibrational modes will only be excited if the molecule is orientated correctly relative to the polarized light. Creatine molecules are all oriented the same way in each crystalline deposit and the 1304 cm^{-1} absorbance band is not observed for creatine crystals oriented horizontally (along the x-axis) on the tissue samples.

Figure 3.24 as reprocessed by Avid Khameneifer is presented in Appendix 1 and the impact on this finding on the results of this thesis is discussed.

4. Discussion

In this study, infrared microspectroscopy has permitted the identification and characterization of focally elevated deposits of creatine in the brains of AD mice, and has demonstrated that these deposits are not co-localized with other tissue components. Further, this technique has allowed tracking of these deposits through serial sections of tissue.

The ability to detect localized deposits of creatine, *in situ*, at micron level spatial resolution is a novel discovery and is specific to vibrational microspectroscopy of unfixed, snap-frozen cryosectioned sections.

The presence of an anomalous spectrum in tissue samples was noted during surveys of neurons in AD brain (Ogg, 2002) but the identity of the source remained unclear for several years until a library search by Paul Dumas identified creatine as a potential match. The systematic survey of levels of creatine in the brains of transgenic AD mice and their littermate controls followed the confirmation of the identity of creatine by IR and Raman spectroscopy (Gallant et al, 2006). Raman microspectroscopy can also be used to identify creatine deposits in tissue samples, but the 1 μm by 1 μm spot size of the laser source makes large area surveys cumbersome and time-consuming. Infrared microspectroscopy thus was our method of choice for the large-area surveys that were the focus of this research project.

Conventional histochemical analysis cannot be used for analysis of levels or distribution of creatine. Creatine is very soluble in water; the crystals seen in tissue samples would be rinsed away in the numerous solvent treatments required in staining protocols, and no stain has been developed for detection of creatine. Histochemical analysis permits the

identification of specific components within tissue samples, and the specificity of stains does not permit the detection of compounds other than those sought. For these reasons, detection of elevated creatine would not be possible through histochemical analysis. Other imaging techniques, such as MRI and PET, can detect creatine within the brain. However, these techniques do not offer the spatial resolution provided by infrared spectroscopy. Moreover, it is extremely difficult to achieve any quantitative comparison from subject to subject.

Despite this, there are limitations to infrared microspectroscopy: the identification of one specific molecule, such as creatine, within a matrix of tissue components is a rare finding, and possible only due to the localized elevated concentration of creatine in these deposits. Further, the sensitivity and accuracy of infrared microspectroscopy can be limited by the quality of data collected and the means of data processing employed.

In this section, the challenges in detection of creatine deposits are discussed, followed by a discussion of the focally elevated creatine deposits and their implication in the AD brain.

4.1 Data quality and processing

4.1.1 Poor Signal/Noise may prevent identification of creatine

Accurate analysis of creatine levels was dependent on the quality of the infrared spectra obtained. Although most of the data obtained was of excellent quality, poor focus of the microscope, loss of signal due to decay of the synchrotron radiation over time, or density of the tissue sample, particularly in regions with high plaque burden, led to reduced signal/noise in some maps. When signal/noise ratios decrease, the creatine peaks used for analysis are the first to be lost, or to have their absorbance profile modified by noise (Figure 4.1), as they are sharper and, in cases of low levels of creatine, less prominent than many tissue peaks,. While all pixels coloured to indicate the presence of creatine were reviewed to ensure a creatine signal was displayed, it is possible that creatine levels may be under-represented in maps where spectral quality was compromised.

This reduction in signal/noise ratios would have been particularly likely in maps acquired using the Nicolet Magna 500 FTIR Nic-Plan microscope as the stage that supported the sample was unsteady. During the time it took to acquire large maps, the microscope stage would droop, resulting in the sample moving out of the focal plane of the infrared radiation (Figure 4.2). Some maps were paused, re-focused, and resumed, or redone altogether, while others were partially discarded due to poor quality of data. No such loss of focus was seen with the Bruker Hyperion microscope, nor with the new Nicolet Continuum IR microscope (installed in fall 2006 at the Synchrotron Radiation Centre).

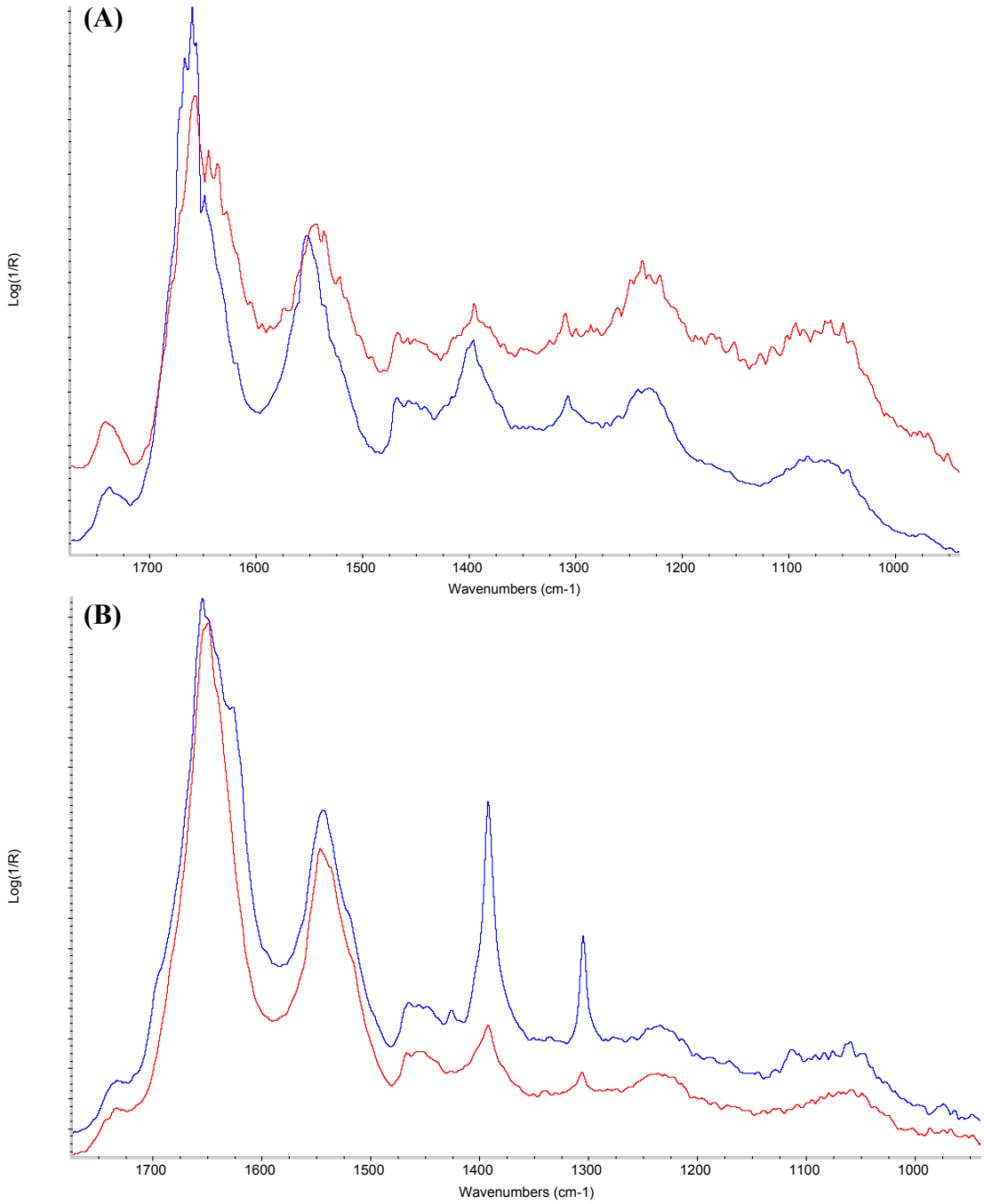

Figure 4.1: Effect of signal/noise on detection of creatine. In a sample with poor signal/noise ratios (A), the creatine signal may be easily lost within the noise if the signal is low (red). In an sample with better signal/noise ratios (B) there is a more pronounced difference between high (blue) and low (red) creatine levels.

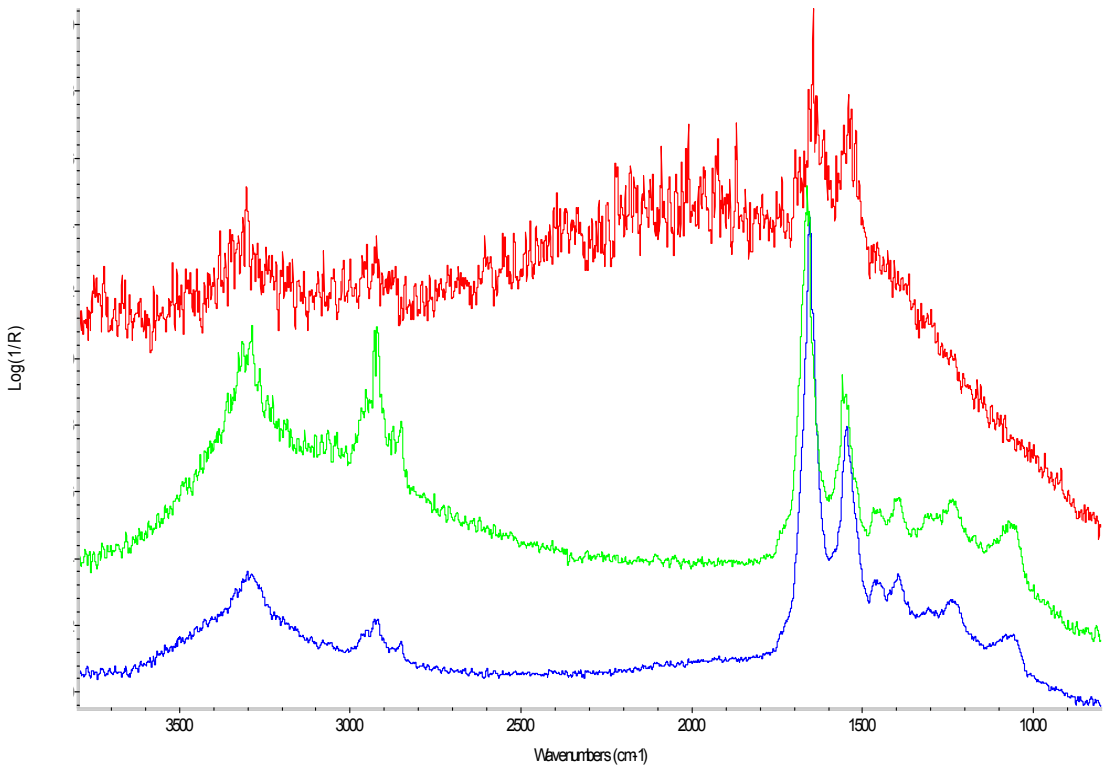

Figure 4.2: Effect of the loss of stage focus on spectral quality. Despite proper focus and good spectral quality in the early stages of a map (blue), the stage of the Nicolet Magna 500 FTIR Nic-Plan microscope would drop out of focus over time. While spectra acquired when the stage was only slightly out of focus may have been useful (green), by the end of some maps, spectra had become of low enough quality to be unusable (red). These three spectra were taken near the beginning (blue), middle (green) and end (red) of one infrared map, which was subsequently redone.

4.1.2 Changes in baseline necessitate changes in creatine processing parameters

The majority of creatine maps were processed using the primary set of parameters identified in the Chapter 2. However, for some samples, alternate parameters resulted in false colour images that were better representations of the distribution of creatine seen when examining individual spectra. Both samples that required these alternate parameters – A11 and A22 – displayed overall higher absorbance across the infrared spectrum. In many spectra, the absorbance from the amide I and amide II regions would saturate the detector, resulting in absorbance peaks that would plateau at the maximum allowed value of log(1/R) of 6. The need for alternate parameters reflects the higher overall absorbance of the sample as well as a slightly shifted baseline. Peak maxima appear at the same wavenumber for samples using both sets of parameters (Figure 4.2)

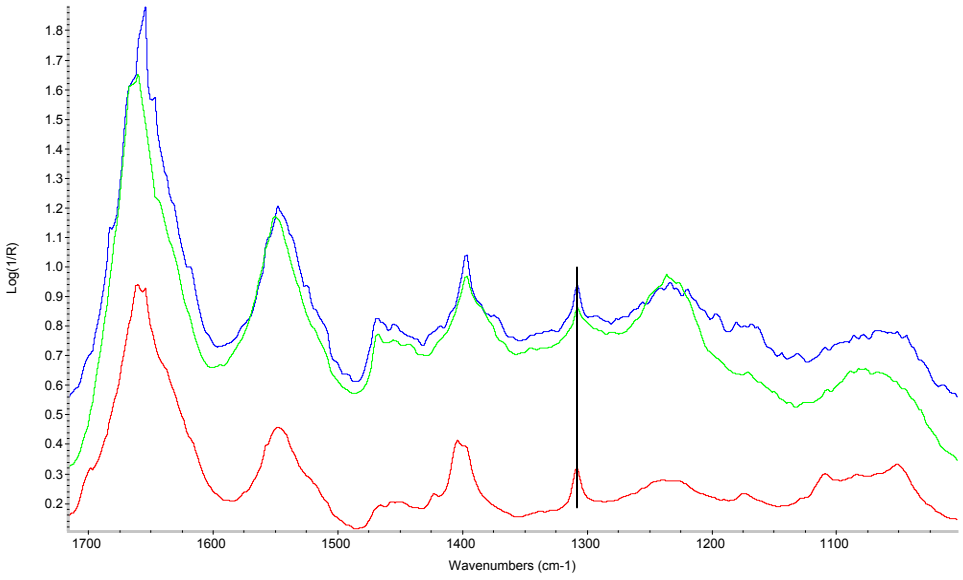

Figure 4.3: Creatine peak in samples using primary and alternate parameters. Spectra from samples A11 (green) and A22 (blue) display overall higher absorbance than those from other samples (red) and require alternate parameters to identify creatine levels accurately, despite the location of the peak maximum being at the same location for all samples. All three spectra are displayed on a common absorbance scale.

4.2 Focally elevated creatine

As reviewed in chapter 3, creatine has been found to be focally elevated in the brains of transgenic APP mice, as compared to their littermate controls. This can be seen through visual comparison of images depicting creatine distribution from littermate pairs in Figures 3.3-3.21, and is quantified in terms of the number of creatine pixels detected in each sample surveyed in Table 3.1.

This finding has remained consistent across two lines of transgenic mice; the TgCRND8 mice (Figures 3.3-3.13) show no discernable differences from the Tg19959 mice (Figures 3.14-3.17). This finding has also remained consistent with the use of two different types of infrared sources, with two differing spectrometers and differing parameters for data analysis. Samples A22-A25 were surveyed with both the Bruker Tensor FTIR with Bruker Hyperion microscope and globar lightsource, and with the Nicolet Magna 500 FTIR with Nic-Plan IR microscope and synchrotron light source (Figures 3.14-3.21). Use of both systems resulted in the detection of focally elevated creatine in the transgenic as compared to the control mice. Differences between the results obtained using the two systems are discussed below.

While the reliability of detection of plaques over large regions was limited, the results obtained from processing maps for β-sheet, combined with visual inspection of tissues for plaque locations, indicated that creatine deposits are not co-localized with plaques.

4.2.1 The hippocampus in the AD brain

The hippocampus is part of the medial temporal lobe memory system and is crucial to memory function (Squire and Zola-Morgan, 1991). The hippocampus is affected in the

early stages of AD, with the CA1 region being among the first to exhibit both Aβ plaques and NFT (Braak and Braak, 1991; Braak and Braak, 1996; Gertz et al, 1996). Levels of synapsin I – a protein associated with nerve terminals – have been found to be reduced in the AD hippocampus (Perdahl et al, 1984; Scheff and Price, 2003), and more recent ultrastructural studies have found synaptic loss, reduced width of the molecular layer, and an overall reduction in synaptic volume density (synapses per area) in the hippocampal dentate gyrus (Scheff and Price, 2003; Scheff et al, 2006). Volumetric MRI has been used to demonstrate that hippocampal volume is reduced in the earliest stages of AD (Fox and Freeborough, 1996; Convit et al, 1997; Jack et al, 1997; Laakso et al, 1998). MRI has also been used more recently to image the distribution of large plaques in the AD brain, both in vivo and in vitro (Faber et al, 2007).

4.2.2 Improved resolution of creatine deposits with synchrotron light source

Samples evaluated using the Bruker Tensor 27 FTIR with Bruker Hyperion microscope and Cytospec analysis gave the appearance of a larger creatine presence. This is a result of the larger pixel size necessary using this globar source. With a 25 μm by 25 μm pixel size, any creatine within this pixel area would result in a positive signal for creatine, regardless of the actual size of the deposit. Thus a small creatine deposit could result in the assignment of a full positive pixel. This demonstrates the improved accuracy of analysis with the diffraction-limited spatial resolution of a synchrotron light source. Despite this, it is important to note that for those samples observed with both synchrotron and globar sources (A22-A25), creatine deposits were identified in the same regions

using both instruments, with the difference in results being due to the spatial resolution of the instrument.

4.2.3 Creatine deposits are found frequently in the CA region

The distribution of the creatine deposits revealed in the initial surveys of transgenic mice and their non-transgenic littermates was further explored by the analysis of serial sections of one mouse, A14. This further revealed that a majority of the deposits observed were located in the CA1 region of the hippocampus. Many of these deposits were linear, or streak-like, in shape suggesting that they may be transported through a linear component of the brain, such as axons or capillaries. Further studies of creatine deposits in serial section could confirm whether some small deposits are part of linear deposits moving perpendicular to the plane of the section.

The localization of creatine deposits within the CA may mean that creatine levels are under-reported in samples where the full CA was not surveyed.

4.2.4 Transgenic and non-transgenic mice display creatine deposits

Three of the eight non-transgenic mice displayed creatine deposits. These mice, A02, A04, and A10 were three of the eldest mice, aged 624, 504, and 457 days respectively, at the time of sacrifice. While fewer deposits were present in these mice than in their counterparts with AD, the deposits are still significant, suggesting that the pooling of creatine may be due to processes common to both AD and aging.

In only one pair of mice – A10 and A11 – creatine levels were higher in the control as compared to the transgenic mouse. Infrared spectra acquired from the AD mouse, A11,

were very noisy which may have resulted in under-reporting of creatine levels in this sample. In addition, neither sample had the full hippocampus mapped (Figures 3.8 and 3.9), and full mapping of the region may alter the relative amounts of creatine.

4.3 Limitations to imaging creatine deposits through serial sections

Of four serial sections analyzed for creatine levels, the first and third sections displayed the best congruency between creatine deposits, with six identifiable in both sections. These deposits could not be associated with deposits in the second or fourth sections, and these did not reveal deposits that were congruent between themselves.

Despite these four sections being selected based on the quality of the samples, both the second and fourth sections show folding that would have occurred on sectioning. This suggests that even moderate compression of the sample may distort the creatine distribution detected.

Maps processed for both lipid and β-sheet content displayed better congruency between serial sections, with all larger features, such as white matter and neurons, aligning and a few smaller features, such as those that may represent plaque locations, aligning. In these maps, congruency was best between the first and third sample as well.

4.4 Previous MRS evaluation of metabolites in the AD brain

Several earlier magnetic resonance spectroscopy (MRS) studies have examined metabolite concentration in the AD brain (Pfefferbaum et al 1999; Stoppe et al, 2000; Huang et al, 2001; Valenzuela et al, 2001; Ackl et al, 2005; Godbolt et al, 2006; Mandal,

2007). The hippocampus is rarely a specific target, due to its small size, but creatine levels are often a factor in these studies.

Several studies have used total creatine levels – the combined creatine and phosphocreatine signal – as internal controls when levels of other metabolites are sought, sometimes as a sole reference and othertimes alongside a second internal standard (Valenzuela et al, 2001; Ackl et al, 2005; Godbolt et al, 2006). This is due, at least in part, to the stability of creatine within an individual over time. While the focally elevated creatine levels detected in the hippocampus of transgenic mice may or may not be consistent across the full brain, the use of creatine as an internal control should be reconsidered.

Other studies aimed at investigating possible variation in creatine concentration in the AD brain have produced varying results – some show no significant difference in creatine levels in AD patients as compared to controls (Stoppe et at, 2000), while others note higher creatine levels in AD patients (Huang et al, 2001), and still others report elevated creatine and phosphocreatine levels in both AD and elderly control patients (Pfefferbaum et al, 1999). While the results of this study support those that show elevated levels of creatine in AD patients, and the presence of creatine deposits in elderly controls, more extensive surveying is necessary to confirm whether the finding is consistent across other regions of the brain. Should further surveys find that the elevation of creatine levels is isolated to the hippocampus, it is likely that MRS would not detect this change. Should further surveys find that creatine is elevated throughout the brain, this would suggest that MRS may not have the resolution necessary to detect the small creatine deposits.

4.5 Causes of elevated creatine remain unclear

This study does not reveal the cause of elevated creatine, but some speculation is necessary to determine future directions of research.

Inflammation and oxidative stress are common to both AD and aging, and these conditions are known to modify metabolic processes and numerous enzymes, including creatine kinase (David et al, 1998; Castegna et al, 2002; Aksenov et al, 2000). This potential disruption to the CK reaction could lead to pooling of creatine as depleted PCr reserves are replaced by transport of additional PCr, rather than by rephosphorylation of Cr by CK. Enzymes or precursors in Cr synthesis may also be modified in AD, affecting the balance of Cr in the body.

Creatine concentration is higher in astrocytes and oligodendrocytes than in neurons (Urenjak et al, 1993) and astrocytes respond to neuronal injury in both the AD and aged brain (Cotrina and Nedergaared, 2002; Miller and O'Callaghan, 2003), with presence of astrocytes increasing by an estimated 20% in normal aging (Cotrina and Nedergaared, 2002). While neuronal loss in AD is accepted fact, neuronal loss in normal aging remains under discussion (McEwen, 1999; Šimić et al, 1997). However, elevated creatine levels as a result of increased astrocytes would explain elevated creatine in both AD and aged mice.

4.6 Nature of creatine localization

The creatine deposits observed had varying shapes – some appeared as large aggregates while others appeared linear, or streak-like. Examples of both types of deposit can be seen in the processed maps of the hippocampus of A03 (Figure 3.5).

Creatine deposits appearing as large aggregates could indicate the transport of localized creatine through cells such as astrocytes. These aggregates could also indicate that creatine is ubiquitous throughout the hippocampus, with the aggregation being a result of crystallization either in vivo, or after the animal is sacrificed and the tissue harvested. Linear deposits suggest that creatine is contained within linear structures in the brain, such as axons or capillaries. The prevalence of the deposits in the CA1 region would support the presence of creatine in neurons over capillaries.

However, both types of deposits are found in the hippocampi surveyed, suggesting either that multiple processes lead to focally elevated creatine or that a link exists between the two types. As mentioned earlier, deposits that do not have a linear appearance could be the result of a structure moving perpendicular to the plane of the samples cut. Further, any structure containing creatine in close proximity to another structure doing the same could appear as one large aggregate, as could any curling or coiling of one structure.

If creatine deposits are contained within axons, it is possible that the loss of a neuron containing creatine could result in a linear deposit becoming a larger aggregate. The shift from linear, axon-contained deposits to less constrained deposits would be seen more commonly in aged mice for whom the disease had progressed further.

5. Conclusions and Future Work

From this preliminary assessment of creatine in the AD brain, it can be concluded that:

- Infrared microspectroscopy can detect elevated creatine in situ, with spatial resolution improving with synchrotron light sources. While this technique is limited in its scope, it provides information unavailable through conventional histochemical and other imaging technique and is an important complement to research ongoing in these fields.

- Creatine is focally elevated in the brains of transgenic AD mice as compared to non-transgenic littermates.

- Current MRS studies using creatine as an internal control may be inaccurate; the practice of using total creatine levels as an internal control should be reviewed.

- Creatine is not co-localized with plaques.

- Creatine can be detected in serial sections from one mouse, providing information on the nature of creatine deposits that will lead to further understanding of the reason and role of elevated creatine in the AD brain.

- Creatine is seen in the brains of non-transgenic elderly mice.

Further research is necessary to explore the significance of the localization of deposits, to confirm their shape or structure, and to explore the significance of elevated creatine in the AD and aged brain. Specifically:

- Further mapping of large regions in serial sections from one mouse will provide for a better understanding of the shape of creatine deposits within the brain, allowing for a better understanding of why creatine is elevated in the AD brain.

- Similar large-region mapping in regions of the brain other than the hippocampus will indicate whether elevated creatine is specific to the hippocampus or is a common feature throughout the AD brain.

- Staining for enzymes involved in the synthesis of creatine (AGAT and GAMT) and its processing in brain (CK) will reveal whether an increase or decrease in these enzymes is a factor in the increased creatine levels observed.

- Reprocessing for creatine using parameters for peaks other than the 1304 cm^{-1} absorbance band will provide a more accurate depiction of creatine in the samples, eliminating the impact of crystal orientation.

Appendix 1

Initially, the 1304 cm^{-1} peak was chosen for analysis of creatine levels as it was isolated from typical absorbance features in infrared spectra of tissue samples. The peaks between 1408 and 1384 cm^{-1} provide a stronger signal, but overlay other absorbance bands. However, by 2007, improvements in data acquisition at the Synchrotron Radiation Centre improved signal to noise ratios, and further data acquisition and analysis revealed that the doublet around 1400 cm^{-1} and the peak at 1304 cm^{-1} are orientation dependent, with the peak at 1304 cm^{-1} being inactive in some orientations, and the two peaks within the doublet around 1400 cm^{-1} having opposing responses to orientation. Thus one of the two peaks within the doublet remains active in every orientation.

As mentioned in section 3.3, analysis of creatine deposits using the 1304 cm^{-1} absorbance band under-represents the levels of creatine in the brain as the vibrational mode associated with the 1304 cm^{-1} band is only activated when creatine crystals are oriented correctly relative to linearly polarized synchrotron radiation. Figure 3.24 was re-analyzed (Figure A.1) using the absorbance between 1408 and 1384 cm^{-1} with a baseline set between 1412 and 1380 cm^{-1}.

Clearly, the levels of creatine described in this thesis are not an accurate reflection of the levels present in the samples examined. The data presented in part B of Figures 3.3 to 3.17 and the number of pixels of creatine counted in Table 3.1 are under-representations and should be re-evaluated. Data acquired using a globar light source (Figures 3.18 to 3.21) will not be affected by this finding, as globar radiation is not polarized.

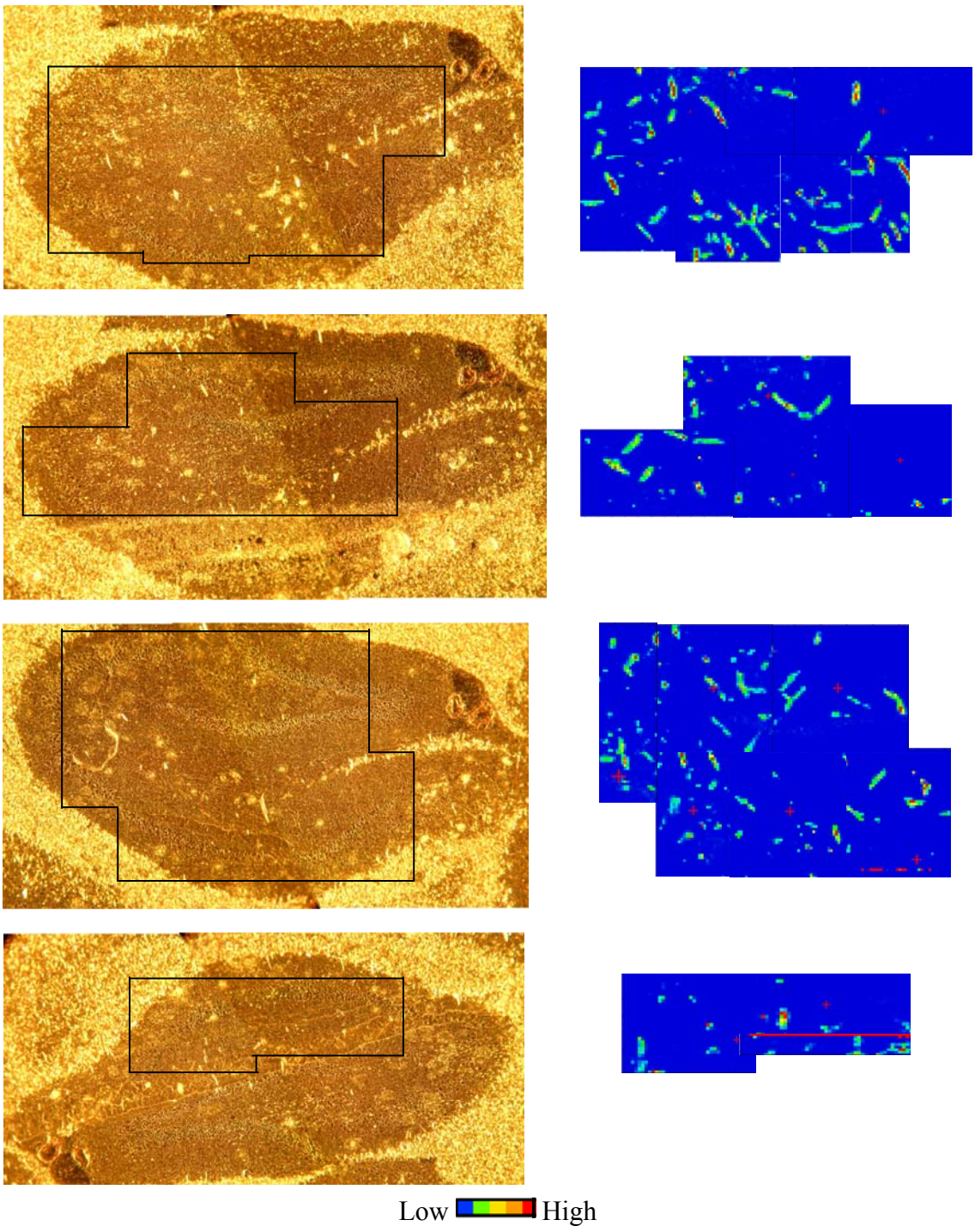

Figure A.1: Creatine distribution in serial sections from the hippocampus of A14, reprocessed. As in Figure 3.24, the region of the hippocampus surveyed is outlined in images (A), (C), (E), (G). Creatine distribution is represented in the adjacent sections (B), (D), (F), (H). These sections have been analyzed using the peaks between 1408 and 1384 cm^{-1}, rather than the peak centered at 1304 cm^{-1}. Several horizontal deposits can be seen that were not represented in Figure 3.24.

References

Ackl, N., Ising, M., Schreiber, Y. A., Atiya, M., Sontag, A., Auer, D. P. (2005) Hippocampal metabolic abnormalities in mid cognitive impairment and Alzheimer's disease. Neurosci Lett, 384, 23-28.

Aksenov, M., Aksenova, M., Butterfield, D. A., Markesbery, W. R. (2000) Oxidative modification of creatine kinase BB in Alzheimer's disease brain. J Neurochem, 74, 2520-2527.

Bhatia, R., Lin, H., Lal, R. (2000) Fresh and globular amyloid β protein (1-42) induces rapid cellular degeneration: evidence for AβP channel-mediated cellular toxicity. FASEB Journal, 14, 1233-1243.

Blessed, G., Tomlinson, B. E., and Roth, M. (1968) The Association Between Quantitative Measures of Dementia and of Senile Change in the Cerebral Grey Matter of Elderly Subjects. Brit J Psychiat, 114, 797-811.

Braak, H., and Braak, E. (1991) Neuropathological stageing of Alzheimer-related changes. Acta Neuropathol, 82, 239-259.

Braak, H., and Braak, E. (1996) Evolutio of the neuropathology of Alzheimer's disease. Acta Neurol Scand, 165, 3-12.

Braissant, O., Henry, H., Loup, M., Eilers, B., Bachmann, C. (2001) Endogenous synthesis and transport of creatine in the rat brain: an in situ hybridization study. Mol Brain Res, 86, 193-201.

Buée, L., Bussière, T., Buée-Scherrer, V., Delacourte, A., Hof, P. R. (2000) Tau protein isoforms, phosphorylation and role in neurodegenerative disorders. Brain res rev, 33, 95-130.

Buée-Scherrer, V., Buée, L., Hof, P. R., Leveugle, B., Gilles, C., Loerzel, A. J., Perl, D. P., Delacourte, A. (1995) Neurofibrillary degeneration in Amyotrophic Lateral Sclerosis/Parkinsonism-Dementia Complex of Guam. Am J Path, 68, 924-932.

Buée-Scherrer, V., Buée, L., Leveugle, B., Perl, D. P., Vermersch, P., Perl, Hof, P. R., Delacourte, A. (1997) Pathological τ proteins in postencephalitic Parkinsonism: Coparison with Alzheimer's disease and other neurodegenerative disorders. Annals of Neurology, 42, 356-359.

Buée-Scherrer, V., Hof, P. R., Buée, L., Leveugle, B., Vermersch, P., Perl, D. P., Olanow, C. W., Delacourte, A. (1996) Hyperphosphorylated tau proteins differentiate corticobasal degeneration and Pick's disease. Acta Neuropathol, 91, 351-359.

Busciglio, J., Gabuzda, D. H., Matsudaira, P., Yankner, B. A. (1993) Generation of β-amloid in the secretory pathway in neuronal and neuronal cells. Proc Natl Acad Sci USA, 90, 2092-2096.

Butterfield, D. A., Griffin, S., Munch G., Pasinetti, G. M. Amyloid β-peptide and amyloid pathology are central to the oxidative stress and inflammatory cascades under which Alzheimer's disease brain exists. Journal of Alzheimer's Disease, 4, 193-201.

Cadoux-Hudson, T. A., Blackledge, M. J., Radda, G. K. (1989) Imaging of human brain creatine kinase activity in vivo. FASEB, 3, 2660-2666.

Camacho, N. P., West, P., Torzilli, P. A., Mendelsohn, R. (2001) Biopolymers, 62, 1-8.

Canadian Study of Health and Aging Working Group. (1994) Canadian Study of Health and Aging: study methods and prevalence of dementia. Can Med Assoc J, 150, 899-913.

Canadan Study of Health and Aging Working Group. (2000) The Incidence of dementia in Canada. Neurology, 55, 66-73.

Carr, G. L. (2001) Resolution limits for infrared microspectroscopy explored with synchrotron radiation. Rev Sci Instrum, 72, 1613-1619.

Carr, G. L., Hanfland, M., Williams, G. P. (1995) Midinfrared beamline at the National Synchrotron Light Source port U2B. Rev Sci Instrum, 66, 1643-1645.

Casley, C. S., Canevari, L., Land, J. M., Clark, J. B., Sharpe, M. A. (2002) β-Amyloid inhibits integrated mitochondrial respiration and key enzyme activities. J Neurochem, 80, 91-100.

Castegna, A., Aksenov, M., Aksenova, M., Thongboonkerd, V., Klein, J. B., Pierce, W. M., Booze, R., Markesbery, W. R., Butterfield, D. A. (2002) Proteomic identification of oxidatively modified proteins in Alzheimer's disease brain. Part I: creatine kinase BB, glutamine synthase, and ubiquitin carboxy-terminal hydrolase L-1. Free Radical Biology & Medicine, 33, 562-571.

Chartier-Harlin, M., Crawford, F., Houlden, H., Warren, A., Hughes, D., Fidani, L., Goate, A., Rossor, M., Roques, P., Hardy, J., Mullan, M. (1991) Early-onset Alzheimer's disease caused by mutations at codon 717 of the β-amyloid precursor protein gene. Nature, 353, 844-846.

Chisti, M. A., Yang, D., Janus, C., Phinney, A. L., Horne, P., Pearson, J., Strome, R., Zuker, N., Loukides, J., French, J., Turner, S., Lozza, G., Grilli, M., Kunicki, S., Morissette, C., Paquette, J., Gervais, F., Bergeron, C., Fraser, P. E., Carlson, G. A., St. George-Hyslop, P., Westaway, D. (2001) Early-onset amyloid deposition and cognitive deficits in transgenic mice expressing a double mutant form of amyloid precursor protein 695. J Biol Chem, 276, 21562-21570.

Choo, L., Wetzel, D. L., Halliday, W. C., Jackson, M., LeVine, S. M., Mantsch, H. H. (1996) In Situ characterization of β-amyloid in Alzheimer's diseased tissue by synchrotron Fourier Transform infrared microspectroscopy. Biophysical Journal, 71, 1672-1679.

Convit, A., De Leon, M. J., Tarshish, C., De Santi, S., Tsui, W., Rusinek, H., George, A. (1997) Specific hippocampal volume reductions in individuals at risk for Alzheimer's disease. Neurobiol Aging, 18, 131-138.

Corder, E. H., Saunders, A. M., Strittmatter, W. J., Schmechel, D. E., Gaskell, P. C., Small, G. W., Roses, A. D., Haines, J. L., Pericak-Vance, M. A. (1993) Gene dose of apolipoprotein E type 4 allele and the risk of Alzheimer's disease in late onset families. Science, 261, 921-923.

Cotrina, M. L., Nedergaard, M. (2002) Astrocytes in the aging brain. J Neurosci Res, 67, 1-10.

Cummings, J. L., Cole, G. (2002) Alzheimer's disease. JAMA, 287, 2335-2338.

Cytospec, Inc. http://www.cytospec.com. Croton-On-Hudson, NY, USA.

David, S., Shoemaker, M., Haley, B. E. (1998) Abnormal properties of creatine kinase in Alzheimer's disease brain: Correlation of reduced enzyme activity and active site photolabeling with aberrant cytosol-membrane partitioning. Mol Brain Res, 54, 276-287.

Delacourte, A., David, J. P., Sergeant, N., Buée, L., Wattez, A., Vermersch, P., Ghozali, F., Fallet-Biance, C., Pasquier, F., Lebert, F., Petit, H., Di Menza, C. (1999) The biochemical pathway of neurofibrillary degeneration in aging and Alzheimer's diseases. American Academy of Neurology, 52, 1158-1165.

Delacourte, A., Sergeant, N., Wattez, A., Gauvreau, D., Robitaille, Y. (1998) Vulnerable neuronal subsets in Alzheimer's and Pick's disease are distinguished by their τ isoform distribution and phosphorylation. Annals of neurology, 198, 193-204.

Dickson, D. W. (1997) The pathogenesis of senile plaques. J Neuropathol Exp Neurol, 56, 321-339.

Dringen, R., Verleysdonk, S., Hamprecht, B., Willker, W., Leibfritz, D., Brand, A. (1998) Metabolism of glycine in primary astroglial cells: synthesis of creatine, serine, and glutathione. J Neurochem, 70, 835-840.

Dumas, P., and Miller, L. (2003) Biological and biomedical applications of synchrotron infrared microspectroscopy. J Biol Phys, 29, 201-218.

Dumas, P., and Miller, L. (2003) The use of synchrotron infrared microspectroscopy in biological and biomedical investigations. Vib Spec, 32, 3-21.

Dumas, P., Sockalingum, G. D., Sulé-Suso, J. (2007) Adding synchrotron radiation to infrared microspectroscopy: what's new in biomedical applications? Trends in Biotechnology, published online.

Duncan, W. D., and Williams, G. P. (1983) Infrared synchrotron radiation from electron storage rings. Applied Optics, 22, 2914-2923.

Esch, F. S., Keim, P. S., Beattie, E. C., Blacher, R. W., Culwell, A. R., Oltersdorf, T., McClure, D., Ward, P. J. (1990) Cleavage of amyloid β peptide during constitutive processing of its precursor. Science, 248, 1122-1124.

Faber, C., Zahneisen, B., Tippmann, F., Schroeder, A., Fahrenholz, F. (2007) Gradient-echo and CRAZED imaging for minute detection of Alzheimer plaques in an APP_{V717I} x ADAM10-*dn* mouse model. Magnetic Resonance in Medicine, 57, 696-703.

Fox, N. C., Freeborough, P. A. (1996) Visualisatio and quantification of rates of atrophy in Alzheimer's disease. Lancet, 348, 94-98.

Fraser, R. D. B. (1950) Infra-red microspectrometry with a 0.8 N.A. reflecting microscope. Discuss Faraday Soc, 9, 378-383.

Gallant, M., Rak, M., Szeghalmi, A., Del Bigio, M. R., Westaway, D., Yang, J., Julian, R., Gough, K. M (2006) Focally elevated creatine detected in amyloid precursor protein (APP) transgenic mice and Alzheimer disease brain tissue. J Biol Chem, 281, 5-8.

Geddes, J. F., Hughes, A. J., Lees, A. J., and Daniel, S. E. (1993) Pathological overlap in cases of parkinsonism associated with neurofibrillary tangles. Brain, 116, 281-302.

Gertz, H.-J., Xuereb, J. H., Huppert, F. A., Brayne, C., Krüger, H., McGee, M. A., Paykel, E. S., Harrington, C. R., Mukaetova-Ladinska, E. B., O'Conner, D. W., Wischik, C. M. (1996) The relationship between clinical dementia and neuropathological staging (Braak) in a very elderly community sample. Eur Arch Psychiatry Clin Neurosci, 246, 132-136.

Gibson, G. E. (2002) Interactions of oxidative stress with cellular calcium dynamics and glucose metabolism in Alzheimer's disease. Free Radical Biology & Medicine, 32, 1061-1070.

Glenner, G. G., and Wong, C. W. (1984) Alzheimer's disease: initial report of the purification and characterization of a novel cerebrovascular amyloid protein. Biochem Biophys Res Commun, 120, 885-890.

Goate, A., Chartier-Harlin, M., Mullan, M., Brown, J., Crawford, F., Fidani, L., Giuffra, L., Haynes, A., Irving, N., James, L., Mant, R., Newton, P., Rooke, K., Roques, P., Talbot, C., Pericak-Vance, M., Roses, A., Williamson, R., Rossor, M., Owen, M., Hardy, J. (1991) Segregation of a missense mutation in the amyloid precursor protein gene with familial Alzheimer's disease. Nature, 349, 704-706.

Godbolt, A. K., Waldman, A. D., MacManus, D. G., Schott, J. M., Frost, C., Cipolotti, L., Fox, N. C., Rossor, M. N. (2006) MRS shows abnormalities before symptoms in familial Alzheimer disease. Neurology, 66, 718-722.

Gough, K. M., Zelinski, D., Wiens, R., Rak, M., Dixon, I. M. C. (2003) Fourier transform infrared evaluation of microscopic scarring in the cardiomyopathic heart: Effect of chronic AT_1 suppression. Anal Biochem, 316, 232-242.

Gowing, E., Roher, A. E., Woods, A. S., Cotter, R. J., Chaney, M., Little, S. P., Ball, M. J. (1994) Chemical characterization of Aβ 17-42 peptide, a component of diffuse amyloid deposits of Alzheimer disease. J Biol Chem, 269, 10987-10990.

Griffiths, P. R., Sloane, H. J., Hannah, R. W. (1977) Interferometers vs. monochromators: Separating the optical and digital advantages. Appl Spectrosc, 31, 485-495.

Grundke-Iqbal, I., Iqbal, K., Quinlan, M., Tung, Y., Zaidi, M. S., and Wisniewski, H. M. (1986) Microtubule-associated Protein Tau: a component of Alzheimer paired helical filaments. J Biol Chem, 261, 6084-6089.

Grundke-Iqbal, I., Iqbal, K., Tung, Y., Quinlan, M., Wisniewski, H. M., and Binder, L. I. (1986) Abnormal Phosphorylation of the Microtubule-Associated Protein tau (Tau) in Alzheimer Cytoskeletal Pathology. Proc Natl Acad Sci USA, 83, 4913-4917.

Haas, C., Hung, A. Y., Selkoe, D. J. (1991) Processing of β-amyloid precursor protein in microglia and astrocytes favors an internal localization over constitutive secretion. J Neurosci, 11, 3783-3793.

Haass, C., Hung, A. Y., Schlossmacher, M. G., Teplow, D. B., Selkoe, D. J. (1993) β-Amyloid peptide and a 3-kDa fragment are derived by distinct cellular mechanisms. J Biol Chem, 268, 3021-3024.

Haass, C., Schlossmacher, M. G., Hung, A. Y., Vigo-Pelfrey, C., Mellon, A., Ostaszewski, B. L., Lieberburg, I., Koo, E. H., Schenk, D., Teplow, D. B., Selkoe, D. J. (1992) Amyloid β-peptide is produced by ultured cells during normal metabolism. Nature, 359, 322-325.

Hansen, L. A., Masliah, E., Galasko, D., and Terry, R. D. (1993) Plaque-only Alzheimer disease is usually the Lewy Body variant, and vice versa. J Neuropathol Exp Neurol, 52, 648-654.

Harigaya, Y., Shoji, M., Kawarabayashi, T., Kanai, M., Nakamura, T., Iizuka, T., Igeta Y., Saido, T. C., Sahara, N., Mori, H., Hirai, S. (1995) Modified amyloid β protein ending at 42 or 40 with different solubility accumulates in the brain of Alzheimer's disease. Biochem Biophys Res Commun, 211, 1015-1022.

Heneka, M. T. (2006) Inflammation in Alzheimer's disease. Clinical Neuroscience Research, 6, 247-260.

Herzberg, G. (1939) Molecular Spectra and Molecular Structure: Diatomic Molecules. Prentice-Hall: New York.

Herzberg, G. (1945) Molecular Spectra and Molecular Structure: Infrared and Raman Spectra of Polyatomic Molecules. Van Nostrand: Princeton.

Hirano, A., Malamud, N., Elizan, T. S., and Kurland, L. T. (1966) Amyotrophic Lateral Sclerosis and Parkinsonism-Dementia Complex on Guam. Arch Neurol, 15, 35-51.

Hof, P. R., Bouras, C., Perl, D. P., Sparkes, D. L., and Morrison, J. H. (1995) Age-related distribution of neuropathologic changes in the cerebral cortex of patients with Down's syndrome. Arch neurol, 52, 379-391.

Hof, P. R., Charpiot, A., Delacourte, A., Buée, L., Purohit, D., Perl, D. P., and Bouras, C. (1992) Distribution of neurofibrillary tangles and senile plaques in the cerebral cortex in postencephalitic parkinsonism. Neuroscience Letters, 139, 10-14.

Hsia, A. Y., Masliah, E., McConlogue, L., Yu, G., Tatsuno, G., Hu, K., Kholodenko, D., Malenka, R. C., Nicoll, R. A., Mucke, L. (1999) Plaque-independent disruption of neural circuits in Alzheimer's disease mouse models. Proc Natl Acad Sci USA, 96, 3228-3233.

Huang, W., Alexander, G. E., Chang, L., Shetty, H. U., Krasucki, J. S., Rapoport, S. I., Schapiro, M. B. (2001) Brain metabolite concentration and dementia severity in Alzheimers disease. Neurology, 57, 626-632.

Huffman, S. W., Bhargava, R., Levin, I. W. (2002) Generalized implementation of rapid-scan Fourier Transform infrared spectroscopic imaging. Applied Spectroscopy, 56, 965-969.

Hyman, B. T., Trojanowski, J. Q. (1997) Editorial on Consensus Recommendations for the Postmortem Diagnosis of Alzheimer Disease from the National Institute on Aging and the Reagan Institute Working Group on Diagnostic Criteria for the Neuropathological Assessment of Alzheimer Disease. J Neuropathol Exp Neurol, 56, 1095-1097.

Ihara, Y., Jukina, N., Miura, R., Ogawara, M. (1986) Phosphorylated tau protein is integrated into paired helical filaments in Alzheimer's disease. J Biochem, 99, 1807-1810.

Illenberger, S., Zheng-Fischhöfer, Q., Preuss, U., Stamer, K., Baumann, K., Trinczek, B., Biernat, J., Godemann, R., Mandelkow, E., Mandelkow, E. (1998) The Endogenous and Cell Cycle-dependent Phosphorylation of tau Protein in Living Cells: Implications for Alzheimer's Disease. Molecular Biology of the Cell, 9, 1495-1512.

Ipsiroglu, O. S., Stromberger, C., Ilas, J., Höger, H., Mühl, A., Stöckler-Ipsiroglu, S. (2001) Changes of tissue creatine concentrations upon oral supplementation of creatine-monohydrate in various animal species. Life Sciences, 69, 1805-1815.

Iwatsubo, T., Odaka, A., Suzuki, N., Mizusawa, H., Nukina, N., Ihara, Y. (1994) Visualization of Aβ42(43) and Aβ40 in senile plaques with end-specific Aβ monoclonals: evidence that an initially deposited species is Aβ42(43). Neuron, 13, 45-53.

Jack, C. R. Jr., Peterson, R. C., Xu, Y. C., Waring, S. C., O'Brien, P. C., Tangalos, E. G., Smith, G. E., Ivnik, R. J., Kokmen, E. (1997) Medial temporal atrophy on MRI in normal aging and very mild Alzheimer's disease. Neurology, 49, 786-794.

Jamin, N., Duman, P., Moncuit, J., Fridman, W., Teillaud, J., Carr, G. L., Williams, G. P. (1998) Highly resolved chemical imaging of living cells by using synchrotron infrared microspectroscopy. Proc Natl Acad Sci USA, 95, 4837-4840.

Joachim, C. L., Morris, J. H., Selkoe, D. J. (1989) Diffuse senile plaques occur commonly in the cerebellum in Alzheimer's disease. Am J Path, 135, 309-319.

Johnston, J. A., Cowbur, R. F., Norgren, S., Wiehager, B., Venizelos, N., Winblad, B., Vigo-Pelfrey, C., Schenk, D., Lannfelt, L., O'Neill, C. (1994) Increased β-amyloid release and levels of amyloid precursor protein (APP) in fibroblast cell lines from family members with the Swedish Alzheimer's disease APP670/671 mutation. FEBS Letters, 354, 274-278.

Kang, J., Lemaire, H., Unterbeck, A., Salbaum, J. M. Masters, C. L., Grzeschik, K., Multhaup, G., Beyreuther, K., Müller-Hill, B. (1987) The precursor of Alzheimer's disease amyloid A4 protein resembles a cell-surface receptor. Nature, 325, 733-736.

Khachaturian, Z. S. (1985) Diagnosis of Alzheimer's Disease. Arch Neurol, 42, 1097-1105.

Kidd, M. (1963) Paired Helical Filaments in Electron Microscopy of Alzheimer's Disease. Nature, 197, 192-193.

Kidd, M. (1964) Alzheimer's disease – an electron microscopal study. Brain, 87, 307-324.

Kienlen-Campard, P., Miolet, S., Tasiaux, B., Octave, J. Intracellular Amyloid-β1-42, but not extracellular soluble amyloid-β peptides, induces neuronal apoptosis. J Biol Chem, 277, 15666-15670.

Koo, E. H., Squazzo, S. L. (1994) Evidence that production and release of amyloid β-protein involves the endocytic pathway. J Biol Chem, 269, 17386-17389.

Kosik, K. S., Joachim, C. L., and Selkoe, D. J. (1986) Mirotubule-Associated Protein Tau (tau) is a major antigenic component of paired helical filaments in Alzheimer disease. Proc Natl Acad Sci USA, 83, 4044-4048.

Laakso, M. P., Soininen, H., Partanen, K., Lehtovirta, M., Hallikainen, M., Hänninen, T., Helkala, E.-L., Vainio, P., Riekkinen, P. J. Sr. (1998) MRI of the hippocampus in Alzheimer's disease: sensitivity, specificity, and analysis of the incorrectly classified subjects. Neurobiol Aging, 19, 23-31.

Lasch, P., Haensch, W., Naumann, D., Diem, M. (2004) Imaging of colorectal adenocarcinoma using FT-IR microspectroscopy and cluster analysis. Biochim et Biophys Acta, 1688, 176-186.

Levy-Lahad, E., Wasco, W., Poorkaj, P., Romano, D. M., Oshima, J., Pettingell, W. H., Yu, C., Jondro, P. D., Schmidt, S. D., Wang, K., Crowley, A. C., Fu, Y., Guenette, S. Y., Galas, D., Nemens, E., Wijsman, E. M., Bird, T. D., Schellenberg, G. D., Tanzi, R. E. (1995) Candidate gene for the chromosome 1 familial Alzheimer's disease locus. Science, 269, 973-977.

Lewis, E. N., Treado, P. J., Reeder, R. C., Story, G. M., Dowrey, A. E., Marcott, C., Levin, I. W. (1995) Fourier transform spectroscopic imaging using an infrared focal-plane array detector. Anal Chem, 67, 3377-3381.

Li, F., Calingasan, N. Y., Yu, F., Mauck, W. M., Toidze, M., Almeida, C. G., Takahashi, R. H., Carlson, G. A., Beal, M. F., Lin, M. T., Gouras, G. K. (2004) Increased plaque burden in brains of APP mutant MnSOD heterozygous knockout mice. J Neurochem, 89, 1308-1312.

Lovestone, S., and Reynolds, C. H. (1997) The Phosphorylation of Tau: a critical stage in neurodevelopment and neurodegenerative processes. Neuroscience, 78, 309-324.

Mandal, P. K. (2007) Magnetic resonance spectroscopy (MRS) and its application in Alzheimer's disease. Concepts in Magnetic Resonance, 30A(1), 40-64.

Mantsch, H. H., Chapman, D. (1996) Infrared Spectroscopy of Biomolecules. Wiley-Liss, New York.

Mark, R. J., Pang, Z., Geddes, J. W., Uchida, K., Mattson, M. P. (1997) Amyloid β-peptide impairs glucose transport in hippocampal and cortical neurons: involvement of membrane lipid peroxidation. J Neuroscience, 17, 1046-1054.

Masters, C. L., Simms, G., Weinman, N. A., Multhaup, G., McDonald, B. L., Beyreuther, K. (1985) Amyloid plaque core protein in Alzheimer disease and down syndrome. Proc Natl Acad Sci USA, 82, 4245-4249.

Mattson, M. P., Cheng, B., Davis, D., Bryant, K., Lieberburg, I., Rydel, R. E. (1992) β-Amyloid peptides destabilize calcium homeostasis and render human cortical neurons vulnerable to excitotoxicity. J Neuroscience, 12, 376-389.

McEwen, B. S. (1999) Stress and the aging hippocampus. Frontiers in Neuroendocrinology, 20, 49-70.

McKhann, G., Drachman, D., Folstein, M., Katzman, R., Price, D., and Stadlan, E. M. (1984) Clinical diagnosis of Alzheimer's Disease: Report of the NINCDS-ADRDA Work Group under the auspices of Department of Health and Human Services Task Force on Alzheimer's Disease. Neurology, 34, 939-944.

Miller, D. B., O'Callaghan, J. P. (2003) Effects of aging and stress on hippocampal structure and function. Metabolism, 52, 17-21.

Miller, L. M., and Dumas, P. (2006) Chemical imaging of biological tissue with synchrotron infrared light. Bochim et Biophys Acta, 1758, 846-857.

Miller, L. M., Smith, R. J. (2005) Synchrotrons versus globars, point-detectors versus focal plane arrays: Selecting the best source and detector for specific infrared microspectroscopy and imaging applications. Vib Spec, 38, 237-240.

Mirra, S. S., Heyman, A., McKeel, D., Sumi, S. M., Crain, B. J., Brownlee, L. M., Vogel, F. S., Hughes, J. P., van Belle, G., Berg, L., and participating CERAD neuropathologists. (1991) The Consortium to Establish a Registry for Alzheimer's Disease (CERAD). Part II. Standardization of the neuropathologic assessment of Alzheimer's disease. Neurology, 41, 479-486.

Münch, G., Schinzel, R., Loske, C., Wong, A., Durany, N., Li, J. J., Vlassara, H., Smith, M. A., Perry, G., Riederer, P. (1998) Alzheimer's disease – synergistic effects of glucose deficit, oxidative stress and advanced glycation endproducts. J Neural Transm, 105, 439-461.

The National Institute on Aging, and Reagan Institute Working Group on Diagnostic Criteria for the Neuropathological Assessment of Alzheimer's Disease. (1997) Neurobiology of Aging, 18, S1-S2.

Neuroinflammation Working Group: Akiyama, H., Barger, S., Barnum, S., Bradt, B., Bauer, J., Cole, G. M., Cooper, N. R., Eikelenboom, P., Emmerling, M., Fiebich, B. L., Finch, C. E., Frautschy, S., Griffin, W. S. T., Hampel, H., Hull, M., Landreth, G., Lue, L., Mrak, R., Mackenzie, I., McGeer, P. L., O'Banion, M. K., Pachter, J., Pasinetti, G., Plata-Salaman, C., Rogers, J., Rydel, R., Shen, Y., Streit, W., Strohmeyer, R., Tooyoma, I., Van Muiswinkel, F. L., Veerhuis, R., Walker, D., Webster, S., Wegrzyniak, B., Wenk, G., Wyss-Coray, T. (2000) Inflammation and Alzheimer's disease. Neurobiology of Aging, 21, 383-421.

Newell, K. L., Hyman, B. T., Growdon, J. H., Hedley-Whyte, E. T. (1999) Application of the National Institute on Aging (NIA)-Reagan Institute Criteria for the Neuropathological Diagnosis of Alzheimer Disease. J Neuropathol Exp Neurol, 58, 1147-1155.

Nucara, A., Lupi, S., Calvani, P. (2003) The infrared synchrotron radiation beamline at the third generation light source ELETTRA. Rev Sci Instrum, 74, 3934-3942.

Nukina, N., and Ihara, Y. (1986) One of the antigenic determinants of paired helical filaments is related to tau protein. J Biochem, 99, 1541-1544.

Ogg, M. T. J. (2002) Vibrational microspectroscopy of Alzheimer diseased hippocampal tissue. M. Sc. Thesis, University of Manitoba.

Ohtsuki, S. (2004) New aspects of the blood-brain barrier transporters; its physiological roles in the central nervous system. Biol Pharm Bull, 27, 1489-1496.

Perdahl, E., Adolfsson, R,. Alafuzoff, I., Albert, K. A., Nestler, E. J., Greengard, P., Winblad, B. (1984) Synapsin I (Protein I) in different brain regions in senile dementia of Alzheimer type and in multiinfarct dementia. J Neural Transmission, 60, 133-141.

Pfefferbaum, A., Adalsteinsson, E., Speilman, D., Sullivan, E. V., Lim, K. O. (1999) In vivo brain concentrations of N-acetyl compounds, creatine, and choline in Alzheimer disease. Arch Gen Psychiatry, 56, 185-192.

Price, D. L., Sisodia, S. S., Borchelt, D. R. (1998) Genetic neurodegenerative diseases: the human illness and transgenic models. Science, 282, 1079-1083.

Puchtler, H., Sweat, F., Levine, M. (1962) On the binding of congo red by amyloid. Histochem Cytochem, 10, 355-362.

Rak, M. (2007) Synchrotron infrared microspectroscopy of biological tissues: brain tissue from TgCRND8 Alzheimer's disease mice and developing scar tissue in rats. PhD Thesis, University of Manitoba.

Rak, M., Del Bigio, M. R., Mai, S., Westaway, D., Gough, K. (2007) Dense-core and diffuse Aβ plaques in TgCRND8 mice studies with synchrotron FTIR microspectroscopy. Biopolymers, online.

Rogaev, E. I., Sherrington, R., Rogaeva, E. A., Levesque, G., Ikeda, M., Liang, Y., Chi, H., Lin, C., Holman, K., Tsuda, T., Mar, L., Sorbi, S., Nacmias, B., Placentini, S., Amaducci, L., Chumakov, I., Cohen, D., Lannfelt, L., Fraser, P. E., Rommens, J. M., St George-Hyslop, P. H. (1995) Famillial Alzheimer's disease in kindreds with missense mutations in a gene on chromosome 1 related to the Alzheimer's disease type 3 gene. Nature, 376, 775-778.

Roher, A. E., Kokjohn, T. A., Esh, C., Weiss, N., Childress, J., Kalback, W., Luehrs, D. C., Lopez, J., Brune, D., Kuo, Y., Farlow, M., Murrell, J., Vidal, R., Ghetti, B. The human amyloid-β precursor protein$_{770}$ mutation V717F generates peptides longer than amyloid-β-(40-42) and flocculent amyloid aggregates. J Biol Chem, 279, 5829-5836.

Roth, M., Tomlinson, B. E., and Blessed, G. (1966) Correlation between Scores for Dementia and Counts of 'Senile Plaques' in Cerebral Grey Matter of Elderly Subjects. Nature, 209, 109-110.

Scheff, S. W., and Price, D. A. (2003) Synaptic pathology in Alzheimer's disease: a review of ultrastructural studies. Neurobiol Aging, 24, 1029-1046.

Scheff, S. W., Price, D. A., Schmitt, F. A., Mufson, E. J. (2006) Hippocampal synaptic loss in early Alzheimer's disease and mild cognitive impairment. Neurobiol Aging, 27, 1372-1384.

Scheuner, D., Eckman, C., Jensen, M., Song, X., Citron, M., Suzuki, N., Bird, T. D., Hardy, J., Hutton, M., Kukull, W., Larson, E., Levy-Lahad, E., Viitanen, M., Peskind, E., Poorkaj, P., Schellenberg, G., Tanzi, R., Wasco, W., Lannfelt, L., Selkoe, D., Younkin, S. (1996) Secreted amyloid β-protein similar to that in the senile plaques of Alzheimer's disease is increased *in vivo* by the presenilin 1 and 2 and *APP* mutations linked to familial Alzheimer's disease. Nature Medicine, 2, 864-870.

Schmechel, D. E., Saunders, A. M., Strittmatter, W. J., Crain. B. J., Hulette, C. M., Joo, S. H., Pericak-Vance, M. A., Goldgaber, D., Roses, A. D. (1993) Increased amyloid β-peptide deposition in cerebral cortex as a consequence of apolipoprotein E genotype in late-onset Alzheimer disease. Proc Natl Acad Sci USA, 90, 9649-9653.

Schultz, S. E., and Kopec, J. A. (2003) Impact of Chronic Conditions. Statistics Canada Health Reports, 14, 41-53.

Selkoe, D. J. (2001) Alzheimer's Disease: Genes, Proteins, and Therapy. Physiol Rev, 81, 741-766.

Selkoe, D. J., Podlisny, M. B., Joachim, C. L., Vickers, E. A., Lee, G., Fritz, L. C., Oltersdorf, T. (1988) β-Amyloid precursor protein of Alzheimer disease occurs as 110- to 135-kilodalton membrane-associated proteins in neural and nonneural tissues. Proc Natl Acad Sci USA, 85, 7341-7345.

Sherrington, R., Rogaev, E. I., Liang, Y., Rogaeva, E. A., Levesque, G., Ikeda, M., Chi, H., Lin, C., Li, G., Holman, K., Tsuda, T., Mar, L., Foncin, F., Bruni, A. C., Montesi, M. P., Sorbi, S., Rainero, I., Pinessi, L., Nee, L., Chumakov, I., Pollen, D., Brookes, A., Sanseau, P., Polinsky, R. J., Wasco, W., Da Silva, H. A. R., Haines, J. L., Pericak-Vance, M. A., Ranzi, R. E., Roses, A. D., Fraser, P. E., Rommens, J. M., St George-Hyslop, P. H. (1995) Cloning of a gene bearing missense mutations in early-onset familial Alzheimer's disease. Nature, 375, 754-760.

Shoji, M., Golde, T. E., Ghiso, J., Cheung, T. T., Estus, S., Shaffer, L. M., Cai, X.-D., McKay, D. M., Tintner, R., Frangione, B., Younkin, S. G. (1992) Production of the Alzheimer Amyloid β protein by normal proteolytic processing. Science, 258, 126-129.

Šimić, G., Kostović, I., Winblad, B., Bogdanović, N. (1997) Volume and number of neurons of the human hippocampal formation in normal aging and Alzheimer's disease. J Comp Neurol, 379, 482-494.

Sisodia, S. S. (1992) β-Amyloid precurson protein cleavage by a membrane-bound protease. Proc Natl Acad Sci USA, 89, 6075-6079.

Squire, L. R., and Zola-Morgan, S. (1991) The medial temporal lobe memory system. Science, 253, 1380-1386.

Stoppe, G., Bruhn, H., Pouwels, P. J. W., Hänicke, W., Frahm, J. (2000) Alzheimer disease: absolute quantification of cerebral metabolites in vivo using localized proton magnetic resoncance spectroscopy. Alzheimer Dis Assoc Disord, 14, 112-119.

Strittmatter, W. J., Saunders, A. M., Schmechel, D., Pericak-Vance, M., Enghild, J., Salvesen, G. S., Roses, A. D. (1993) Apolipoprotein E: high-avidity binding to β-amyloid and increased frequency of type 4 allele in late-onset familial Alzheimer disease. Proc Natl Acad Sci USA, 90, 1977-1981.

Surewicz, W. K., Mantsch, H. H., and Chapman, D. (1993) Determination of protein secondary structure by Fourier Transform infrared spectroscopy: a critical assessment. Biochemistry, 32, 389-394.

Tagliavini, F., Giaccone, G., Frangione, B., Bugiani, O. (1988) Preamyloid deposits in the cerebral cortex of patients with Alzheimer's disease and nondemented individuals. Neurosci Lett, 93, 191-196.

Takahashi, R. H., Milner, T. A., Li, F., Nam, E. E., Edgar, M. A., Yamaguchi, H., Beal, M. F., Xu, H., Greengard, P., Gouras G. K. (2002) Am J Path, 161, 1869-1879.

Takeuchi, H., Mizuno, T., Zhang, G., Wang, J., Kawanokuchi, J., Kuno, R., Suzumura, A. (2005) Neuritic beading induced by activated microglia is an early feature of neuronal dysfunction toward neuronal death by inhibition of mitochondrial respiration and axonal transport. J Biol Chem, 280, 10444-10454.

Tarnopolsky, M. A., and Beal, M. F. (2001) Potential for creatine and other therapies targeting cellular energy dysfunction in neurological disorders. Ann Neurol, 49, 561-574.

Terry, R. D. (1963) The Fine Structure of neurofibrillary tangles in Alzehimer's disease. J Neuropathol Exp Neurol, 22, 629-642.

Terry, R. D., Gonatas, N. K., Weiss, M. (1964) Ultrastructural studies in Alzheimer's presenile dementia. Am J Path, 44, 269-297.

Terry, R. D., Lawrence, A. H., DeTeresa, R., Davies, P., Tobias, H., Katzman, R. (1987) Senile dementia of the Alzheimer type without neocortical neurofibrillary tangles. J Neuropathol Exp Neurol, 46, 262-268.

Tomlinson, B. E., Blessed, G., and Roth, M. (1968) Observations on the Brains of Non-Demented Old People. J neurol Sci, 7, 331-356.

Tomlinson, B. E., Blessed, G., and Roth, M. (1970) Observations on the Brains of Demented Old People. J neurol Sci, 11, 205-242.

Tucker, R. P. (1990) The roles of microtubule-associated proteins in brain morphogenesis: a review. Brain res rev, 15, 101-120.

Tuppo, E. E., and Arias, H. R. (2005) The role of inflammation in Alzheimer's disease. International Journal of Biochemistry & Cell Biology, 37, 289-305.

Urenjak, J., Williams, S. R., Gadian, D. G., Noble, M. (1993) Proton nuclear magnetic resonance spectroscopy unambiguously identifies different neural cell types. J Neurosci, 13, 981-989.

Valenzuela, M. J., Sachdev, P. (2001) Magnetic resonance spectroscopy in AD. Neurology, 56, 592-598.

Vassar, R., Bennett, B. D., Babu-Khan, S., Kahn, S., Mendiaz, E. A., Denis, P., Teplow, D. B., Ross, S., Amarante, P., Loeloff, R., Luo, Y., Fisher, S., Fuller, J., Edenson, S., Lile, J., Jarosinski, M. A., Biere, A. L., Curran, E., Burgess, T., Loui, J., Collins, F., Treanor, J., Rogers, G., Citron, M. (1999) β-Secretase cleavae of Alzheimer's amyloid precursor protein by the transmembrane aspartic protease BACE. Science, 286, 735-741.

Versijpt, J. J., Dumont, F., Van Laere, K. J., Decoo, D., Santens, P., Audenaert, K., Achten, E., Slegers, G., Dierckx, R. A., Korf, J. (2002) Assessment of neuroinflammation and microglial activation in Alzheimer's disease with radiolabelled PK 11195 and single photon emission computed tomography. Eur Neurol, 50, 39-47.

Villareal, D. T., and Morris, J. C. (1998) The Diagnosis of Alzheimer's Disease. Alzheimer's Disease Review, 3, 142-152.

Wallimann, T., and Hemmer, W. (1994) III-2 Creatine kinase in non-muscle tissues and cells. Mol Cell Biochem, 133/134, 193-220.

Wong, P. C., Cai, H., Borchelt, D. R., Price, D. L. (2002) Genetically engineered mouse models of neurodegenerative diseases. Nature Neuroscience, 5, 633-639.

Wood, J. G., Mirra, S. S., Pollock, N. J., Binder, L. I. (1986) Neurofibrillary Tangles of Alzheimer disease share antigenic determinants with the axonal microtubule-associated protein Tau (tau). Proc Natl Acad Sci USA, 83, 4040-4043.

Wyss, M., and Kaddurah-Daouk, R. (2000) Creatine and creatinine metabolism. Physiological Reviews, 80, 1107-1213.

Wyss, M., and Schulze, A. (2002) Health implications of creatine: can oral creatine supplementation protect against neurological and atherosclerotic disease? Neuroscience, 112, 243-260.

Yamaguchi, H., Hirai, S., Morimatsu, M., Shoji, M., Harigaya, Y. (1988) Diffuse type of senile plaques in the brains of Alzheimer-type dementia. Acta Neuropathol, 77, 113-119.

Yan, R., Bienkowski, M. J., Shuck, M. E., Miao, H., Tory, M. C., Pauley, A. M., Brashier, J. R., Stratmen, N. C., Wathews, W. R., Buhl, A. E., Barter, D. B., Tomasselli, A. G., Parodi, L. A., Heinrikson, R. L., Gurney, M. E. (1999) Membrane-anchored aspartyl protease with Alzheimer's disease β-secretase activity. Nature, 402, 533-537.